Investigating the Solar Wind Dynamic Pressure Control on the Magnetosphere-Ionosphere-Thermosphere System Using Global Numerical Models

by

Doğacan Su Öztürk

A dissertation submitted in partial fulfillment of the requirements for the degree of
Doctor of Philosophy
(Atmospheric Oceanic and Space Sciences and Scientific Computing)
in The University of Michigan
2018

Doctoral Committee:

Professor James A. Slavin, Co-Chair
Associate Professor Shasha Zou, Co-Chair
Professor Kenneth G. Powell, Cognate
Professor Aaron J. Ridley, Member

Doğacan Su Öztürk

dcsoztrk@umich.edu

ORCID iD: 0000-0002-8071-2707

To all the kids, refugees and immigrants of the world

ACKNOWLEDGEMENTS

The research in this dissertation was funded in part by the MMS Project at the Southwest Research Institute under their NASA contract NNG04EB99C, the NSF AGS 1342968 and AGS 1203232 grants, and the University of Michigan Internal Fund. I would also like to gratefully acknowledge the Fulbright Scholarship Program, and Dr. Teh-Sun Lee and his family for the Rackham Teh-Sun Lee award.

However, most of the support I received during my PhD does not come from the grants and scholarships but from the insight, experience and time that people so kindly shared with me. Here, I will do my best to acknowledge their efforts and thank them.

To my advisors, to Dr. Shasha Zou, I can't thank you enough for your kindness, guidance, patience and sincerity. I will always take pride in being one of your first students, and I will always hope to make you proud. To Dr. James Slavin, I am deeply grateful for your wisdom, your humanity and your generosity in creating moments, whether it be a tour in the British Natural History Museum, watching the MMS launch, or trying a new vegetarian restaurant. I will always cherish these moments, and will aspire to be as kind and generous as you are.

To my committee members, to Dr. Aaron Ridley, I am very thankful for your eagerness to solve my problems, and teaching me how to come to terms with my perfectionist side, instead of drowning it. And many thanks for developing GITM, it had been instrumental in my dissertation study and I think I will be using it quite often in the foreseeable future. To Dr. Ken Powell, thank you very much for advising

me through the years on the scientific computing program and making time to meet with students even for trivial questions about progress. I am very honored to have you in my committee.

To the CLaSP faculty and researchers, thank you for all you have taught me. To Dr. Igor Sokolov for being a great advisor and a great communicator without words. To Dr. Valeriy Tenishev, for teaching me not to be afraid of asking questions. To Dr. Daniel Welling for believing in me, and for teaching me Python!

To the mentors in my life, I am forever indebted to you. Thank you to Dr. Rona Oran for your insight and experience, to Dr. Raluca Illie for being the voice of reason many times, to Dr. Leonardo Hector Regoli for your solidarity and coffee times and to Dr. Andres Munoz-Jaramillo for picking up my pieces.

To the CLaSP Staff, you run this department! To Faye Ogasawara, for teaching me how to use macports, the most important skill I acquired during my PhD, to Eidilia Thomas, for bluebeary and always making me feel welcome, to Laura Hopkins, to Debbie Eddy, to Darren Britten-Bozone, to Rachel Long, and to Sandra Pytlinski thank you so much!

To my caregivers, I am grateful to Dr. Jasmin Parwaz, for going out of her way to help me whenever I need, to Meghan Park for fixing my broken hand in no time, to Thomas Payne, for the movies, songs, cars, sports and adventures, to Susan Weber, the moment I met you I knew I could trust you with all my immigration matters!

To Pınar Acar, I can not even start to remember all the times you lifted me up, all the things we laughed about and cried about. Okay, mostly me laughing due to my big sister cunning and your little sister gullibility. You are so dear to me, and there is no such thing as too much you. I am so grateful for all the memories we made and will make.

To my less sexy girlz, Gülüm Albut, Yasemin Kalafatoğlu, Gizem Şengör and Şule Sağroğlu, having this safety net of best friends since primary school allowed me to be

myself. I am forever grateful for our friendship of harmonious imperfections.

To my high school friends, to Gülce Güldür for ever so graciously keeping me in the loop, to Erkin Özer for being mad at me for going away, to Hatice İrem Demir for dragging me out of Ann Arbor for day trips to Chicago and New York, to Can Özer, for rooting for me like a hooligan would for Beşiktaş, to Zafer Temizkan, for always being amused by my serious concerns.

To my university friends, to Egemen Menteş for coming all the way to Ann Arbor to spend my first summer here, you are an amazing friend and I miss the comfort of being in your presence every day, to Mertcan Bayar, your friendship and honesty makes me stronger and to Serdar Seçkin, for your encouragement throughout the way even at times when we were in deep troubles.

To my Erasmus friends, Cağlar Genç, Emile Soulié, João Carreira, Miguel Miranda, Alexandra Schneider, Bahar Yousefian Sandal, Sema Ermez, Meliha Gözde Rainville and Halil Kükner, you taught me how to let things go and make fun of myself, both very much needed qualities in life!

To my Fulbright friends, who are all so very special. To Setsuko Yokoyama for being the most curious, graceful and mischievous soul I have ever met. To Györgyi Parditka for saving Hungary and having a plan on how to be friends, to Eva Rez for respecting and valuing people like nobody else does.

To Avinkrishnan Vijayachandran, just a word is enough to put you in action, thank you for your bravery and all the mother recipes we cooked together. They warmed my kitchen, my heart and my stomach!

To my Istanbul friends, to Reha Altay Bozgül for always saying what you believe, and for always believing in what is morally right, Ömer Aykut for being smitten, and to Mehmet Orhan Şanko for your punchlines. We will always be together in my heart.

To Manan Kocher, for a lot of things but mostly for “boy, don’t we know how to

have fun?" and to Fadi Shihadeh, for showing me losing something is gaining another.

To Gangkai Poh, Christina Clarissa and Artemis, for always being there to take the steam off.

To my best office mates ever, to Shaosui Xu for all the times your heart broke with mine, to Lois K. Sarno-Smith for your courage and empathy, to Nicole Pothier McGilivray for trail blazing and to Abigail R. Azari for our own twisted sense of humor and teaching me how to be political.

To my CLaSP friends, Dmitry Borovikov (and Olga!), Yuxi Chen (and Qin!), Meng Jin (and Ela!), Zhenguang Huang, Yinsi Shou, Ryan Dewey, Camilla Harris, Mary Morris, Samantha Basil, Juan Crespo, Ava Dupre and Patrick Belancourt, I loved bumping into you in the corridors, thank you for all that you have taught me.

To my Ann Arbor friends, Kyle Ding, Ece Sancı, Söğüt Türkmen Aksoy, Remzi Can Aksoy, Pınar Yoldaş, Noah Green, Priyamvada Goyal, Sriram Ganesan, Daniel Nunez, Devina Sanjaya, Aaditya Lakshmanan, Alex Kondrov, Alina Rafikova, Motoki Taniguchi and Ayşe Büke Hızıroğlu, you all made Ann Arbor a home far away from home.

To my conference friends, Kristie LLera, Ashraf Moradi, Banafshe Ferdosi, Niloufar Nowrouzi, Junxiang Hu, Colby Haggerty, Jeffrey Broll, Xueling Shi, Dong Lin, Anthony Saikin, Jennimari Koskela, Emma Douma and Yaxue Dong, you ease the burden of traveling. I look forward to seeing you so much and I am so glad to be in the same field with you.

To my neighbor, Robert Wischmeyer, aka Uncle Bob, thank you for showing that life does not end with death. I am grateful to have met someone as sophisticated, gentle and dutiful as you, and I can't wait for our next eggnog time.

To Daniel Price, for helping me with whatever life throws at me, and dealing with whatever I throw at you. I couldn't have asked for more.

To family friends, Tuna, Meriç, Sülün and Mustafa Uysaler, Mustafa Amca, I

wish I could have thanked you when you were still with us, but thank you very much for a great childhood. To Ayşe Ünal for teaching me to be humble, to Kaan, Murat, Zekiye and Cihat Atsever, growing up with you was great fun.

To my maternal side of the family, in particular my aunts, Sezer Gonay who always makes us laugh, Selma Şahin for loving me before she knew me, Aynur Boyar and my cousin Oya Boyar you have taught me so much more about the world than I could ever repay.

To my paternal side of the family, especially to my aunts, Sare Ünlü for being the most accommodating person in the world while swearing if need be and to Saniye Adalı for our saturday gossip sessions, sending me hand knitted hats, scarves and blankets to keep me warm away from home.

To my grandparents, Sabahat Gonay for teaching me fear is an invitation, Havva Öztürk and Musa Öztürk, in my mind you will always be in that house with green walls and a garden overseeing Ankara, I missed you all.

To Gülten anne, for showing me nothing is only a man's job, and chasing people down with a coal shovel if things come down to that. To Suzan Oktay Erol and Sibel Oktay for having a hand on my back, always.

To my undergraduate advisor, Dr. Zerefşan Kaymaz, you are the architect of my career and I have never met someone as sensible and selfless as you. One of my happiest memories is the time when we were having beer and pizza as they towed your car and we went hunting for it after we finished the beers. You are a great adviser, and your influence on me is beyond words.

To my brother, Deniz Onat Öztürk, for being too cool for school, and giving the best hugs even as a six month old baby! You also get an apology. I wish I was there for your milestones, but I hope you can come and live with me for the rest of our lives. I am so happy with how you turned out to be.

To my parents, my mother Nilüfer Öztürk who worked day and night, at a job

she was very good at but she loathed, to give us a better future, my father Mehmet Öztürk who valued intellectuality most, in an era that does not value wisdom, I don't think there are words that can describe how much I value you and how much I feel humbled by all you have done. I wouldn't have wanted to be born, but if being born is inevitable, you two are the best parents to have. Thank you for teaching me early on about different forms of privilege, class conflict and how to be on the right side of history.

To the people who care for each other, to the green grass, to the blue sky, to the birds singing, thank you!

TABLE OF CONTENTS

DEDICATION ii

ACKNOWLEDGEMENTS iii

LIST OF FIGURES xii

LIST OF TABLES xxi

ABSTRACT xxii

CHAPTER

I. Introduction 1

1.1 The Near Earth Environment 1
1.1.1 The Solar Wind and Interplanetary Magnetic Field 1
1.1.2 The Magnetosphere 5
1.1.3 The Ionosphere 7
1.1.4 The Thermosphere 7
1.2 The Geospace System Coupling 9
1.2.1 Solar Wind - Magnetosphere Interaction 9
1.2.2 Magnetosphere - Ionosphere Interaction 18
1.2.3 Ionosphere - Thermosphere Interaction 24
1.2.4 Magnetic Perturbations at the Ground 28
1.3 Purpose of the Study 32

II. The Global Model of the Geospace System 34

2.1 The Ideal Magnetohydrodynamic Equations 34
2.2 Global Magnetosphere Model 35
2.3 Inner Magnetosphere Model 35
2.3.1 Rice Convection Model: RCM 35
2.3.2 Comprehensive Ring Current Model: CRCM 36
2.4 Ionosphere Model 36

2.5 Ionosphere Thermosphere Model . . . 37
2.5.1 The Model Description . . . 37
2.5.2 The Governing Equations . . . 38
2.6 Other Tools Used in the Study . . . 42
2.6.1 Ground Observations . . . 42
2.6.2 Spacecraft Observations . . . 43
2.6.3 SpacePy . . . 43

III. The Response of the Geospace System to Solar Wind Dynamic Pressure Enhancements Under Different IMF B_Y orientations . . . 44

3.1 Introduction . . . 44
3.2 Simulation Setup . . . 47
3.3 Response of the M-I System . . . 50
3.3.1 Ground Magnetometer Response to Different IMF B_Y 50
3.3.2 Field-aligned Current Systems Under Different IMF B_Y . . . 51
3.3.3 Contributions from Different Currents Systems to the Magnetic Perturbations at the Ground . . . 56
3.3.4 Magnetospheric Sources for the Perturbations at the Ground . . . 57
3.4 Discussion . . . 64
3.4.1 PI Signature Under Different IMF B_Y . . . 64
3.4.2 MI Signature Under Different IMF B_Y . . . 65
3.5 Summary and Conclusions . . . 66

IV. A Case Study of a Sudden Solar Wind Dynamic Pressure Increase on the Geospace System . . . 68

4.1 Introduction . . . 68
4.2 Methodology . . . 71
4.2.1 Simulation Setup . . . 72
4.2.2 Validation of the Simulation Results . . . 75
4.3 Magnetospheric Response . . . 77
4.4 Ionospheric Response . . . 79
4.5 Discussion . . . 88
4.6 Summary and Conclusions . . . 95

V. A Case Study of a Sudden Solar Wind Dynamic Pressure Decrease on the Geospace System . . . 96

5.1 Introduction . . . 96
5.2 Methodology . . . 99
5.2.1 Simulation Setup . . . 99

5.2.2 Spacecraft Positions . . . 103
5.3 Results . . . 104
5.3.1 Magnetospheric Response . . . 104
5.3.2 Ionospheric Response . . . 110
5.4 Discussion . . . 118
5.5 Summary and Conclusions . . . 119

VI. The Geospace System Responses to Idealized Sudden Solar Wind Dynamic Pressure Increase and Decrease . . . 121

6.1 Introduction . . . 121
6.2 Methodology . . . 122
6.2.1 Simulation Setup for Compression . . . 122
6.2.2 Simulation Setup for Decompression . . . 125
6.3 Comparison of Magnetospheric Responses to Strong Compression and Decompression Events . . . 127
6.4 Comparison of Ionospheric Responses . . . 140
6.4.1 FAC Response . . . 140
6.4.2 Joule Heating Response . . . 142
6.4.3 Ion Temperature Response . . . 144
6.4.4 Virtual Magnetometer Response . . . 146
6.4.5 Altitude Profiles in the Ionosphere . . . 148
6.5 Discussion . . . 153
6.6 Summary and Conclusions . . . 156

VII. Conclusions and Future Work . . . 158

7.1 Findings of the Work . . . 158
7.2 Future Work . . . 161
7.2.1 Exploring the Effects of Other Solar Wind and IMF Drivers During Solar Wind Dynamic Pressure Variations . . . 161
7.2.2 Exploring the Magnetotail Response to the Solar Wind Dynamic Pressure Variations . . . 163
7.2.3 Improving the Models . . . 163

BIBLIOGRAPHY . . . 164

LIST OF FIGURES

Figure

1.1 The early Parker solar wind model shown in the solar ecliptic plane. The spirals are magnetic field lines originating from the center of the Sun and propagating with the solar wind to the interplanetary medium. The solar wind speed is shown as 300 km/s (which is considered slow solar wind today). S/B denotes the sector boundary, which separates the inward and outward-directed magnetic fields. Adapted from Figure 4.1 of [*Balogh et al.* (2008)]. 3

1.2 The distribution of Earth-directed high speed streams (red) and interplanetary shocks (blue) between the years 2010-2017. The number of events are taken from the NASA CCMC DONKI Event Catalog. 5

1.3 A schematic representation of the Earth's magnetic dipole. The direction of the magnetic field lines are from south to north. Adapted from *Gombosi* (2004). 6

1.4 The height versus electron density profile of the ionosphere. The peak densities and major ion species of the D, E, F_1, and F_2 layers are shown. Adapted from Figure 2.16 of *Schunk and Nagy* (2009). . 8

1.5 The global averaged number density profiles of total (black) and major thermospheric constituents during solar maximum (left) and solar minimum (right), derived from NRLMSISE-00 model. Adapted from Figure 2.a and 2.d of *Emmert* (2015). 10

1.6 Illustration of Earth's magnetosphere and its interaction with the solar wind. The Sun is to the left of the image. The illustration shows Earth's bow shock, magnetosheath, magnetopause, magnetotail, plasmasphere and plasma sheet. (The illustration is taken from: *www.nasa.gov/mission_pages/ibex/news/spaceweather.html*) . . . 11

1.7 A schematic diagram showing the magnetospheric convection of magnetic field lines under southward IMF B_Z. The numbers show the magnetic field lines and their ionospheric counterparts. Adapted from Figure 8.15b in *Kelley* (2009). 17
1.8 The two cell convection pattern in the ionosphere is shown in MLT coordinates. The contours are magnetospheric electrostatic potentials. Adapted from Figure 12.4 of *Schunk and Nagy* (2009). 19
1.9 Electric potential contours under different IMF B_Y and B_Z derived from an empirical model. Adapted from Figure 12.4 of *Schunk and Nagy* (2009). 20
1.10 The altitude profiles of the specific,Hall and Pedersen conductivities are shown. Adapted from Figure 2.6 of *Kelley* (2009). 23
1.11 The HDZ and NEZ coordinate system. Adapted from Figure 11.3 of *Schunk and Nagy* (2009). 30
1.12 The magnetic field perturbations associated with sudden commencement at different latitudes and local times. Adapted from *Araki* (1994b). 31
3.1 (a) The idealized solar wind parameters for three simulations. The first panel shows the IMF B_Y for case 1 ($B_Y = -5nT$), case 2 ($B_Y = 0nT$) and case 3 ($B_Y = 5nT$). The second panel shows IMF $B_Z = 5nT$, the third panel shows the velocity, the fourth panel shows the density and the fifth panel shows the variation in the solar wind dynamic pressure. The red line marks the time of the pressure in the outer boundary. (b) The positions of the virtual magnetometers in MLT coordinates. 49
3.2 The MLT-time maps of the magnetic perturbations detected by the uniformly distributed virtual ground magnetometers located at middle latitudes (a) and high latitudes (b) are shown. The rows show $50°, 60°, 70°$ and $80°$ latitudes (top to bottom). The panels on the left show the responses when IMF B_Y is negative, the ones in the center show the case when B_Y is 0, and the panels on the right show the response when B_Y is positive. The red contours show positive, blue contours show negative perturbations. The purple line is the zero contour. Green lines show the dusk, noon, dawn, midnight sectors. 52

3.3 (a) The temporal evolution of the FACs in the Northern hemisphere between t and t+3 minutes under different IMF B_Y conditions. From left to right, the first column shows the case for negative B_Y, the second column shows the case for zero B_Y and the third column shows the case for positive B_Y. (b) The temporal evolution of the time differenced FACs are shown for the same time instances. The perturbation FACs that give rise to PI and MI signatures on the ground are labeled. 55

3.4 The contour plots showing contribution from different current systems in the M-I system for the case where B_Y is zero at three time instances t-1, t+3, and t+7 minutes. From left to right each column shows FAC, Pedersen, Hall, Magnetospheric currents and the total perturbation respectively. 59

3.5 The ground magnetic perturbation profiles taken at peak PI (t+3 min.) and MI (t+7 min.) are shown for the northern hemisphere. From left to right the columns show negative B_Y, zero B_Y, and positive B_Y cases. 60

3.6 The equatorial magnetospheric flow profiles taken before the compression at t (top row), and 1 minute after the compression (bottom row) are shown. The arrows show the velocity vector, whereas solid lines show the magnetic field lines, colored based on the direction of the field-aligned current on the ionospheric foot point (red/blue-upward/downward). From left to right the columns show negative B_Y, zero B_Y, and positive B_Y cases. 61

3.7 The equatorial magnetospheric flow profiles taken before the compression at t + 3 min. (top row), andt + 7 min. after the compression (bottom row) are shown. The arrows show the velocity vector, whereas solid lines show the magnetic field lines, colored based on the direction of the field-aligned current on the ionospheric foot point (red/blue-upward/downward). From left to right the columns show negative B_Y, zero B_Y, and positive B_Y cases. 63

4.1 The Wind measurements of the IMF and solar wind plasma parameters, obtained from CDAWeb and the sym-H index, taken from OMNIWeb databases are shown on the left (a). Panels show IMF B_Y, B_Z, x component of the solar wind velocity, proton density and the sym-H index from top to bottom. The same parameters (except sym-H) are shown on the right taken from the simulation at the subsolar point (X=15 R_E) (b). The last panel on the right shows the variation of the simulated dynamic pressure. The solid red lines show the arrival time of the compression front, as detected by ground magnetometers. 74

4.2 The comparison of the N-component of the Poker Flat (PKR) magnetometer observations (red) with the simulated magnetometer response (blue) extracted at the same location of PKR, during the solar wind dynamic pressure enhancement is shown. The negative preliminary impulse signature was observed at 0445 UT. 76

4.3 The simulated equatorial magnetospheric flow profiles taken at 0446 UT(a) and 0447 UT(b) are shown. The arrows show the flow vectors color coded according to their velocities. The magnetic field lines that show the perturbed flow associated with the main impulse phase are shown and color coded according to the direction of the current carried (red, upward; blue, downward). The footprints of these magnetic field lines on the top of the ionosphere are shown in the bottom left corners. 78

4.4 The simulated FACs (first row), Joule heating (second row), ion temperature and convection profiles at 227 km (third row), and the N component of the magnetic field perturbations (fourth row) are shown at the quiet time (a), 0445 UT (b), 0446 UT (c), 0447 UT (d) and 0448 UT (e). The cyan dot shows the location of the PKR magnetometer, and the orange dot shows the location of the geographic north pole (GNP) in the fourth row. 82

4.5 The vertical (100-600 km) profiles for the ion temperature (top row) and neutral temperature (bottom row) taken at 19 LT (18 MLT) between 50° and 90° latitudes taken at quiet time (a/d), 0445 UT (b/e) and 0446 UT (c/f) are shown. The solid (dashed) lines show the eastward (westward) convection velocity. 84

4.6 The vertical (100-600 km) profiles of ion temperature (a), electron temperature (b) and electron density (c) are shown. The panels on the left show PFISR observations, whereas the panels on the right show the simulated responses extracted at the same location. The colors show the time-averaged profiles for before the event (0430-0445 UT) in gray, during (0445-0450 UT) in blue, immediately after (0450-0455 UT) in green and after (0455-0500 UT) in red. The dotted line shows the profile extracted at 0446 UT. 86
4.7 The vertical (100-600 km) density profiles for NO^+ (top) and O^+ (middle) and the neutral temperature are shown. The colors show the time-averaged profiles for before the event (0430-0445 UT) in gray, during (0445-0450 UT) in blue, immediately after (0450-0455 UT) in green and after (0455-0500 UT) in red. The dotted line shows the profile extracted at 0446 UT. 88
4.8 The vertical profile (100-600 km) of the contributions from the ion to neutral collisional heat transfer (red), ion to neutral frictional heat transfer (blue) and neutral vertical heat conduction rates (orange) are shown at 0446 UT at the simulated PFISR location. 92
4.9 The temporal variations of the ion (blue) and neutral (orange) velocities are shown on the left (a), while the collisional (red) and frictional (blue) heating rates are shown on the right (b) at 240 km over the PFISR location. 94
5.1 The input values used for IMF B_Y, B_Z, solar wind plasma parameters V_X and n_p are shown as well as the dynamic pressure and the sym-H index taken from the OMNI Database between 1400 UT to 1500 UT. The solid green line shows the time of dynamic pressure drop. . . . 100
5.2 The simulated IMF B_Y, B_Z, solar wind V_X. N_P and P_{dyn} values extracted from the subsolar point at 17 R_E are shown between 1430 UT to 1500 UT. The solid green line shows the time of the pressure drop. 102
5.3 The positions of MMS-1 (blue) and THEMIS-D (red) spacecraft are shown in GSM XY (a) and XZ (b) coordinates. The magenta dashed lines show the magnetopause boundary calculated with the Shue model, based on the IMF and solar wind values before the dynamic pressure drop. The teal dashed lines show the magnetopause boundary after the dynamic pressure drop. 103

5.4 The pressure contours in the XZ plane with open (black) and closed (white) magnetic field lines are shown on the left for 1435 UT (a), 1438 UT (b). The purple dot shows the location of THEMIS-D, whereas the pink dot shows the location of MMS-1. On the right, contours of V_X are plotted with magnetospheric flow vectors. The blue (red) lines show the magnetic field lines centered at the flow vortices that carry downward (upward) FACs at 1438 UT. 105
5.5 The pressure contours in the XZ plane with open (black) and closed (white) magnetic field lines are shown on the left for 1440 UT (a), 1445 UT (b) and 1450 UT (c). The purple dot shows the location of THEMIS-D, whereas the pink dot shows the location of MMS-1. On the right, contours of V_X are plotted with magnetospheric flow vectors. The blue (red) lines show the magnetic field lines centered at the flow vortices that carry downward (upward) FACs at 1440 UT. 106
5.6 The variation of the magnetopause distance calculated with the Shue model (dashed) and density gradient (solid) with the solar wind dynamic pressure in between 1430 UT to 1500 UT are shown. 107
5.7 The comparison of satellite measurements (bottom panels) and simulated satellite responses (top panels) for THEMIS-D ESA (left) velocity measurements and MMS-1 FGM (right) magnetic field measurements are shown between 1430 UT-1500 UT. The red line shows the y component and the blue line shows the x component of the velocity on the left. On the right, the blue line shows the x, the red line shows the z component of the magnetic field vector. 109
5.8 The FACs, perturbation FACs, Joule heating profile and the simulated ground magnetometer responses to the solar wind dynamic pressure drop are shown for 1435 UT (a), 1438 UT (b), 1440 UT (c), 1445 UT (d) and 1450 UT (e). The green, blue and pink dots in the bottom panels show the locations of the HOP, HOV and RAN magnetometers. 112
5.9 The comparison of the simulated magnetometer responses (red) with HOP (a), HOV (b) and RAN (c) magnetometers (blue) are shown in between 1430 UT-1500 UT. The solid green line shows the response to solar wind dynamic pressure drop. 113

5.10 The GITM results for ion temperature and convection profiles at 210 km (top) and electron density (middle) are shown for 1435 UT (a), 1438 UT (b), 1440 UT (c), 1445 UT (d) and 1450 UT (e). The bottom panel shows the ion temperature for a meridional cut taken between 50° and 90° latitude at 11 LT, with horizontal ion convection velocities plotted on top for the same time steps. 116
5.11 The altitude profiles (110-540 km) at 11 LT, 78° for ion temperature (a), electron temperature (b) and electron density (c) taken at 1435 UT (blue), 1437 (dark green), 1438 UT (pink), 1440 UT (orange), 1445 UT (purple) and 1450 UT (light green) are shown. 117
6.1 The IMF B_Y, B_Z, solar wind V_X, N_P and P_{dyn} values used to drive the weak SI^+ and the strong SI^+ simulations are shown in between 1400 UT to 1500 UT. The red line shows the time when the perturbation was at the outer boundary and the green line shows the arrival of the disturbance to the Earth. 124
6.2 The IMF B_Y, B_Z, solar wind V_X, N_P and P_{dyn} values used to drive the weak SI^+ and the strong SI^- simulations are shown in between 1400 UT to 1500 UT. The red line shows the time when the perturbation was at the outer boundary and the green line shows the arrival of the disturbance to the Earth. 126
6.3 The comparison of the magnetospheric flow profiles at the equatorial plane before the dynamic pressure increase (a) and decrease (b) events. The contours show the x component of the velocity, arrows show the flow vectors, and the contours on the top of the Earth shows the radial current projections (red/upward; blue/downward). 128
6.4 The equatorial magnetospheric flow profiles for SI^+ (a,b,c) and SI^- (d,e,f) taken at 1 minute prior to the perturbation (a,d), at the time of arrival (b,e) and 1 minute after the arrival of the perturbation (c,f). Pink arrows highlight the most significant flow profile changes. . . 130
6.5 The equatorial magnetospheric flow profiles for SI^+ (a,b,c) and SI^- (d,e,f) taken at 3 (a,d), 4 (b,e) and 6 (c,f) minutes after the arrival of the perturbation. Pink and purple arrows highlight the most significant flow profile changes. 132
6.6 The x (blue) and y (red) components of the velocity at dawn (a) and dusk (b) sectors taken at $x = 4R_E$ are shown between 1430 UT to 1500 UT for the SI^+ event. 134

6.7 The x (blue) and y (red) components of the velocity at dawn (a) and dusk (b) sectors taken at $x = 4R_E$ are shown between 1430 UT to 1500 UT for the SI^- event. 135
6.8 A diagram showing the passage of a spacecraft over the PI^+ (clock-wise) and MI^+ (counter clock-wise) vortices in the dusk sector during a compression event (left) and the Vx and Vy components it would measure along its trajectory (right). 138
6.9 A diagram showing the passage of a spacecraft over the PI^- (counter clock-wise) and MI^- (clock-wise) vortices in the dusk sector during a decompression event (left) and the Vx and Vy components it would measure along its trajectory (right) 139
6.10 The evolution of the FACs are shown at quiet time (a), 1 (b), 2 (c) and 6 (d) minutes after the arrival of the perturbations. Panels show strong SI^+, SI^-, weak SI^+ and SI^- simulations from top to bottom. The red (blue) contours show upward (downward) FACs, the dashed and solid lines show electric field potentials. 141
6.11 The evolution of the Joule heating profiles are shown at quiet time (a), 1 (b), 2 (c) and 6 (d) minutes after the arrival of the perturbations. Panels show strong SI^+, SI^-, weak SI^+ and SI^- simulations from top to bottom. 143
6.12 The evolution of the differenced ion temperature profiles are shown at quiet time (a), 1 (b), 2 (c) and 6 (d) minutes after the arrival of the perturbations with ion convection vectors on top for the Northern Hemisphere. Panels show strong SI^+, SI^-, weak SI^+ and SI^- simulations from top to bottom. The strong and weak simulation results are shown with separate color bars. 146
6.13 The evolution of the baseline subtracted magnetic perturbation profiles at the ground are shown at quiet time (a), 1 (b), 2 (c) and 6 (d) minutes after the arrival of the perturbations for the Northern Hemisphere. Panels show strong SI^+, SI^-, weak SI^+ and SI^- simulations from top to bottom. The strong and weak simulation results are shown with separate color bars. 148

6.14 The vertical ion temperature (left), electron temperature (middle), and the electron density (right) profiles at select time steps are shown at peak heating locations on the dawn (a) and the dusk (b) sectors for the strong SI^+ event. The time steps shown are 1430 UT (t-7min; blue), 1437 UT (t; pink), 1438 UT (t+1min; orange), 1440 UT (t+3min; purple), 1445 UT (t+8min; brown) and 1450 UT (t+13min; green). 151
6.15 The vertical ion temperature (left), electron temperature (middle), and the electron density (right) profiles at select time steps are shown at peak heating locations on the dawn (a) and the dusk (b) sectors for the strong SI^- event. The time steps shown are 1430 UT (t-7min; blue), 1437 UT (t; pink), 1438 UT (t+1min; orange), 1440 UT (t+3min; purple), 1445 UT (t+8min; brown) and 1450 UT (t+13min; green). 152
7.1 The variation of the magnetopause standoff distance calculated from the simulations using the density gradient model (solid line) and from the solar wind observations using the Shue model (dashed line) with the IMF B_Z (upper panel; blue) and solar wind dynamic pressure (bottom panel; green) between 1430-1740 UT during the 11 June 2017 event. 162

LIST OF TABLES

Table

1.1 Fast and slow solar wind properties observed at Earth's orbit (adapted from *Schrijver and Siscoe* (2009)). 2

1.2 Layers of the ionosphere and their properties (adapted from *Gombosi* (2004)). 7

ABSTRACT

The geospace system, consisting of the intrinsically coupled magnetosphere, ionosphere and thermosphere (M-I-T), is in pressure balance with the solar wind. During sudden changes in the solar wind dynamic pressure, the magnetosphere undergoes rapid compression or expansion processes which significantly perturb the magnetospheric flow profiles and the global current systems. These sudden global changes are called sudden impulses (SIs). Based on the low-latitude magnetic field perturbation measurements by the ground magnetometers, the SIs are traditionally defined as positive SIs (SI^+s); indicating magnetospheric compression or negative SIs (SI^-s), indicating magnetospheric decompression.

The magnetospheric and ionospheric responses to the SI^+s and SI^-s under different IMF and solar wind drivers are not well established mainly due to the sparsity of observations. Therefore, the modelling approach was adopted to understand the geospace system response. The University of Michigan Block Adaptive Tree Solarwind Roe Upwind Scheme (BATS-R-US) global magnetohydrodynamic (MHD) code was employed to study the generation and propagation of the perturbations associated with the compression and decompression of the magnetosphere system. The high-resolution electric potential and auroral power output from this coupled model were then used to drive the Global Ionosphere Thermosphere Model (GITM) to investigate the I-T system responses to the solar wind dynamic pressure variations.

In this study, we investigated the SI^+ and SI^- processes and their effects on the geospace system. Through idealized simulations, we showed that a two-step

response existed in the magnetosphere and the ionosphere. Both in the SI^+ and SI^- cases, the initial response included magnetopause boundary deformation and forming vortex-like structures in the boundary. The second response was the formation of magnetospheric flow vortices with opposite senses of rotation on the dawn and dusk sectors. These perturbed magnetospheric flows were associated with Field-Aligned Currents (FACs) during both stages that mapped to the ionosphere. Moreover, the ionospheric convection response due to these perturbation FACs preserved the two-step behaviour, since the transient currents reversed directions between stages. The dawn-dusk asymmetry seen in the magnetospheric flows were also maintained in the ionospheric convection patterns.

We also established the role of the IMF B_Y on the geospace response during SI+ events, through idealized simulations. We showed that even though the magnetospheric and ionospheric perturbations that formed during SI+ were very similar, the superposition of these perturbation currents with the B_Y controlled NBZ (Northward B_Z) current system resulted in different FAC profiles. Therefore, the simulated magnetic field perturbations on the ground showed significant variability with the IMF B_Y.

Furthermore, we performed two case studies of an SI^+ and SI^-. The simulations showed that the two-step behaviour was conveyed to the thermosphere, through the ion-neutral coupling. For the SI^+ case, both simulation and observation results showed enhanced ion and electron temperatures and decreased electron density. The SI^- case study showed observational evidence for the simulated magnetospheric flow profiles.

Within this study, the following scientific questions have been addressed: (i) the role of IMF By on the ground magnetometer response to the solar wind dynamic pressure enhancements, (ii) the magnetospheric and ionospheric responses, such as field-aligned currents and convection, (iii) the role of pressure variation in determining

the geospace system response and (iv) the ionosphere-thermosphere coupled responses to the sudden changes in the solar wind dynamic pressure.

CHAPTER I

Introduction

1.1 The Near Earth Environment

The near Earth environment is the region that consists of Earth's neutral atmosphere, ionosphere and magnetosphere systems. Being able to know the conditions in the near-Earth environment is essential for successful telecommunication and spacecraft operations [*Lanzerotti* (2007)]. This region can be highly dynamic depending on the solar wind and IMF conditions This deviation is caused by mass, momentum and energy transport from the solar wind drivers to the near Earth systems. Such changes can cause disruptions in telecommunication signals, impose radiation hazards on spacecraft and air travelers, increase aerodynamic drag causing orbital problems or even loss of the spacecraft [*Picholtz* (1996), *Belehaki et al.* (2009)]. In the following chapters the properties and fundamental drivers of each medium and how they couple will be discussed.

1.1.1 The Solar Wind and Interplanetary Magnetic Field

The solar wind is an ionized plasma flow which is driven by the pressure difference between the Sun's corona and the interstellar medium [*Gombosi* (2004)]. The region in between, which is filled with the supersonic solar wind, is called the heliosphere. This is where the solar system resides, therefore all the bodies inside the

heliosphere interact with the solar wind. Thus, the dynamic pressure exerted on the body significantly affects the environment around it.

The type of interaction between the obstacle and the solar wind depends on the body's magnetism since the solar wind also carries remnants of the solar magnetic field [*Kivelson and Russell* (1997)]. This interplanetary magnetic field (IMF) is frozen into the solar wind plasma, which means that plasma and magnetic field lines move together [*Kivelson and Russell* (1997)]. The solar wind plasma moves outward from a fixed source at the base of Sun, however this source moves as the Sun rotates. Because of this motion, the magnetic field lines and the solar wind stream lines have a spiral shape as shown in Figure 1.1. This spiral is known as the Parker spiral.

Ulysses observations of the solar wind revealed that there were two distinct streams coming from the Sun [*Gosling* (1997)]. The solar wind from the higher latitudes of the Sun is discharged at higher speeds than at the lower latitudes and as a result they have different density, temperature and velocity values. The properties of the 'fast' and 'slow' solar wind are shown in Table 1.1.

Table 1.1: Fast and slow solar wind properties observed at Earth's orbit (adapted from *Schrijver and Siscoe* (2009)).

Property	Slow wind	Fast wind
Density	10 cm^{-3}	3 cm^{-3}
Flow speed	430 ± 100 km/s	700-900 km/s
Proton temperature	4.2 x $10^4 K$	2.4 ± 0.6 x $10^5 K$
Electron temperature	1.3 ± 0.5 x $10^5 K$	1.3 ± 0.2 x $10^5 K$
Magnetic field	6 ± 3 nT	6 ± 3 nT

This variability in the solar wind causes significant dynamic pressure variations along the heliosphere. Since the fast solar wind has a higher velocity, it travels along a less coiled Parker spiral than the slow solar wind, eventually converging to the slow stream at lower latitudes [*Kivelson and Russell* (1997)]. The plasma in between the slow and fast solar wind regions is then compressed forming a high pressure region. As

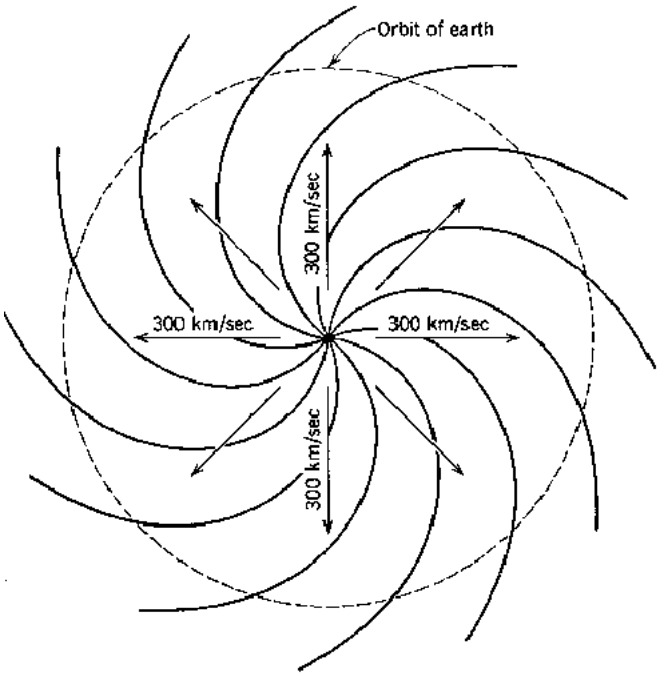

Figure 1.1: The early Parker solar wind model shown in the solar ecliptic plane. The spirals are magnetic field lines originating from the center of the Sun and propagating with the solar wind to the interplanetary medium. The solar wind speed is shown as 300 km/s (which is considered slow solar wind today). S/B denotes the sector boundary, which separates the inward and outward-directed magnetic fields. Adapted from Figure 4.1 of [*Balogh et al.* (2008)].

this interaction region propagates further outward, it becomes increasingly supersonic, resulting in a pair of forward and reverse shocks [*Gombosi* (2004)]. These regions are known as co-rotation interaction regions (CIRs).

Shocks can also form as a result of eruptive processes in the Sun, known as coronal mass ejections (CMEs) [*Kamide and Chian* (2007)]. Large amounts of high energy plasma and magnetic field are discharged from the Sun during CME events [*Gombosi* (2004), *Kamide and Chian* (2007)]. This high speed ejecta compresses the solar wind ahead and forms an interplanetary shock (IP). The CME core can carry a rope-like magnetic structure, which can also interact with Earth's magnetosphere and cause strong geomagnetic activity.

The distribution of the high speed streams and interplanetary shocks that cause enhanced solar wind dynamic pressure at the Earth are shown in Figure 1.2. During solar maximum the number of shock and high speed stream events can exceed 75 events per year, resulting in prolonged disturbances in the Earth's magnetosphere.

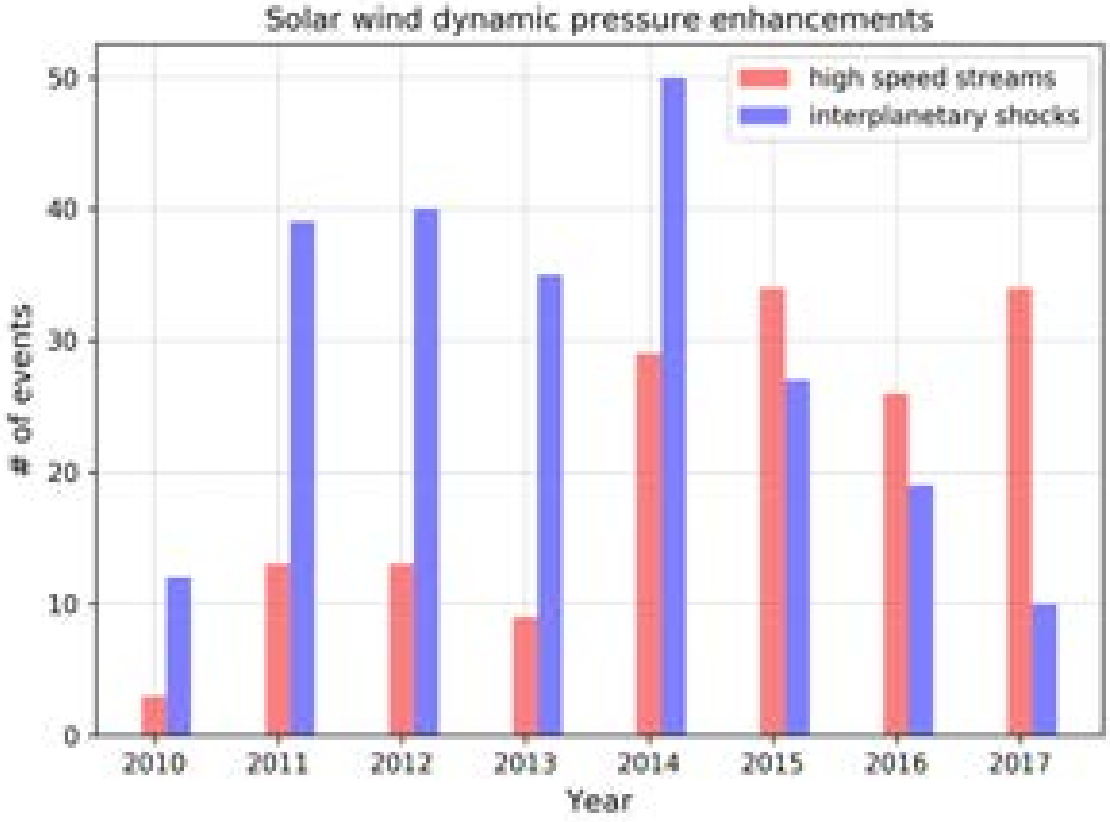

Figure 1.2: The distribution of Earth-directed high speed streams (red) and interplanetary shocks (blue) between the years 2010-2017. The number of events are taken from the NASA CCMC DONKI Event Catalog.

1.1.2 The Magnetosphere

Earth has an intrinsic dipolar magnetic field with a dipole moment of $7.84 \text{x} 10^{15}$ Tm^3. This dipole is tilted about 11° towards the rotation axis *Kivelson and Russell* (1997). Magnetic field lines are directed to the magnetic North Pole as shown in Figure 1.3.

In a coordinate system that is fixed along the dipole moment of the Earth, the rotation can be neglected and the radial and angular magnetic field strengths can be obtained with the equations 1.1 - 1.3.

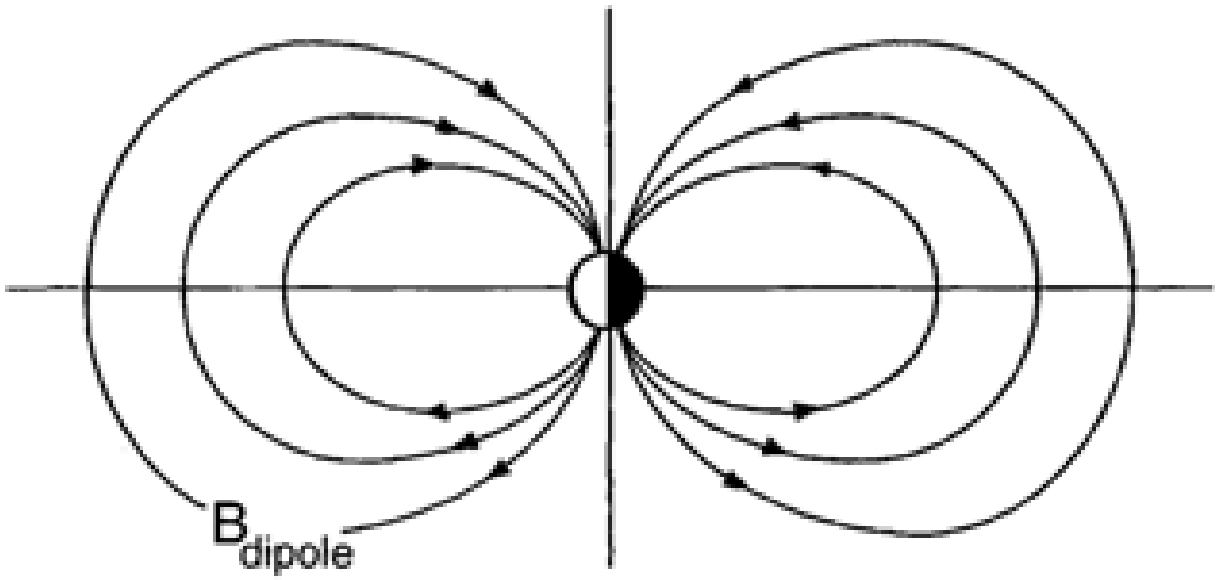

Figure 1.3: A schematic representation of the Earth's magnetic dipole. The direction of the magnetic field lines are from south to north. Adapted from *Gombosi* (2004).

Table 1.2: Layers of the ionosphere and their properties (adapted from *Gombosi* (2004)).

Layer	Altitude	Peak Density	Dominant species
D Region	60-90 km	$10^3\ cm^{-3}$	NO^+, O_2^+, N_2^+
E Region	90-140 km	$10^5\ cm^{-3}$	O_2^+
F_1 Region	140-200 km	$10^6\ cm^{-3}$	O^+
F_2 Region	200-500 km	$10^6\ cm^{-3}$	O^+

$$B_r = 2Mr^{-3}\cos\theta \tag{1.1}$$

$$B_\theta = Mr^{-3}\sin\theta \tag{1.2}$$

$$B = Mr^{-3}\sqrt{1+3\cos^2\theta} \tag{1.3}$$

Here, M is the magnetic dipole moment of the Earth, r is the radial distance from the center of the Earth and θ is the co-latitude where the magnetic field lines map.

1.1.3 The Ionosphere

The ionosphere is the ion and electron dominant region of the terrestrial atmosphere [*Gombosi* (2004)] which overlaps with the mesosphere, thermosphere and exosphere. The ionosphere is highly stratified due to the molecular weight of the ion species and it is classified based on the density of each region. The ionospheric density profile has strong diurnal variation and the peak densities drop by an order of magnitude during the nighttime.

1.1.4 The Thermosphere

The thermosphere is the upper part of the Earth's atmosphere where the slow mixing causes a stratified composition depending on the temperature and the molecular weight of the species [*Gombosi* (2004), *Schunk and Nagy* (2009)]. The density of

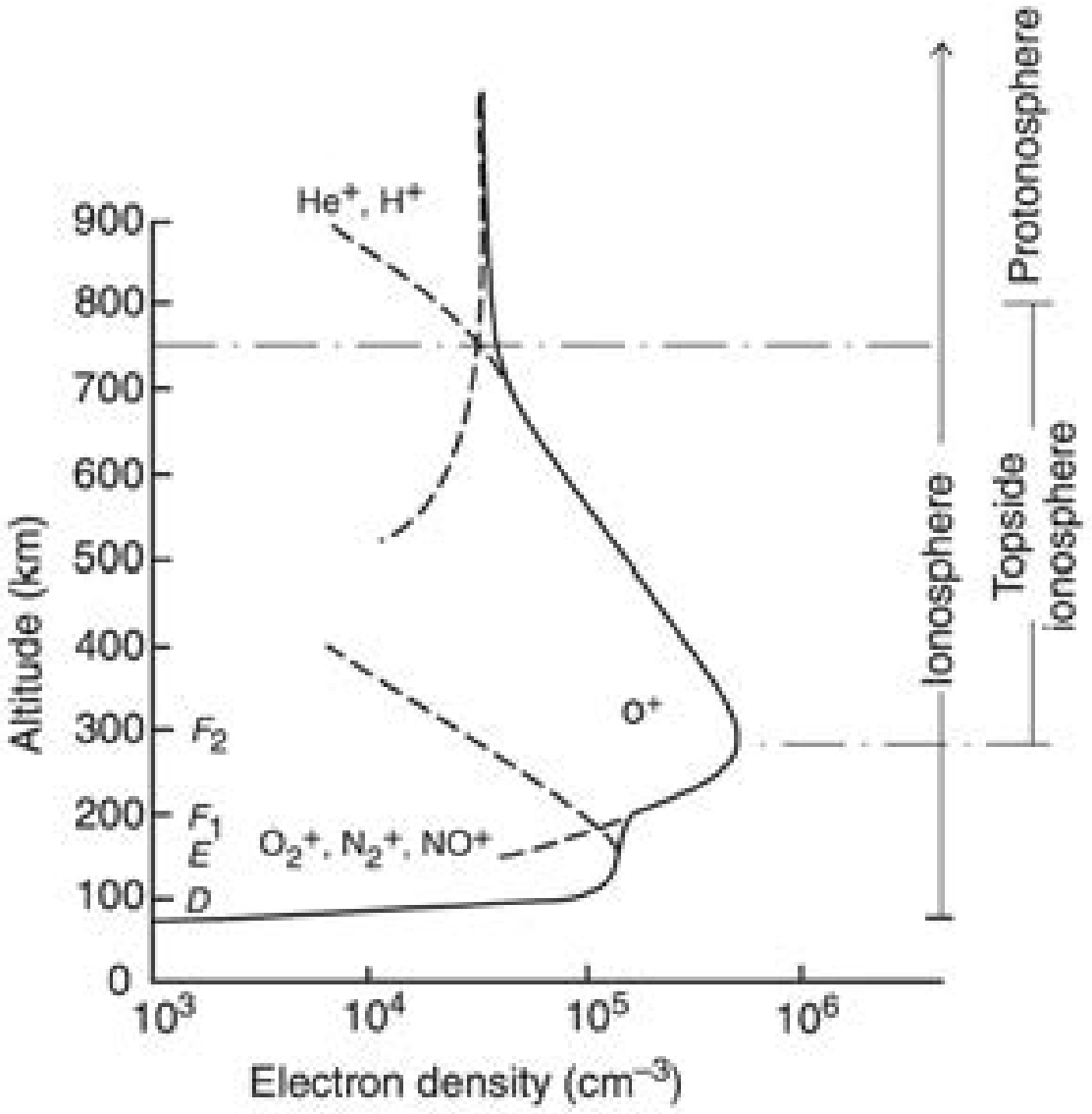

Figure 1.4: The height versus electron density profile of the ionosphere. The peak densities and major ion species of the D, E, F_1, and F_2 layers are shown. Adapted from Figure 2.16 of *Schunk and Nagy* (2009).

each species varies exponentially as shown in Equation 1.4.

$$n(z) = n(z_0)e^{-\frac{z-z_0}{H}} \tag{1.4}$$

The n is the number density of the species, z is the altitude, z_0 is the base altitude and H is the scale height. The expression for scale height is shown in Equation 1.5.

$$H = \frac{kT}{mg} \tag{1.5}$$

The scale height depends on the Boltzmann coefficient (k), ambient temperature (T), molecular weight of the constituent (m) and the gravity (g). The most common species in the thermosphere are H, He, O, N_2 and O_2. The solar activity dependent altitude profiles for these species are shown in Figure 1.5. During solar maximum (left), the thermospheric temperatures are higher, leading to higher thermospheric density at high altitudes. During solar minimum (right), the lower thermospheric temperatures cause the constituents to condense.

1.2 The Geospace System Coupling

The solar wind, magnetosphere, ionosphere and thermosphere systems are intrinsically coupled with each other, which makes studying the propagation of perturbations very difficult because of the different dominant particles and physical processes in each region.

1.2.1 Solar Wind - Magnetosphere Interaction

The magnetospheric processes are controlled by the solar wind and interplanetary magnetic field [*Kamide and Chian* (2007)]. The plasma flow from the Sun, determines the shape and size of the Earth's magnetic dipole field. The established equilibrium between the solar wind and the Earth's magnetic dipole gives rise to a magnetic

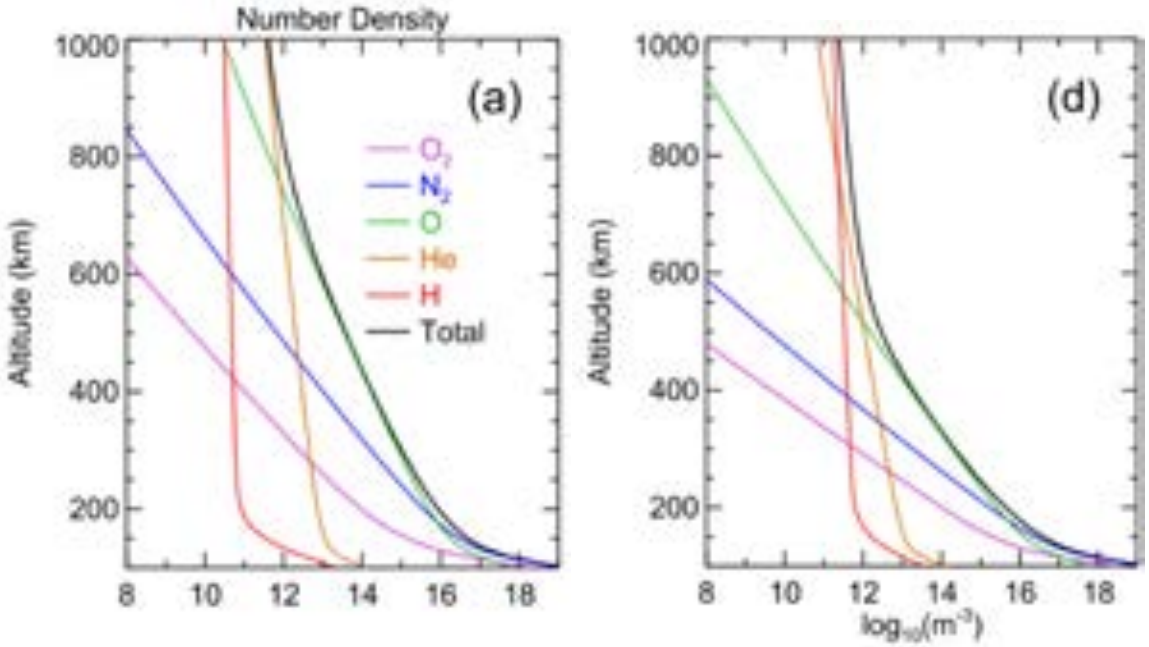

Figure 1.5: The global averaged number density profiles of total (black) and major thermospheric constituents during solar maximum (left) and solar minimum (right), derived from NRLMSISE-00 model. Adapted from Figure 2.a and 2.d of *Emmert* (2015).

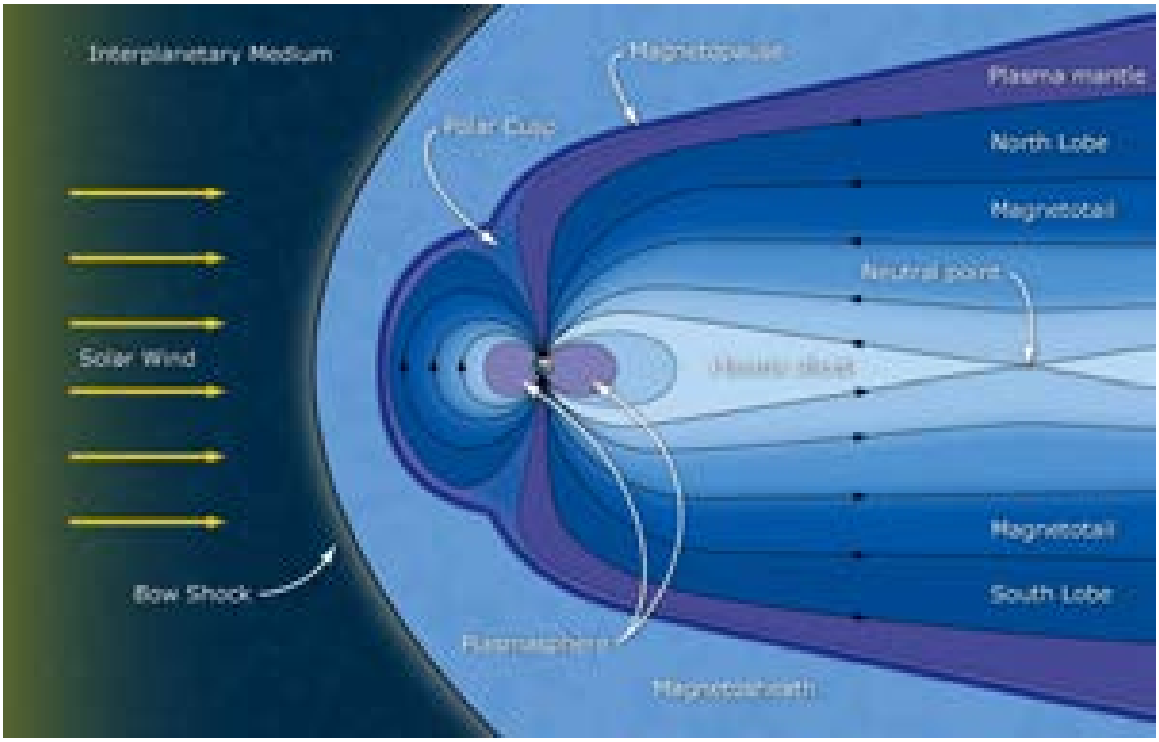

Figure 1.6: Illustration of Earth's magnetosphere and its interaction with the solar wind. The Sun is to the left of the image. The illustration shows Earth's bow shock, magnetosheath, magnetopause, magnetotail, plasmasphere and plasma sheet. (The illustration is taken from: *www.nasa.gov/mission_pages/ibex/news/spaceweather.html*)

configuration as shown in Figure 1.6.

1.2.1.1 Bow Shock

The bow shock is the shock that forms in front of the Earth's magnetosphere due to its interaction with the supersonic solar wind [*Gombosi* (2004)]. The formation of the bow shock slows down the solar wind and diverts its flow around the Earth. The jump conditions that describe the plasma properties after the bow shock are given below.

$$\rho_2 = \frac{\gamma + 1}{\gamma - 1}\rho_{SW} \tag{1.6}$$

$$u_{t_2} - u_{SW_t} = \frac{2}{\gamma - 1} \frac{B_{SW_n} - B_{SW_t}}{\mu_0 \rho_{SW} u_{SW}} \tag{1.7}$$

Here, the ρ_{SW}, u_{SW}, B_{SW_n}, and B_{SW_t} are solar wind density, speed, normal and tangent components of the magnetic field. The solar wind specific heat, γ is taken as 5/3. The downstream conditions denoted with ρ_2 and u_{t_2} define the properties of the plasma in between the bow shock and the Earth's magnetosphere, at a region called the magnetosheath.

1.2.1.2 Magnetosheath

The region between the bow shock and the Earth's magnetosphere is called the magnetosheath [*Gombosi* (2004), *Kivelson and Russell* (1997)]. Passing through the bow shock the solar wind plasma decelerates and its kinetic energy transforms into thermal energy. Thus, the plasma in this region is thermalized and the flow becomes subsonic [*Kamide and Chian* (2007)].

1.2.1.3 Magnetopause

The ram pressure contribution to solar wind is the highest compared to thermal and magnetic pressure. The magnetopause is the location where Earth's magnetic field pressure balances the solar wind pressure. This relation is shown in Equation 1.8.

$$\rho_{SW}^2 u_{SW}^2 = \frac{B_{MS}^2}{2\mu_0} \tag{1.8}$$

Here the ρ_{SW} is the solar wind density, u_{SW} is the solar wind speed, B_{MS} is the magnetosheath magnetic field, and μ_0 is the permeability. As the solar wind dynamic pressure increases, the left hand side of Equation 1.8 increases and pushes Earth's magnetosheath inward.

The magnetopause standoff distance can be expressed at the equator using the Earth's dipole field which is shown in Equation 1.1.

$$R_{MP} = \left(\frac{B_0^3}{2\mu_0 \rho_{SW} u_{SW}^2} \right)^{1/6} \tag{1.9}$$

Here the R_{MP} is the magnetopause standoff distance, B_0 is the magnetic field strength at the Earth's surface (equator). The magnetopause radius strongly depends on the solar wind dynamic pressure, however it also depends on the z-component of the IMF. *Shue et al.* (1997) derived an empirical formula for the magnetopause standoff distance as a function of solar wind dynamic pressure and IMF B_Z. This formula is shown in Equation 1.10.

$$r = 2^{\alpha} r_0 (1 + cos\theta)^{-\alpha} \tag{1.10}$$

where α is:

$$\alpha = (0.58 - 0.007 B_Z)[1 + 0.024 ln(P_d)] \tag{1.11}$$

and the r_0 is given by:

$$r_0 = [10.22 + 1.29 tanh(0.184(B_Z + 8.14))] \left(\frac{1}{P_{SW}} \right)^{1/6.6} \tag{1.12}$$

Here r is the radial distance and θ is the solar zenith angle.

The magnetopause is a tangential discontinuity [*Kamide and Chian* (2007)]. It is blunt on the dayside but is stretched towards the tail [*Kivelson and Russell* (1997)]. There are other factors that affect the shape and size of Earth's magnetosphere related to the plasma properties, especially on the magnetotail.

Chapman-Ferraro currents

A boundary current system forms in between the solar wind plasma and the Earth's magnetic field at the magnetopause, which is known as *Chapman-Ferraro currents*

due to oppositely moving electrons and positively charged particles [*Kivelson and Russell* (1997)]. The strength of the Chapman-Ferraro current at the magnetopause can be expressed as shown in Equation 1.13.

$$I = \frac{2\rho_{SW}}{B_Z} u_{SW}^2 \tag{1.13}$$

Here the B_Z is the magnetic field strength of the Earth's dipole at the magnetopause.

1.2.1.4 Inner Magnetosphere

The inner magnetosphere is the region between 1000 km to geostationary orbits (6-7 R_E), consisting of two distinct plasmas, the plasmasphere and the radiation belts.

Plasmasphere

The plasmasphere is the region where high densities of cold plasma (1eV) exist. The source for this cold plasma is believed to be the upper ionospheric particles that escaped from the gravitation field of the Earth [*Kivelson and Russell* (1997)]. The plasmasphere is dominated by H^+, but He^+, O^+, O^{++}, N^+ and N^{++} are also observed. This cold plasma resides in the low and middle latitude regions in the closed field lines near the Earth.

Radiation Belts

The radiation belts are the regions of trapped energetic particles (MeV) [*Kamide and Chian* (2007)]. The particle population is higher in the equatorial plane and lower at the higher latitudes due to losses to the neutral atmosphere [*Kivelson and Russell* (1997)]. During geomagnetically active periods the radiation belt particle density and energy increases.

Ring Current

The inner magnetospheric trapped particles with energy ranges between 10 to 200 keV

propagate in closed trajectories due to gradient curvature drift [*Gombosi* (2004)]. The positively charged particles drift westward, whereas electrons drift eastward creating a current along the equatorial plane which is called the ring current. During storm time the ring current increases, creating an overall drop in the geomagnetic field which can be measured with the Disturbed Storm Time (D_{st}) index [*Gombosi* (2004)].

1.2.1.5 Magnetotail

The solar wind stretches Earth's magnetic dipole away from the Sun [*Kivelson and Russell* (1997)] and creates an elongated magnetosphere on the nightside. A current sheet divides the magnetotail into two: the northern tail lobe and the southern tail lobe. The tail lobes map to the corresponding nightside polar ionospheres. An estimate of the magnetic flux in the tail lobe is given in Equation 1.14.

$$\Phi_T = \frac{1}{2}\pi R_T^2 B_T \tag{1.14}$$

Here Φ_T is the magnetic flux, R_T is the tail radius and B_T is the tail magnetic field strength.

Based on the definition of the magnetopause, the magnetotail should be in pressure balance with the solar wind at the boundary. This pressure balance yields to an estimate of the shape and size of the magnetotail as shown in Equation 1.15.

$$\rho u_{SW}^2 sin^2\alpha + p_0 = \frac{B_T^2}{2\mu_0} \tag{1.15}$$

Here p_0 is the isotropic pressure of the solar wind and α is the flaring angle that determines the shape of the magnetotail. Observations have shown that the magnetotail can extend to 230 R_E in the anti sunward direction [*Kivelson and Russell* (1997)]. The flaring angle decreases with the tail distance.

Plasma sheet

The plasma sheet, or central plasma sheet, is a region in the magnetotail that extends closer to the Earth [*Gombosi* (2004)]. The plasma sheet lies on the stretched but closed field lines and has a population of hot particles. At the magnetotail, this current sheet is names as **tail current sheet**.

1.2.1.6 Dungey Cycle

As discussed above, the IMF B_Z plays an important role in magnetospheric physics, because of a phenomenon called **magnetic reconnection**. The magnetic reconnection is still a widely studied concept, which is based on the merging of oppositely aligned magnetic fields to form new magnetic field lines [*Gombosi* (2004)]. *Dungey* (1961) was first to suggest a steady circulation of the magnetospheric plasma through a series of magnetic reconnection events. They showed that when the IMF B_Z was southward, it will reconnect with the Earth's magnetic dipole field (1), then the frozen-in magnetic fields would be stretched tailward by the solar wind (2). In the magnetotail, these fields would be predominantly in the x-direction, with one end connected to the poles, and the other in the solar wind. The open field lines would then achieve a closed state [*Kivelson and Russell* (1997)] by reconnecting in the Earth's magnetotail (3). This reconnection would create one terrestrial closed field line, and a plasmoid that would be released to the interplanetary medium to merge with the solar wind. On the other hand the newly reconnected terrestrial field line would propagate in the sunward direction (4) and would flow around either the dawn or the dusk side of the Earth (5) back to the dayside (6) [*Kivelson and Russell* (1997)]. This steady circulation of the magnetospheric field lines is called the *Dungey cycle* and has crucial importance in understanding the magnetosphere-ionosphere interaction. The schematic representation of the Dungey cycle is show in Figure 1.7.

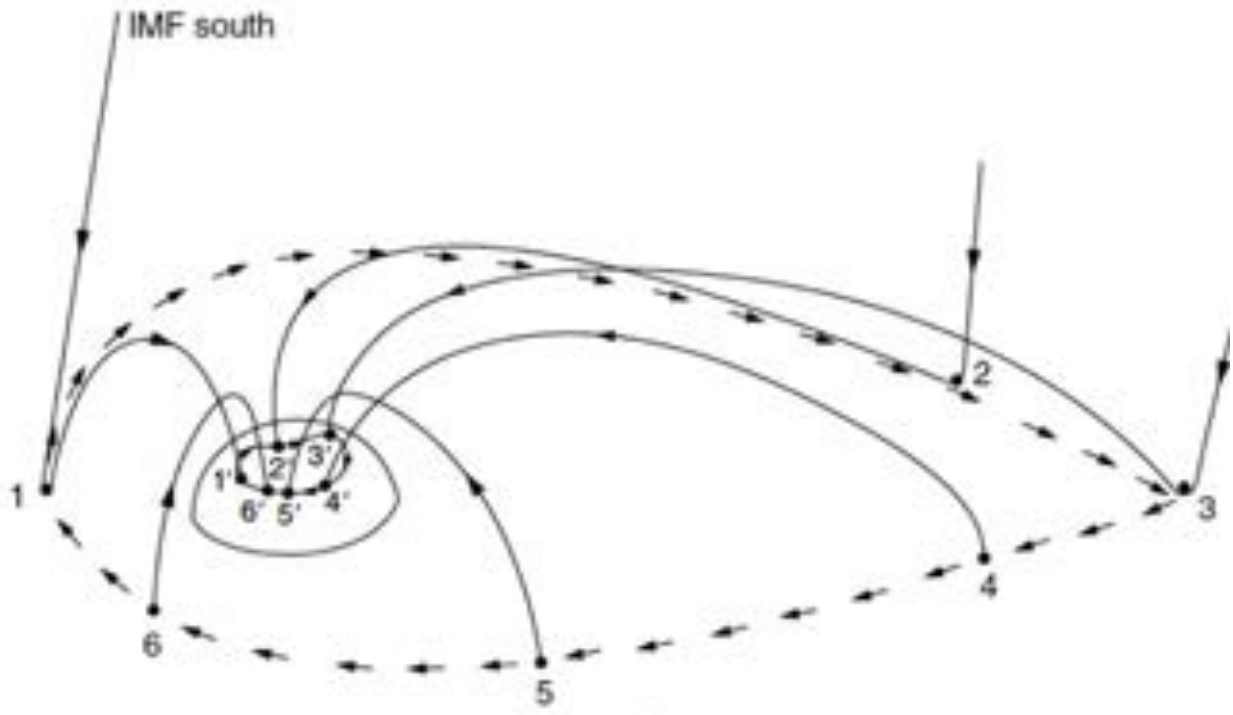

Figure 1.7: A schematic diagram showing the magnetospheric convection of magnetic field lines under southward IMF B_Z. The numbers show the magnetic field lines and their ionospheric counterparts. Adapted from Figure 8.15b in *Kelley* (2009).

1.2.2 Magnetosphere - Ionosphere Interaction

1.2.2.1 Convection in the Ionosphere

The Dungey cycle explains the steady convection of magnetic field lines in the magnetosphere. These magnetic field lines are connected to the Earth in the high-latitude regions. As the magnetic field lines reconnect and propagate anti-sunward (1'), the convection electric field ($E_{SW} = u_{SW}\mathrm{x}B_{SW}$) will drive the ionospheric flow from noon towards midnight (2') [*Kivelson and Russell* (1997)]. The convection electric field in the polar cap due to this motion can be estimated with $u_{PC}\mathrm{x}B_{PC}$. Here u_{PC} is the ionospheric convection velocity, whereas B_{PC} is the magnetic field vector at the polar cap. As the magnetic field lines reconnect in the tail and propagate earthwards, the plasma is convected from midnight (3') towards the dayside (4', 5', 6'). The mapping of the magnetospheric convection as electric field potentials to the top of ionosphere in MLT coordinates can be seen in Figure 1.8. This type of convection is called the *two-cell convection pattern* [*Schunk and Nagy* (2009)].

The two-cell convection pattern strictly depends on the interaction of Earth's magnetosphere with the IMF. Observations have shown that when IMF B_Z is southward and IMF B_Y is zero, the convection pattern resembles the two-cell convection pattern. However as shown in Figure 1.9 the potential drops between cells are distributed asymmetrically when the y-component of the IMF changes.

When IMF B_Z is southward, the convection is anti-sunward with the dawn cell being larger when the y component of the IMF is negative and the dusk cell being larger when the y component is positive. However, when B_Z is northward, sunward convection can be observed. There can be up to 4 convection cells when B_Y is zero, with dawn cells being dominant during negative y, and dusk cells being dominant during positive y.

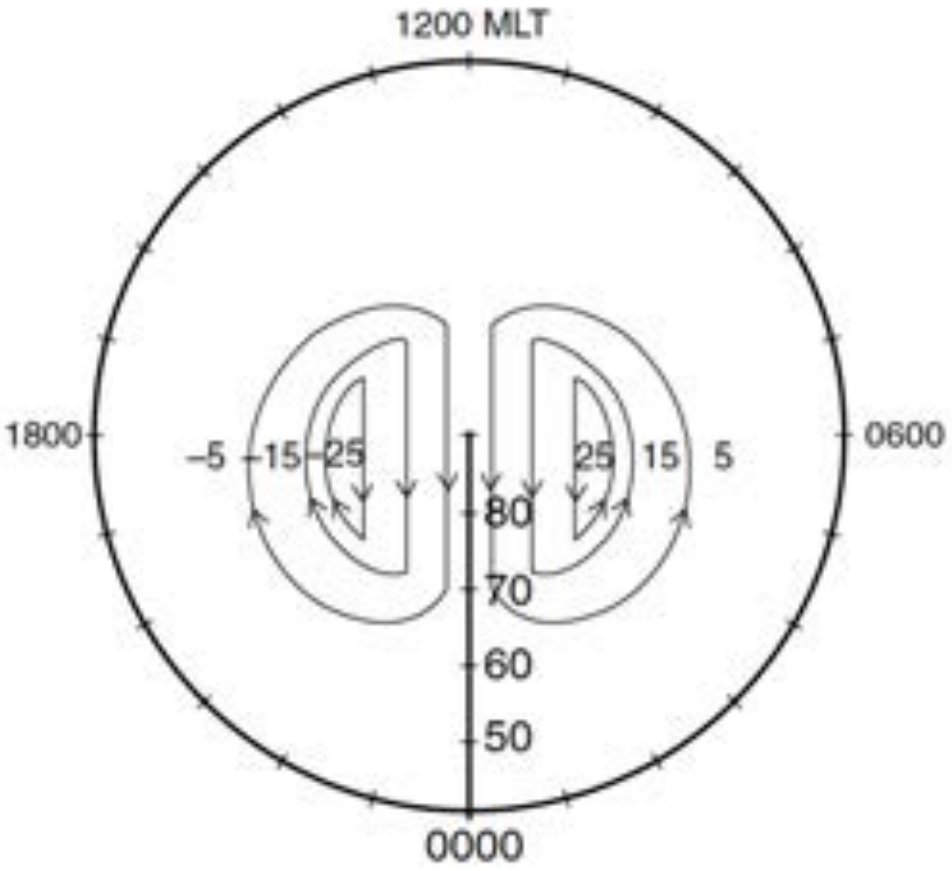

Figure 1.8: The two cell convection pattern in the ionosphere is shown in MLT coordinates. The contours are magnetospheric electrostatic potentials. Adapted from Figure 12.4 of *Schunk and Nagy* (2009).

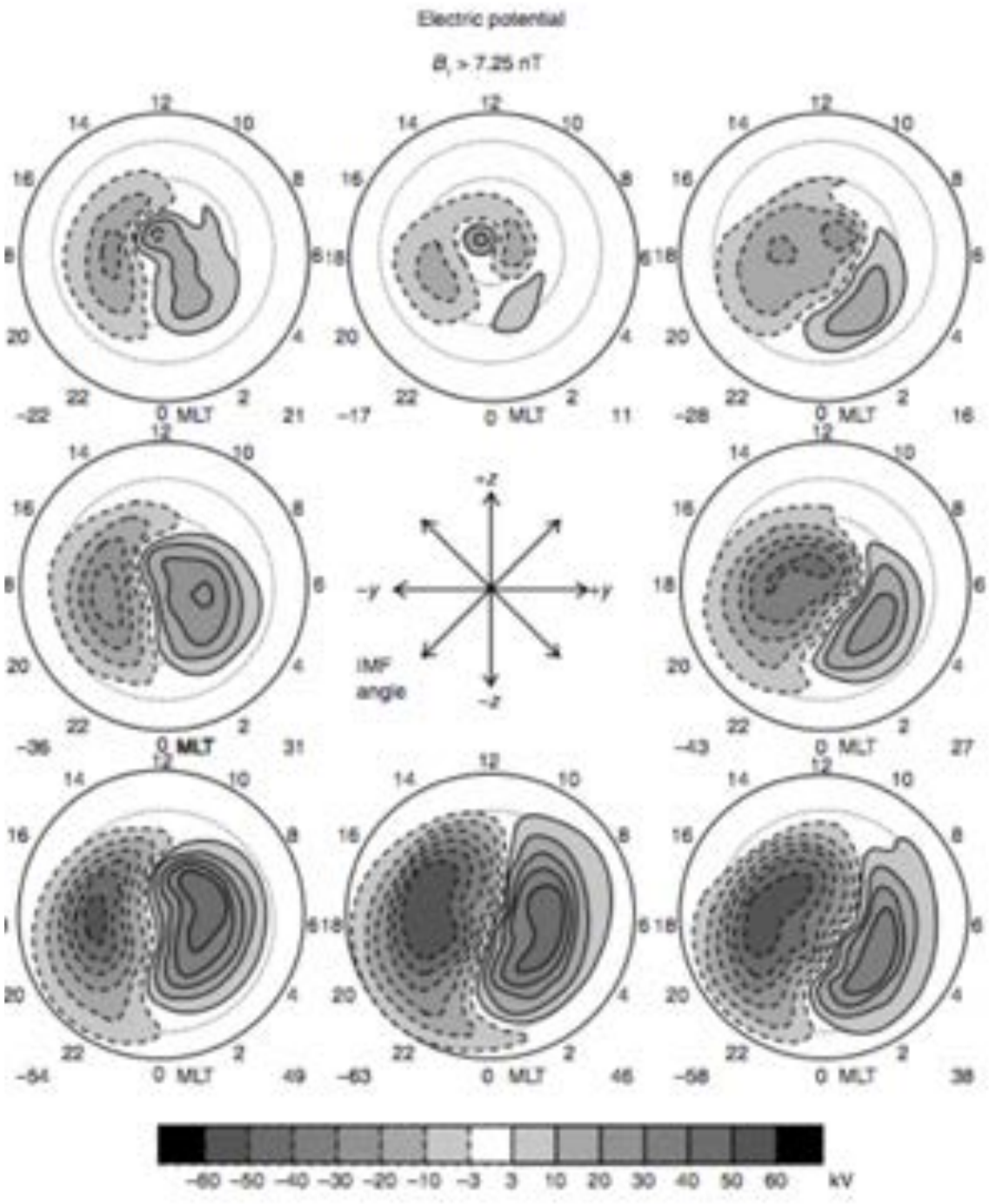

Figure 1.9: Electric potential contours under different IMF B_Y and B_Z derived from an empirical model. Adapted from Figure 12.4 of *Schunk and Nagy* (2009).

1.2.2.2 Region 1 and Region 2 currents

In the high-latitude regions, statistically there are two pairs of field-aligned currents, named Region-1 and Region-2 FACs. The Region 1 currents, which map to higher latitudes, form as a result of the solar wind interaction with the Earth's magnetosphere [*Kivelson and Russell* (1997)]. The Region 1 current is upward on the dusk and downward on the dawn sector.

The Region 2 FACs form as a result of the divergence of the partial ring current in the inner magnetosphere. They flow downward on dusk and upward on dawn sectors, mapping to lower latitudes than the Region 1 current systems.

During Northward IMF B_Z, an *NBZ current system* forms. This current has an upward FAC on dawn and upward FAC on dusk sector mapping to slightly higher latitudes than the Region 1 currents.

1.2.2.3 Ionospheric currents

The conductivity along the magnetic field lines is very high, but it is lower in the ionospheric altitudes compared to in the magnetosphere. At these altitudes the conductivity perpendicular to the magnetic field gains significance as a result of collisions between charged particles and the neutral atmosphere. These collisions give rise to two important major ionospheric currents known as *Pedersen* and *Hall* currents [*Schunk and Nagy* (2009)]. The electron gyrofrequency is much higher than the ion gyrofrequency, so the electrons are magnetized in the ionospheric altitudes and act as if there are no neutrals. On the other hand, the ions are significantly affected by the neutral particles. The different responses of electrons and ions results in deviation of their drifts in the E region and thus the charge separation forms horizontal currents. Therefore the Hall current is perpendicular to both magnetic and electric fields [*Kivelson and Russell* (1997)]. The horizontal current in the ionosphere then can be written as shown in Equation 1.16.

$$\mathbf{J}_\perp = \mathbf{\Sigma_P E}_\perp + \mathbf{\Sigma_H \hat{e_B} x E} \tag{1.16}$$

Here $\mathbf{\hat{e_B}}$ is the unit vector in the direction of the magnetic field, Σ_P and Σ_H are the height-integrated Pedersen and Hall conductances which depend on the collision frequencies.

1.2.2.4 Conductance in the Ionosphere

The conductance of the ionosphere controls the energy transfer between the solar wind, magnetosphere, ionosphere and thermosphere systems. The conductivity profiles depend on the strength of the magnetic field, density of electrons, ions and neutrals.

Pedersen conductivity

The expression for the Pedersen conductivity is shown in Equation 1.17 below.

$$\sigma_P = \Sigma_i \sigma_i \frac{\nu_i^2}{\nu_i^2 + \omega_{c_i}^2} + \sigma_e \frac{\nu_e^2}{\nu_e^2 + \omega_{c_e}^2} \tag{1.17}$$

Here σ_i is the ion conductivity, shown in Equation 1.18, ν_i is the ion collision frequency, ω_{c_i} is the ion gyroradius, σ_e is the electron conductivity, shown in Equation 1.19 and the ω_{c_e} is the electron gyroradius.

The ion and electron conductivities are shown below. Here the n denotes density, m denotes the mass, e denotes the charge and ν denotes the collision frequency of the species with the neutrals. The subscripts i and e shows the species of ions and electrons.

$$\sigma_i = \frac{n_i e_i^2}{m_i \nu_i} \tag{1.18}$$

$$\sigma_e = \frac{n_e e_e^2}{m_e \nu_e} \tag{1.19}$$

Hall conductance

The expression for the Hall conductivity is shown in Equation 1.20 below.

$$\sigma_H = -\Sigma_i \sigma_i \frac{\nu_i \omega_{c_i}}{\nu_i^2 + \omega_{c_e}^2} + \sigma_e \frac{\nu_e \omega_{c_e}}{\nu_e^2 + \omega_{c_e}^2} \tag{1.20}$$

The typical altitude profiles of the specific, Hall and Pedersen conductances at mid-latitude, daytime are shown in Figure 1.10. The Hall conductivity is significantly larger than the Pedersen conductivity below 130 km. The specific conductivity is the most dominant term above 250 km. The conductivities depend on electron density. Therefore any cause of source or temperature variation can affect the vertical profile. Conductivities are generally weaker at the nightside, as well as at the winter hemispheres due to the lower temperatures and electron densities. in the absence of strong electron precipitation.

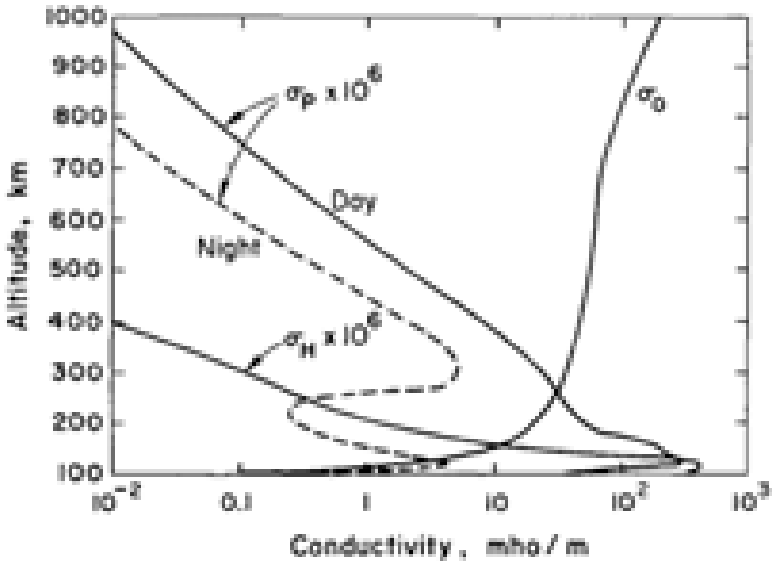

Figure 1.10: The altitude profiles of the specific,Hall and Pedersen conductivities are shown. Adapted from Figure 2.6 of *Kelley* (2009).

1.2.2.5 Energy transfer from the Magnetosphere

The mass, momentum and energy transfer from the magnetosphere to the ionosphere can be summarized in two categories: *particle precipitation* and *joule heating*.

Particle precipitation

Magnetospheric particles are lost in Earth's atmosphere due to processes known as *pitch-angle scattering* and *charge exchange* [*Kivelson and Russell* (1997)]. Especially during high geomagnetic activity, due to the violation of the first adiabatic invariant high levels of auroral precipitation is observed. Magnetospheric ions can also collide with low energy neutrals resulting in charge exchange and loss of the charged particle.

Poynting Flux

The downward propagating Poynting flux from the magnetosphere can also transfer energy to the ionosphere-thermosphere system by acting against **jxB** forces. The expression for Poynting Flux is shown in Equation 1.21.

$$\mathbf{S} = \frac{\mathbf{E} \times \mathbf{B}}{\mu_0} \tag{1.21}$$

This applied electromagnetic force is dissipated parallel to Pedersen currents [*Kivelson and Russell* (1997)] at high latitudes through Joule heating. When the different between ion and neutral velocities are higher, the frictional heating increases, as shown in Equation 1.22 [*Schunk and Nagy* (2009)].

$$T_i - T_n = \frac{m_n}{3k}(v_i - v_n)^2 \tag{1.22}$$

1.2.3 Ionosphere - Thermosphere Interaction

1.2.3.1 Transport

Transport is one of the most dominant processes in the high latitude ionosphere which causes density variations. This motion can be examined in two categories, first

is the horizontal transport which was discussed in detail in Section 1.2.2.1 and the other is the vertical transport which will be discussed in this section. The charged particles are constrained to the inclined magnetic field, however the body forces acting on them are in the vertical direction [*Schunk and Nagy* (2009)]. The inclination angle becomes larger in the middle and lower latitudes, further complicating the transport process at these regions. The general form of the ion diffusion equation is shown in Equation 1.23.

$$u_{iz} = \frac{E}{B} cosI + u_n sinI cosI - sin^2 I D_a \left(\frac{1}{n_i} + \frac{1}{T_p} \frac{\partial}{\partial z} + \frac{1}{H_p} \right) \tag{1.23}$$

Here u_{iz} is the ion diffusion in the vertical direction, I is the magnetic inclination angle, u_n is the neutral wind speed, D_a is the diffusion coefficient (shown in equation 1.24) and H_P is the scale height of the plasma. The first term on the right hand side describes the vertical component of the **E** x **B** drift, the second term shows the contribution from the neutral winds and the last term shows the affects of the body forces along the stratified ionosphere.

$$D_a = \frac{2kT_p}{m_i \nu_{in}} \tag{1.24}$$

The ion diffusion equation is a good estimate for the ion vertical motion at middle and low latitudes however it neglects the heat flow collision terms which are important in higher latitudes and altitudes [*Schunk and Nagy* (2009)].

1.2.3.2 Chemistry

The four main processes are photoionization, impact ionization, ion-molecule reactions and electron-ion recombination *Schunk and Nagy* (2009). Photochemistry is more important than transport at lower altitudes of the ionosphere.

Photoionization

Photoionization is the process in which a photon produces free electron-ion pairs from neutral particles and it is a major source of ionospheric plasma [*Schunk and Nagy* (2009)]. The three major photoionization processes for the terrestrial upper atmosphere are shown in equations 1.25-1.27.

$$O + h\nu \rightarrow O^+ + e^- \tag{1.25}$$

$$O_2 + h\nu \rightarrow O_2^+ + e^- \tag{1.26}$$

$$N_2 + h\nu \rightarrow N_2^+ + e^- \tag{1.27}$$

Impact Ionization

Impact ionization is the ionization process that occurs when an energetic particle, such as electrons, ions, or cosmic rays, collides with a neutral constituent in the atmosphere, and delivers sufficient energy to overcome the neutral's ionization potential [*Kivelson and Russell* (1997)]. The major magnetospheric source of such energized particles are the precipitating electrons, which can form the aurora, with energy ranges between 100 eV to 100 keV [*Kelley* (2009)]. As opposed to photons, an energetic particle gradually loses its energy through impact ionization, which can lead to *primary* and *secondary electrons* [*Kivelson and Russell* (1997)]. The impact ionization process is shown in equation 1.28.

$$A + e^- \rightarrow A^+ + 2e^- \tag{1.28}$$

Here A is any neutral constituent in the atmosphere that has an ionization energy equal or lower to the energy the electron can deposit [*Shang* (2018)]. Impact ionization is particularly important at auroral latitudes due to the precipitation energetic particles from the plasma sheet.

Ion-molecule reactions

The ion molecule reactions are the charge exchanges that occur between a neutral and an ion.

$$O^+ + N_2 \rightarrow NO^+ + N \tag{1.29}$$

$$O^+ + O_2 \rightarrow O_2^+ + N \tag{1.30}$$

$$N_2^+ + O_2 \rightarrow O_2^+ + N_2 \tag{1.31}$$

$$N_2^+ + O \rightarrow O^+ + N_2 \tag{1.32}$$

$$N_2^+ + O \rightarrow NO^+ + N \tag{1.33}$$

Electron-Ion Recombination

When an ion and an electron collide, the free electron recombines with the ion and produces neutrals. Below are some typical dissociative recombination reactions occurring in the Earth's ionosphere.

$$NO^+ + e^- \rightarrow N + O \tag{1.34}$$

$$O_2^+ + e^- \rightarrow O + O \tag{1.35}$$

$$N_2^+ + e^- \rightarrow N + N \tag{1.36}$$

1.2.3.3 Temperature and Transport in the Thermosphere

In addition to responding to the magnetospheric drivers through the ionosphere, the behaviour of the thermosphere system is also affected by lower atmospheric drivers. The equations that describe thermospheric response are discussed below.

Momentum equation

The motion of the thermospheric particles depends on the forces acting on the neutrals. For the terrestrial atmosphere, the Coriolis force and the gravitational force

are two important examples of such forces. In addition, significant pressure gradients arise due to solar EUV heating, between summer and winter hemispheres as well as daytime versus nighttime sectors. Viscous interactions also decrease the velocity of the neutral particles [*Kelley* (2009)]. Even though neutral particles do not respond to electromagnetic fields directly, collisions with ions change their momentum. The ion drag term becomes more important at higher latitudes. The resulting momentum equation for neutral particles is shown in Equation 1.37.

$$\frac{D\mathbf{u_h}}{Dt} = -\frac{1}{\rho}\nabla_{\mathbf{h}}\mathbf{P} - \mathbf{2\Omega x u_h} + \mathbf{g} + \frac{\mathbf{1}}{\rho}\nabla(\mu\nabla\mathbf{u_h}) - \nu_{\mathbf{ni}}(\mathbf{u_h} - \mathbf{u_i}) \tag{1.37}$$

The first term on the right hand side describes the effect of the pressure gradient, the second term is the Coriolis force, the third term is the gravitational force, the fourth term is the viscous diffusion and the last term is the ion drag.

Temperature variation

The temporal variation of the neutral temperature can be estimated using the momentum and energy equations.

$$\frac{dT_n}{dt} = \frac{1}{\rho C_p}\left[\left(\Sigma_{ions}\frac{n_n m_n \nu_{ni}}{m_i + m_n}\left[3k(T_i - T_n) + m_i(\mathbf{u_i} - \mathbf{u_n})^{\mathbf{2}}\right]\right) - \frac{\partial}{\partial z}\left(\lambda_n \frac{\partial T_n}{\partial z}\right)\right] \tag{1.38}$$

The first term in the right hand side is the collisional heat transfer rate, the second term is the frictional heat transfer rate and the third term is the vertical heat conduction rate.

1.2.4 Magnetic Perturbations at the Ground

As discussed in the Section 1.2.1.1., the solar wind plasma and the Earth's magnetosphere are in a pressure balance. When an earthward propagating interplanetary shock or a high-speed stream interacts with the Earth, the momentum exerted by the solar wind on the magnetosphere increases. To balance the new pressure, the Earth's

magnetopause moves radially inward. As a result of this motion, the Chapman-Ferraro currents at the magnetopause are strengthened. This compression of the magnetosphere can be detected by ground magnetometers at Earth's surface [*Kivelson and Russell* (1997)], and is traditionally named as a *sudden impulse (SI)* or a *storm sudden commencement (SSC)* if followed by a geomagnetic storm. The Biot-Savart integral can be used to estimate the magnetic perturbations on the ground as shown in Equation 1.39.

$$\mathbf{B} = \frac{\mu_0 \mathbf{I}}{\mathbf{2r}} \mathbf{e_z} \tag{1.39}$$

Here the I is the current at a circular loop, B is the magnetic field at the center of the current loop, r is the radius of the current loop and z is the axis perpendicular to the plane of the current. Chapman-Ferraro, FACs, ring current are some examples of the currents detected by ground magnetometers.

The ground magnetometers use the HDZ or NEZ coordinate systems. These coordinate systems can be inferred from Figure 1.11, where H is the horizontal component of the magnetic field strength, D is the declination angle between the North (N, along x) and H components, E is the eastward component along y, and the z component is in the nadir direction [*Schunk and Nagy* (2009)].

Ground magnetometer measurements have shown that the SI signatures at lower latitudes were in the form a step-wise enhancement, however at higher latitudes the SI could be decomposed into two consecutive signals as shown in Figure 1.12. The magnetometers recorded a positive short-lived impulse that is positive on the morning and negative on the afternoon sectors, named *preliminary impulse* (PI). This signal is succeeded by a longer-lived signal that is negative on the morning and positive on the afternoon sectors, called a *main impulse* (MI). Other studies [*Shinbori et al.* (2009); *Sun et al.* (2014)] also investigated the PI-MI dependences on magnetic latitude and longitude; nevertheless, due to sparsity of ground magnetometers, a global sense of

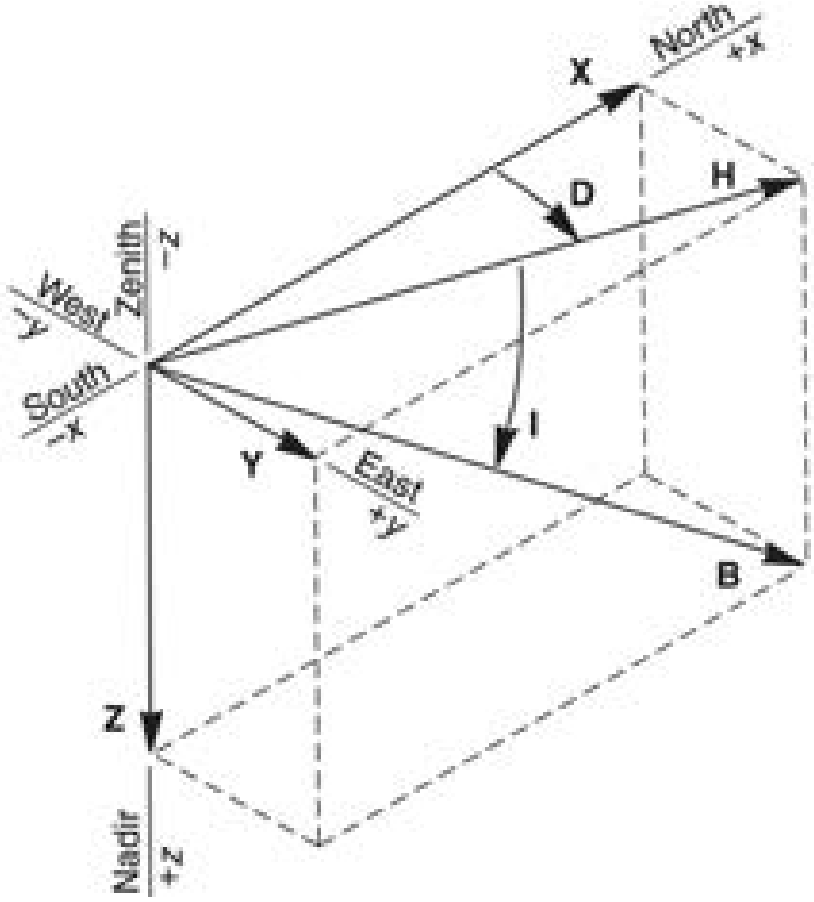

Figure 1.11: The HDZ and NEZ coordinate system. Adapted from Figure 11.3 of *Schunk and Nagy* (2009).

variation under different solar wind conditions has not been established.

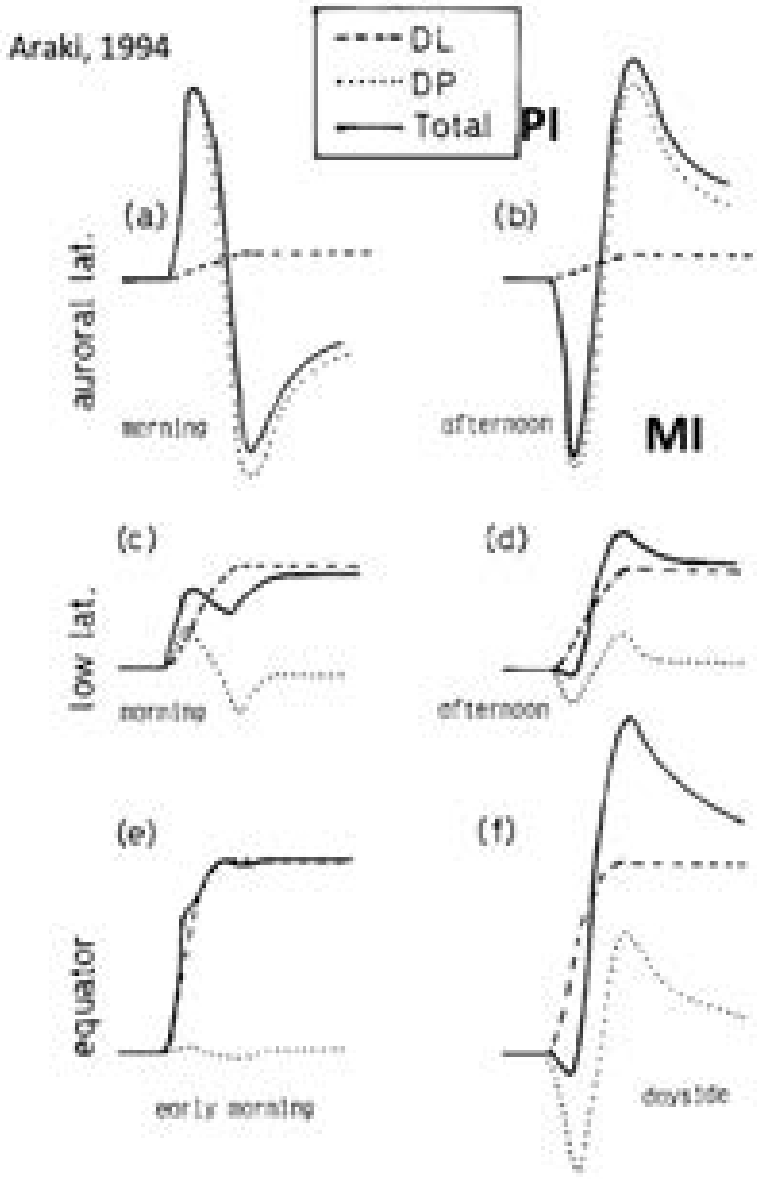

Figure 1.12: The magnetic field perturbations associated with sudden commencement at different latitudes and local times. Adapted from *Araki* (1994b).

1.3 Purpose of the Study

In this chapter, the properties, physics and the plasma processes that define the magnetosphere, ionosphere and thermosphere systems were described. Being in a constant pressure balance with the solar wind, the Earth's geospace system is highly responsive to the variations in the solar wind dynamic pressure, making it one of the major driver of the space weather events in the near Earth environment. However, isolating the effects of dynamic pressure is not trivial due to various reasons. One important reason is that Earth's magnetosphere also responds to the changes in the IMF which is carried by the solar wind. In addition, the perturbations in the solar wind and IMF are oscillatory. This results in a constant variability in the geospace system's response, making it harder to associate certain responses to the drivers. Furthermore, the Earth's own M-I-T systems can be very dynamic and the conditions of these systems are determined by the Earth's rotation and orbital motions. Apart from the difficulties resulting from the complexity of the geospace system, there are also operational limitations, such as the scarcity of observatories, infrequency of experiments and low temporal and spatial resolution of the measurements.

The MHD modeling has been a very important component of geospace system research because with the recent state of the modeling capabilities, the aforementioned limitations can be easily eliminated. However one caveat still needs to be addressed, which is the missing particle physics in the MHD models. Absence of such processes results in misrepresentation of important magnetospheric processes such as dayside and nightside reconnection, auroral precipitation and conductivity. Therefore, it is very important to validate model results with case studies and provide comparisons with measurements when available. For this reason, two chapters of this work are devoted to case studies.

Another caveat, which arises when modeling the I-T system, is that some processes are described through empirical models, such as conductance, convection electric fields

and particle precipitation. These empirical approaches are known to average out small perturbations, especially when different systems are coupled, resulting in lower energy and momentum transfer rates in simulations. Also, these observation based empirical models do not respond to enhancements in the solar wind density. This problem will be discussed further in Chapter 4, but it constitutes one of the main motivations of the study which is to represent the magnetospheric perturbations caused by the solar wind dynamic pressure, by using the physics-based solutions to drive the I-T model.

With this approach, this study aims to answer:

1. What is the role of IMF B_Y in determining the ground magnetometer response to solar wind dynamic pressure enhancement events?
2. How are the I-T systems affected by the magnetospheric compression due to solar wind dynamic pressure enhancement?
3. What are the magnetospheric and ionospheric responses to a solar wind dynamic pressure decrement event?
4. How are the I-T systems affected by the magnetospheric decompression due to solar wind dynamic pressure decrement?
5. What are the differences of geospace responses to the solar wind dynamic pressure enhancement and decrement events?

CHAPTER II

The Global Model of the Geospace System

In order to understand the global geospace system responses to solar wind dynamic pressure variations, we used the Space Weather Modeling Framework (SWMF) [*Toth et al.* (2005)]. The simulations were run on the Ceheyenne and Yellowstone supercomputer clusters operated by the National Center for Atmospheric Research (NCAR). The SWMF has different components that account for different physics domains. In this study we used the global magnetosphere (GM), inner magnetosphere (IM), and ionosphere electrodynamic (IE) components to simulate the impulsive dynamic pressure variations and the geospace system response to such events.

2.1 The Ideal Magnetohydrodynamic Equations

The evolution of the Earth's magnetosphere under solar wind driving can be approximated by the ideal MHD equations. These equations consist of macroscopic transport equations for a gas and Maxwell's equations [*Gombosi* (2004)]. These equations are the conservation of continuity (Equation 2.1), conservation of momentum (Equation 2.2), induction (Equation 2.3) and conservation of energy (Equation 2.4).

$$\frac{\partial \rho}{\partial t} + \nabla.(\rho \mathbf{u}) = \mathbf{0} \tag{2.1}$$

$$\frac{\partial \rho \mathbf{u}}{\partial t} + \nabla . \left[\rho \mathbf{u}\mathbf{u} + \mathbf{I} \left(\mathbf{p} + \frac{\mathbf{B^2}}{\mu_\mathbf{0}} \right) - \frac{\mathbf{B}\mathbf{B}}{\mu_\mathbf{0}} \right] = -\rho \mathbf{g} \tag{2.2}$$

$$\frac{\partial \mathbf{B}}{\partial t} + \nabla . (\mathbf{u}\mathbf{B} - \mathbf{B}\mathbf{u}) = \mathbf{0} \tag{2.3}$$

$$\frac{\partial}{\partial} \left(\frac{1}{2} \rho u^2 + \frac{3}{2} p \frac{B^2}{2\mu_0} \right) + \nabla . \left(\frac{1}{2} \rho u^2 \mathbf{u} + \frac{\mathbf{5}}{\mathbf{2}} \rho \mathbf{u} + \frac{(\mathbf{B}.\mathbf{B})\mathbf{u} - \mathbf{B}(\mathbf{B}.\mathbf{u})}{\mu_\mathbf{0}} \right) = \rho (\mathbf{g}.\mathbf{u}) \tag{2.4}$$

Here ρ is the mass density, u is the bulk velocity, p is the plasma pressure, $\mathbf{B}$ is the magnetic field vector, $\mathbf{g}$ is the gravity and μ_0 is the permeability of the free space. These equations are solved by the GM component of the SWMF.

2.2 Global Magnetosphere Model

The Block-Adaptive-Tree-Solarwind-Roe-Upwind-Scheme, (BATS-R-US) is used to model the global magnetosphere (GM) [*Toth et al.* (2005)]. It solves 3D MHD equations in a finite volume using Roe's Approximate Riemann Solver on a block adaptive mesh. BATS-R-US can take solar wind measurements of density, velocity, temperature and IMF components as inputs to simulate the global magnetosphere response to solar wind variations. The GM component can be coupled with the IM and IE models and pass the field aligned current information along these domains.

2.3 Inner Magnetosphere Model

2.3.1 Rice Convection Model: RCM

The Rice Convection Model (RCM) is a model of the inner and middle magnetosphere, including the ring current, plasma sheet and their coupling to the ionosphere [*Toffoletto et al.* (2003)]. The RCM uses a bounce-averaged kinetic model and assumes an isotropic distribution function to solve for the collisionless Vlasov equation for the particles in this region. The species included in the RCM are H^+, O^+ and electrons.

When coupled with a global magnetosphere model, RCM takes the time dependent magnetic and electric field input from an outer boundary of choice, which defaults to 10 Earth radii in the SWMF. Then the ExB and gradient curvature drifts are calculated for the transport of particles. The source term in the RCM is the inflow from the outer boundary, namely the global magnetosphere component, and the loss terms are outflow from the boundary and the charge exchange with neutral hydrogen.

The RCM can also be coupled with a high-latitude ionosphere model in the SWMF. In this case, the potential electric field is obtained through solving the current continuity equation and the currents close through the ionosphere through Field-Aligned Currents (FACs), giving rise to a more self-consistent estimate for the Region-2 current systems.

2.3.2 Comprehensive Ring Current Model: CRCM

The Comprehensive Ring Current Model (CRCM) is a kinetic model of the ring current and radiation belts. It solves the Boltzmann equation assuming an anisotropic pitch angle distribution for the particles. Building upon the RCM, CRCM also takes the time varying electric and magnetic fields to calculate the transport equations, in addition it accounts for losses along the particle drift paths [*Fok et al.* (2001)]. When coupled with a global magnetosphere, the CRCM generates the initial particle distribution in the ring current through the steady-state solution at the outer boundary.

2.4 Ionosphere Model

The Ridley Ionosphere Model (RIM), is a 2D ionospheric potential solver at 1000 km [*Ridley et al.* (2004)]. When coupled with global and inner magnetosphere models, it maps the Region-1 and Region-2 currents to the top of the ionosphere and generates a conductance pattern to calculate the electric field potentials. RIM also uses an

empirical relation for conductance that relates ground magnetic perturbations to Hall and Pedersen conductances [*Ridley et al.* (2004)]. Later an exponential empirical relationship is used to calculate the particle precipitation that creates the diffuse aurora in the model. The electric field potential and particle precipitation output from RIM can be used to drive the Global Ionosphere Thermosphere Model.

2.5 Ionosphere Thermosphere Model

2.5.1 The Model Description

The ionosphere and thermosphere are intrinsically coupled systems that require a self-consistent modeling approach. To provide a complete understanding of the geospace system response to solar wind pressure variations, ion and neutral behaviour should be examined through a first-principles based model. The Global Ionosphere Thermosphere Model (GITM) by *Ridley et al.* (2006) is a three dimensional global model, using an altitude-based non-uniform grid. It solves the dynamics and chemistry equations without the hydrostatic assumption.

The following neutral densities are included in GITM: $O, O_2, N(^2D), N(^2P), N(^4S)$, N_2, NO, H and He. The ion species included in the code are as follows: $O^+(^4S), O^+(^2D)$, $O^+(^2P), O_2^+, N^+, N_2^+, NO^+, H^+$ and He^+. The initial density profiles used in the simulations are from the International Reference Ionosphere (IRI) [*Bilitza* (2000)]. Each species has individual vertical velocities based on gradient in partial pressure, gravity, ion drag, Corriolis force, geometry and friction. The terms affecting the overall temperature are solar EUV, Joule and particle heating, conduction, NO and CO_2 radiative cooling.

The high-latitude drivers are particularly important when investigating the geospace system response to solar wind drivers. Solar wind-magnetosphere interactions significantly affect the high-latitude ionospheric electrodynamics and particle precipitation.

GITM can be coupled with various different high-latitude ionospheric electrodynamics models, including the output from the aforementioned ionosphere model, RIM, that self-consistently solves for the global and inner magnetospheres and projects them to a 2D ionosphere at 1000 km.

2.5.2 The Governing Equations

GITM solves the fluid equations for neutrals, ions and electrons in three-dimensional spherical coordinates. The fundamental equations for each of them are discussed below.

2.5.2.1 Neutral equations

The continuity equation for neutrals is shown in Equation 2.5.

$$\frac{\partial N_s}{\partial t} + N_s \bigtriangledown \cdot \mathbf{u} + \mathbf{u} \cdot N_s = 0 \tag{2.5}$$

Here u is the bulk neutral velocity in the horizontal direction and the N_s is the number density for species s. The momentum equation for the neutrals is shown in Equation 2.6.

$$\frac{\partial \mathbf{u}}{\partial t} + \mathbf{u} \cdot \bigtriangledown \mathbf{u} + \bigtriangledown \boldsymbol{T} + \frac{\boldsymbol{T}}{\rho} \bigtriangledown \rho = 0 \tag{2.6}$$

where, ρ denotes the total mass density of the neutrals and $\boldsymbol{T}$ is the normalized neutral pressure, i.e, p/ρ. Finally, the energy equation of neutrals is show in Equation 2.7

$$\frac{\partial \boldsymbol{T}}{\partial t} + \mathbf{u} \cdot \bigtriangledown \boldsymbol{T} + (\gamma - 1)\, \boldsymbol{T} \bigtriangledown \mathbf{u} = 0 \tag{2.7}$$

where γ is the specific heat ratio of the gas. The horizontal and vertical advection is treated separately in GITM. The derivation of the conservation equations for the

horizontal and vertical components in spherical coordinates are described in detail in *Zhu et al.* (2016), *Ridley et al.* (2006), *Zhu* (2016). The continuity equation in the vertical direction after these derivations becomes:

$$\frac{\partial N_s}{\partial t} + N_s \left(\frac{1}{r}\frac{\partial u_\theta}{\partial \theta} + \frac{1}{rcos\theta}\frac{\partial u_\phi}{\partial \phi} - \frac{u_\theta tan\theta}{r} \right) + \frac{u_\theta}{r}\frac{\partial N_s}{\partial \theta} + \frac{u_\theta}{rcos\theta}\frac{\partial N_s}{\partial \phi} = 0 \tag{2.8}$$

The eastward component of the momentum equation is as follows:

$$\begin{aligned} \frac{\partial u_\theta}{\partial t} + u_r\frac{\partial u_\theta}{\partial r} + \frac{u_\theta}{r}\frac{\partial u_\theta}{\partial \theta} + \frac{u_\theta}{rcos\theta}\frac{u_\theta}{\partial \phi} + \frac{1}{rcos\theta}\frac{\partial \mathbf{T}}{\partial \theta} + \frac{\mathbf{T}}{r\rho cos\theta}\frac{\partial \rho}{\partial \phi} \\ = \frac{\mathbf{F}_\phi}{\rho} + \frac{u_\theta u_\phi tan\theta}{r} - \frac{u_r u_\theta}{r} + 2\Omega u_\theta sin\theta - 2\Omega u_r cos\theta \end{aligned} \tag{2.9}$$

Here F_ϕ is the force due to ion-neutral friction and neutral viscosity in the Φ direction. This term can be expressed as follows:

$$\mathbf{F}_\phi = \rho_\mathbf{i}\mu_\mathbf{in}(\mathbf{v}_\theta - \mathbf{u}_\theta) + \frac{\partial}{\partial \mathbf{r}}\eta\frac{\partial \mathbf{u}_\theta}{\partial \mathbf{r}} \tag{2.10}$$

where μ_{in} is the ion-neutral collision frequency and η is the viscosity coefficient. The northward component of the momentum equation is given below:

$$\begin{aligned} \frac{\partial u_\theta}{\partial t} + u_r\frac{\partial u_\theta}{\partial r} + \frac{u_\theta}{r}\frac{\partial u_\theta}{\partial \theta} + \frac{u_\phi}{rcos\theta}\frac{\partial u_\theta}{\partial \phi} + \frac{1}{r}\frac{\partial \mathbf{T}}{\partial \theta} + \frac{\mathbf{T}}{r\rho}\frac{\partial \rho}{\partial \theta} \\ = \frac{\mathbf{F}_\theta}{\rho} - \frac{u_\phi^2 tan\theta}{r} - \frac{u_\theta u_\phi}{r} - \Omega^2 rcos\theta sin\theta - 2\Omega u_\phi sin\theta \end{aligned} \tag{2.11}$$

Here the Ω is the Earth's angular velocity, i.e., effect of the Coriolis force and F_θ is the ion-neutral friction and neutral viscosity in the θ direction as shown in Equation 2.12.

$$\mathbf{F}_\theta = \rho_\mathbf{i}\mu_\mathbf{in}(\mathbf{v}_\theta - \mathbf{u}_\theta) + \frac{\partial}{\partial \mathbf{r}}\eta\frac{\partial \mathbf{u}_\theta}{\partial \mathbf{r}} \tag{2.12}$$

Finally, the horizontal energy equation for the neutrals is:

$$\frac{\mathbf{T}}{\partial r} + \frac{u_\phi}{rcos\theta}\frac{\partial \mathbf{T}}{\partial \theta} + (\gamma - 1)\mathbf{T}\left(\frac{\mathbf{1}}{\mathbf{r}}\frac{\partial \mathbf{u}_\theta}{\partial \theta} + \frac{\mathbf{1}}{\mathbf{rcos\theta}}\frac{\partial \mathbf{u}_\phi}{\partial \phi} - \frac{\mathbf{u}_\theta \mathbf{tan\theta}}{\mathbf{r}}\right) = \mathbf{0} \tag{2.13}$$

and the vertical energy equation for the neutrals is:

$$\frac{\partial \mathbf{T}}{\partial t} + u_r\frac{\partial \mathbf{T}}{\partial r} + (\gamma - 1)\mathbf{T}\left(\frac{\mathbf{2u_r}}{\mathbf{r}} + \frac{\partial \mathbf{u_r}}{\partial \mathbf{r}}\right) = \frac{\kappa}{\mathbf{c}_\nu \rho \overline{\mathbf{m_n}}}\varepsilon \tag{2.14}$$

where c_ν is the averaged specific heat, κ is the Boltzmann constant, the $\overline{m_n}$ is the average mass of neutrals, ε is the energy term that contains the solar EUV heating, NO and O cooling, thermal conduction and Joule heating rates.

2.5.2.2 Ion equations

The ion equations are also separated into the horizontal and vertical components. The ion continuity equation in the horizontal direction is as follows:

$$\frac{\partial N_j}{\partial t} + \frac{v_\theta}{r}\frac{\partial N_j}{\partial \theta} + \frac{v_\phi}{rcos\theta}\frac{\partial N_j}{\partial \phi} = L_j \tag{2.15}$$

Here, N is the number density of the ion species j and L_j is the source term. The ion continuity equation in the vertical direction is as follows:

$$\frac{\partial \mathbf{N_j}}{\partial t} + v_r\frac{\partial \mathbf{N_j}}{\partial r} + \mathbf{N_j}\frac{\partial \mathbf{v_r}}{\partial \mathbf{r}} = \mathbf{0} \tag{2.16}$$

Here, N is the natural log of the number density of the ion species j. This equation is solved for O^+ only, since it is the most dominant species at the F-region. The ion momentum equation is shown in Equation 2.17.

$$\rho_i\frac{d\mathbf{v}}{dt} = -\bigtriangledown(p_i + p_e) + \rho_i\mathbf{g} + \mathbf{eN_e}(\mathbf{E} + \mathbf{v} \times \mathbf{B}) - \rho_\mathbf{i}\mu_\mathbf{in}(\mathbf{v} - \mathbf{u}) \tag{2.17}$$

where $\mathbf{g}$ is the gravity term. This equation can be further simplified by neglecting

the temporal variation of the ion velocity on the left hand side. Finally, the ion energy equation is shown in Equation 2.18.

$$\frac{3}{2}\kappa n_i \frac{\partial T_i}{\partial t} = -\kappa n_i T_i \bigtriangledown \cdot \mathbf{u_i} - \frac{\mathbf{3}}{\mathbf{2}}\mathbf{N_i}\kappa \mathbf{u_i} \cdot \bigtriangledown \mathbf{T_i} - \bigtriangledown \cdot \mathbf{q_i} + \mathbf{\Sigma Q_i} \tag{2.18}$$

Here q_i is the ion heat flow and Q_i is the sum of ion heating rates. In addition, two specific heating terms for the ions are shown in Equations 2.19 and 2.20. The term that expresses the collisional heating of ions by the electrons is shown below.

$$Q_{ie} = 3\kappa\Sigma_i \frac{n_t m_t \nu_t e}{m_t + m_e}(T_e - T_i) \tag{2.19}$$

The heating term that defines the collisional heating of ions by neutrals is as follows.

$$Q_{in} = \Sigma_t n_t m_t \Sigma_k \frac{3\kappa(T_n - T_i) + m_k(u_n - u_i)^2}{m_t + m_k} \tag{2.20}$$

2.5.2.3 Electron equations

The calculations for electrons are simpler since the electron density is calculated from the sum of the ion densities due to charge neutrality. Furthermore, the electron motion is mainly controlled by the $\mathbf{E} \times \mathbf{B}$, further simplifying the terms in the electron momentum equation. The resulting expression for electron velocity is shown in Equation 2.21.

$$\mathbf{v_e} = \frac{\mathbf{E} \times \mathbf{B}}{\mathbf{B^2}} \tag{2.21}$$

The electron energy equation is shown in Equation 2.22.

$$\frac{\partial T_e}{\partial t} = \frac{2}{3} T_e \bigtriangledown \cdot \mathbf{v_e} - \mathbf{v_e} \cdot \bigtriangledown \mathbf{T_e} + \frac{\mathbf{2}}{\mathbf{3}} \frac{\mathbf{1}}{\mathbf{N_e}\kappa} (- \bigtriangledown \cdot \mathbf{q_e} + \mathbf{Q_e} + \mathbf{L_e}) \tag{2.22}$$

Here Q_e is the total electron heating rate, L_e is the total electron cooling rate, and q_e is the electron heat flow vector, which is shown in Equation .

$$\mathbf{q_e} = -\beta_\mathbf{e}\mathbf{J}_\parallel - \kappa_\mathbf{e} \bigtriangledown \mathbf{T_e} \tag{2.23}$$

The electron heat flow vector depends on β_e the thermoelectric coefficients, $J_\parallel$ the current parallel to the magnetic field and κ_e the electron thermal conductivity. In addition, the collisional heating of electron by ions is described as below.

$$Q_{ei} = 3\kappa n_e m_e \Sigma_t \nu_{et} \frac{(T_i - T_e)}{m_e + m_t} \tag{2.24}$$

2.6 Other Tools Used in the Study

2.6.1 Ground Observations

2.6.1.1 SuperMAG

SuperMAG is an international collaboration effort, which collects and provides a database for more than 300 ground based magnetometers [*Gjerloev* (2012)]. It utilizes 3D vector measurements of the magnetic field perturbations measured on the ground. The magnetic field contributions from the Earth's slowly varying dipole field is subtracted (baseline removal) from the measurements.

2.6.1.2 PFISR

Poker Flat Incoherent Scatter Radar is the first component of the Advanced Modular Incoherent Scatter Radar (AMISR) which is a radar facility designed to conduct studies of the upper atmosphere, ionosphere and space weather events. PFISR is located at the $65°N$ and $147°W$. The radar measures plasma parameters such as electron density, electron temperature, ion density, ion temperature, ion neutral collision frequency, ion velocity and composition. The AMISR project is led by Southwest

Research Institute.

2.6.2 Spacecraft Observations

2.6.2.1 THEMIS

The Time History of Events and Mesoscale Interactions During Substorms (THEMIS) mission, employs 5 identically instrumented spacecraft with a primary objective of understanding the cause of geomagnetic substorms. The instrument on board THEMIS spacecraft are: Electric Field instrument (EFI), Fluxgate magnetometer (FGM), Search Coil magnetometer (SCM), Electrostatic analyzer (ESA), Solid State telescope (SST). In this study Themis-D, ESA measurements have been used, which are presented in Chapter 5. For this I would like to acknowledge NASA contract NAS5-02099 and V. Angelopoulos for use of data from the THEMIS Mission. Specifically, C.W. Carlson and J. P. McFadden for use of ESA data.

2.6.2.2 MMS

The NASA Magnetospheric Multi-scale Mission (MMS), consist of four identically instrumented spacecraft that is utilized to study the magnetic reconnection. The FIELDS: Magnetic and Electric Field Instrument Suite is used in this study. Therefore I would like to acknowledge Dr. Roy Torbert the lead Co-I of the FIELDS instrument suite, and Dr. C. T. Russell, the PI of the FGM instrument.

2.6.3 SpacePy

SpacePy is a Python package for space sciences, which aims to make data analysis, modeling and visualization easier [*Morley et al.* (2011)]. This open-source code library was extensively used and its functionality was further improved to visualize and process the simulation results presented throughout this study.

CHAPTER III

The Response of the Geospace System to Solar Wind Dynamic Pressure Enhancements Under Different IMF B_Y orientations

3.1 Introduction

The Earth's magnetosphere undergoes a rapid compression when the solar wind dynamic pressure exhibits a sudden increase. Such enhancements generally occur during encounters with earthward directed IP shocks or steepened high speed stream interfaces. The compression propagates along the magnetosphere-ionosphere (M-I) system [*Collier et al.* (1998), *Suguira et al.* (1968) , *Huttunen et al.* (2005)], which can be traced through ground magnetometers simultaneously [*Araki* (1994b)]. However understanding the formation and propagation of sources behind the SI signal believed to need further study [*Tanaka* (2003)].

As discussed before, the magnetic perturbations measured on the ground are a result of enhanced and reconfigured M-I current systems during the compression of the magnetosphere. At lower latitudes, Chapman-Ferraro currents are the primary source [*Kikuchi and Araki* (1979)], whereas the field-aligned current (FACs) systems and their closure currents play the dominant role at higher latitudes. Global simulations by *Fujita et al.* (2003b), *Fujita et al.* (2005), *Yu. and Ridley* (2011), and *Kubota et al.*

(2015) all displayed different ionospheric transient current systems which form on the dayside and then propagate toward the nightside during the compression events. Simulation results from *Fujita et al.* (2003a) showed an initial current system forming as a result of the immediate magnetopause deformation, in association with the PI signature. Later simulations by *Fujita et al.* (2003b) identified the magnetospheric plasma vortices as the source of the MI signature. Their results showed both these current systems were not a part of the preexisting Region-1 (R1) and Region-2 (r2) current systems on the top of the ionosphere.

Using ground magnetometer results *Araki* (1994b) derived a model of SIs, showing that the PI signal was caused by the equivalent current systems as a result of dusk-to-dawn electric fields. On the contrary the MI signal was due to the equivalent current system resulting from dawn-to-dusk electric fields. In addition, theoretical studies of *Kivelson and Southwood* (1991) revealed that as the magnetopause boundary was compressed, vortices were generated at the boundary, which then propagated with the compression front. Likewise these vortices launched Alfven waves, which propagated down to the ionosphere and perturb the Region 1 and 2 current systems. Similar perturbations of the current systems were also reported by *Yu and Ridley* (2009) using BATS-R-US global MHD simulations. They have shown that regardless of the magnetic latitude, the response to a sudden dynamic pressure enhancement consisted of two phases. However, the identification of the first phase was difficult in the equatorial regions due to fast magnetosonic waves being frequently reflected from the inner and outer boundary of the magnetosphere, eventually dissipating.

A self-consistent model of the M-I system imposes closure of the FAC system through the magnetosphere and ionosphere as boundary conditions. This model results in equivalent convection flows in both the magnetosphere and ionosphere *Tanaka* (2003). Such observations of ionospheric vortices were reported in *Murr et al.* (2002) by combining observations from ground-based magnetometers from Northern and

Southern hemispheres, riometers, and auroral imagers to study the relation between FACs and traveling convection vortices (TCVs). TCVs are a pair of ionospheric counterclockwise or clockwise convection flow vortices that form on the dayside and propagate toward the nightside [*Murr et al.* (2002), *Zesta et al.* (1999)]. Such vortex counterparts were also seen in global MHD simulations. *Slinker et al.* (1996) were one of the first to show that the TCVs form during pressure pulses. By tracing the magnetic field lines that connect the two regions, they showed that the ionospheric TCVs mapped to regions in the equatorial magnetosphere where vortical flows formed and they were associated with such transient currents. *Yu. and Ridley* (2011) also showed the formation and propagation of magnetospheric vortices and their association with the second FAC response that created the MI part of the SC.

The transient currents also change the conductivity profile at the top of the ionosphere. *Zhu et al.* (1999) further studied the effects of precipitation from magnetospheric vortices to the ionosphere along the FACs and concluded that FACs associated with TCVs can cause localized conductivity variations. Furthermore, they showed that this enhancement of conductivity leads to distortion of TCVs and lead to the ground magnetic perturbations.

As discussed in Section 1.2.2.1, the IMF holds a key role in understanding the variability observed in the PI-MI signatures. *Iijima and Potemra* (1976) has shown that the FAC patterns were altered significantly with varying IMF B_Y and B_Z. The IRIDIUM measurements reported in *Anderson et al.* (2008) provided a 10 year statistical distribution of the Region-1 currents derived under different IMF conditions. These results have shown that when the IMF B_Y orientation was positive, the downward FAC cell on the dawn sector expanded and extended equatorward, while in the case of negative IMF B_Y, the upward FAC cell on the dusk sector showed the same response. This effect was more prevalent during northward IMF B_Z conditions.

The dependence of the ionospheric convection to the IMF B_Y orientation has

been well established with numerous studies that include theory, satellite measurements, and ground-based radar observations of ion velocity data [*Backus* (1986); *Heelis* (1984); *Heppner and Maynard* (1987); *Amm et al.* (1999); *Weimer* (2005); *Wilder et al.* (2013)]. Global simulations by *Tanaka* (2001) showed that the mirror symmetry of the two-cell convection pattern was broken due to IMF B_Y. They also identified the Hall currents induced by the Region-1 FAC systems was responsible for the flow variations on the dayside. Yet the relation between IMF B_Y and asymmetries in the ground magnetometer responses was not as widely studied. A study by *Sitar and Friis-Christensen* (1996) concluded that there was no systematic response to solar wind dynamic pressure enhancements and no evident link between the magnetometer response and IMF clock angle, using 2500 h of solar wind data from IMP 8 and ground magnetometers. However, not focusing on the effects of IMF B_Y during northward and southward IMF B_Z conditions separately might have affected the results. Another study to relate the IMF properties with ground magnetic perturbations was conducted by *Weimer* (2005), using the empirical model for convection patterns. The study showed that the empirical model had lower skill scores at sites close to perturbation reversals. This underlines the need for studying the IMF B_Y related asymmetries in perturbation signatures with first-principles based models, which can reproduce magnetospheric and ionospheric sources self-consistently.

3.2 Simulation Setup

To model the solar wind dynamic pressure interaction with the coupled M-I system, we used the SWMF [*Toth et al.* (2005)]. The GM/BATS-R-US, IM/CRCM and IE/RIM components were used to represent the system. The set of simulations presented in this chapter were run on Yellowstone supercomputer cluster operated by the National Center for Atmospheric Research (NCAR).

Three cases were simulated through the aforementioned combination to investigate

the effects of IMF B_Y i.e., B_Y = -5 nT, $B_Y = 0$, and $B_Y = 5$ nT, while all the other parameters were kept the same. The idealized solar wind plasma and IMF parameters that were used to drive the system are shown in Figure 3.1a. The sudden dynamic pressure enhancement was introduced at the outer boundary at t-7 min. The V_X increased from 350 km/s to 445 km/s. The proton number density increased from 10 amu/ cm^3 to 30 amu/ cm^3 and the overall dynamic pressure was enhanced 4 times to its initial value. These values were adapted from a case study of the solar wind dynamic pressure enhancement event on 15 August 2015. The solar wind and IMF conditions extracted from 14 R_E upstream revealed how the shock propagated from the outer boundary to the Earth. When the compression front arrived at the subsolar point, the value of V_X was 430 km/s, the density was 26 amu/ cm^3 and the B_Z and B_Y values deviated only slightly from their initial values.

In order to determine the ground magnetometer response to pressure change, 100 virtual ground magnetometers were implemented uniformly in between 50° and 80° magnetic latitude and with 36° magnetic longitude resolution. A Biot-Savart integral-based algorithm in SWMF readily calculates the perturbations caused by the M-I currents [*Yu and Ridley* (2008)]. The locations of the ground magnetometers are shown in Figure 3.1b. A baseline value is determined (the values at t-1 min.), and subtracted from the reported ground magnetometer responses.

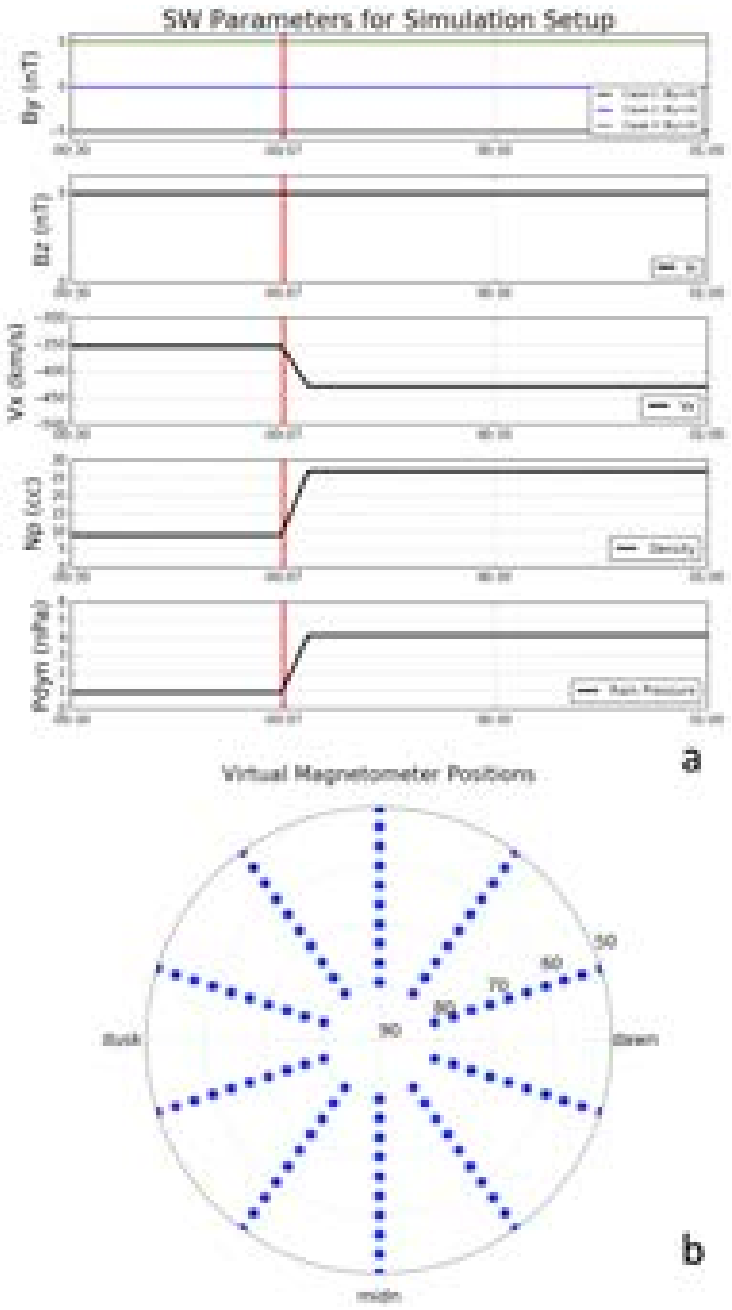

Figure 3.1: (a) The idealized solar wind parameters for three simulations. The first panel shows the IMF B_Y for case 1 ($B_Y = -5nT$), case 2 ($B_Y = 0nT$) and case 3 ($B_Y = 5nT$). The second panel shows IMF $B_Z = 5nT$, the third panel shows the velocity, the fourth panel shows the density and the fifth panel shows the variation in the solar wind dynamic pressure. The red line marks the time of the pressure in the outer boundary. (b) The positions of the virtual magnetometers in MLT coordinates.

3.3 Response of the M-I System

3.3.1 Ground Magnetometer Response to Different IMF B_Y

3.3.1.1 Middle latitude Response

The magnetic north (N) component of the simulated magnetic field perturbations at the ground was investigated to understand the response at the 50° and 60° magnetic latitudes. The MLT-time maps of simulated responses are shown in Figure 3.2a. The first row shows the temporal evolution at 50° under three different IMF B_Y orientations, however there was no significant difference between the three cases. A bipolar response to SI was recorded in all three cases, with a negative dip around 4 nT, followed by a positive perturbation around 10 nT between 11 MLT to 3 MLT. The response was a step-wise enhancement at the dawn sector. The peaks of the bipolar signature were recorded at around t+3 min. and t+7 min., which marked the PI and MI phases respectively.

The SI response at 60°, (bottom row of Figure 3.2a) was very similar to the response at the 50° magnetic latitude, with slightly higher amplitudes recorded for PI and MI phases. The response started to show minor asymmetries around dawn sector, compared with the post-noon responses.

3.3.1.2 High latitude Response

The MLT-time maps of the simulated N-component at 70° and 80° under three different IMF B_Y orientations are shown in Figure 3.2b. The first row shows the temporal evolution at 70°. It can be seen that very clear bipolar signatures have formed as a response to SI at the 70° magnetic latitude. There were also significant dawn-dusk asymmetries between the three different cases. Between 18 and 21 MLTs, simulations driven with negative (left) and positive (right) B_Y, showed a positive perturbation followed by a negative perturbation in the N component. However, the

simulations driven with zero B_Y had a negative perturbation at this region followed by a positive response. In addition, between 0 and 6 MLTs, the simulated response to the SI under a negative B_Y (left) had a negative - positive - negative trend, whereas the positive and zero B_Y responses only recorded a negative then positive trend. In all three cases, the peaks of the bipolar signature were recorded around t+3 min. and t+7 min., similar to the middle latitudes, at the post-noon sectors. Yet, the pre-noon sectors recorded these peaks about 2 minutes earlier.

The bottom three panels in Figure 3.2b show the perturbation maps for stations at 80° magnetic latitude. At this latitude the asymmetries between different cases became very apparent. The simulations driven with negative B_Y (left) showed a strong negative perturbation as a response to SI. Between 10 to 00 MLTs, the response had a weak positive followed by a stronger negative trend. On the contrary, between 00 to 06 MLTs, the response was a strong negative followed by a weak positive trend. The simulations driven with zero B_Y (middle) showed overall weaker perturbations compared to positive and negative B_Y cases, with asymmetric post-noon and pre-noon responses in accordance with *Araki* (1994b) model. The SI perturbations during the positive B_Y (right) showed an overall stronger positive response. There were no significant asymmetries between post-noon and pre-noon sectors, however the response was stronger at the dawn sector. Similarly, the peaks of perturbations corresponded to previous timings of PI and MI peaks.

3.3.2 Field-aligned Current Systems Under Different IMF B_Y

The temporal evolution of the FAC systems as a response to solar wind dynamic pressure enhancement under different IMF B_Y orientations are presented in Figure 3.3a. These polar plots show the Northern hemisphere down to 50° magnetic latitude with magnetic noon located on top. The red contours show the upward FACs, whereas the blue contours show the downward FACs. The solid and dashed lines show the

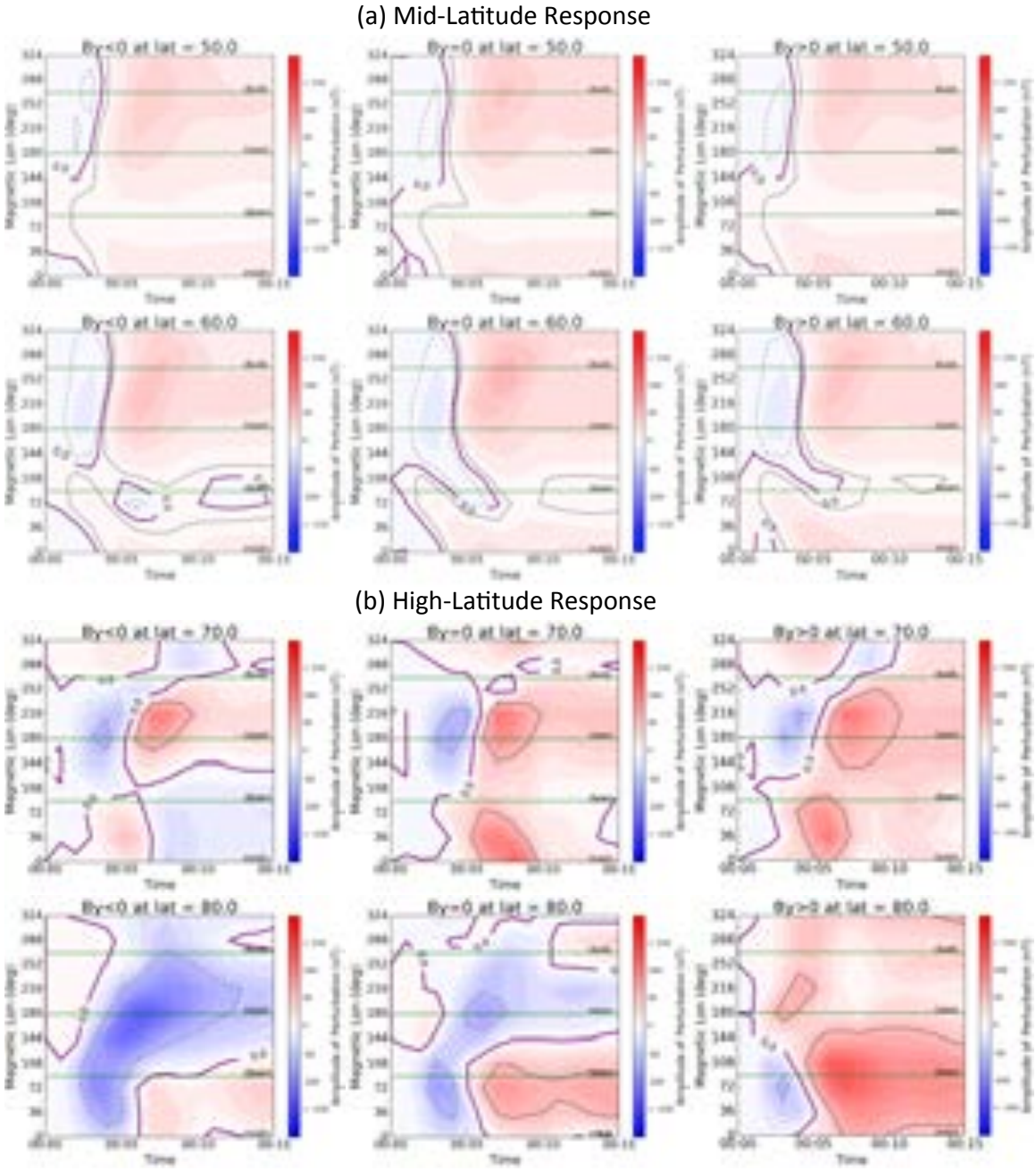

Figure 3.2: The MLT-time maps of the magnetic perturbations detected by the uniformly distributed virtual ground magnetometers located at middle latitudes (a) and high latitudes (b) are shown. The rows show $50°, 60°, 70°$ and $80°$ latitudes (top to bottom). The panels on the left show the responses when IMF B_Y is negative, the ones in the center show the case when B_Y is 0, and the panels on the right show the response when B_Y is positive. The red contours show positive, blue contours show negative perturbations. The purple line is the zero contour. Green lines show the dusk, noon, dawn, midnight sectors.

electric field potentials, while the solid purple line is the open closed field boundary output from the simulations. The top row shows the FACs at the time of arrival of the compression front to the Earth's magnetopause, t. These initial FAC profiles are very different due to the orientation of B_Y. Each column in Figure 3.3a shows the response under a different B_Y orientation, that is negative, zero and positive from left to right. Each row in Figure 3.3a shows a different time interval with 1 min. cadence starting from t (top) to t+3 min. (bottom).

The FACs under negative IMF B_Y had a larger downward FAC cell at the high latitude region, whereas the the FACs under positive B_Y had a larger upward FAC cell at the same region. The FACs under zero B_Y showed the nominal NBZ current system in which both downward and upward FACs had the same cell size at higher latitudes. As the compression front reached the Earth, all three FAC profiles showed a pair of an additional upward FAC cell on dawn and a downward FAC cell on dusk sectors, around 70° magnetic latitude. This FAC pair was later seen as propagated towards the midnight sector at t+2, mapping to a slightly higher magnetic latitude around 75°. At the same time instance, t+2, another additional FAC pair with opposite polarities to the initial pair had formed in the dayside at all simulated cases. The new FAC pair had an upward cell on dusk and a downward cell on dawn again around 70° magnetic latitude. At t+3, this second FAC pair can be seen as it propagated to the nightside following the first FAC pair. The upward FAC of the second pair was stronger (0.1 - 0.2 $\mu A/m^2$) during the negative B_Y case, and the downward FAC was stronger during the positive B_Y case.

In order to investigate these transient FACs, the pre-compression FAC profiles were subtracted from each time snapshot. The evolution of these perturbation FACs are shown in Figure 3.3b. The FACs related with PI had the same direction in all three cases, which was upward at the pre-noon and downward at the post-noon sectors. The strength of the perturbation currents did not vary in between the three

cases however the downward cell extended towards noon during the negative B_Y, whereas upward cell extended towards noon during positive B_Y as can be inferred from the t+1 snapshots. The second perturbation FAC pair had an opposite polarity to that of the first one. This current pairs occur at t+2, displaying more asymmetric features compared to the previous pair. In this case, the downward cell extended towards noon during the positive B_Y, whereas the upward cell extended towards noon during negative B_Y. These perturbation FACs with different polarities resulted in the previously reported variations in the simulated ground magnetometer signatures. Therefore the initial perturbation FAC pair will be referred to as PI-FACs, whereas the second perturbation FAC pair will be referred to as MI-FACs from here forward.

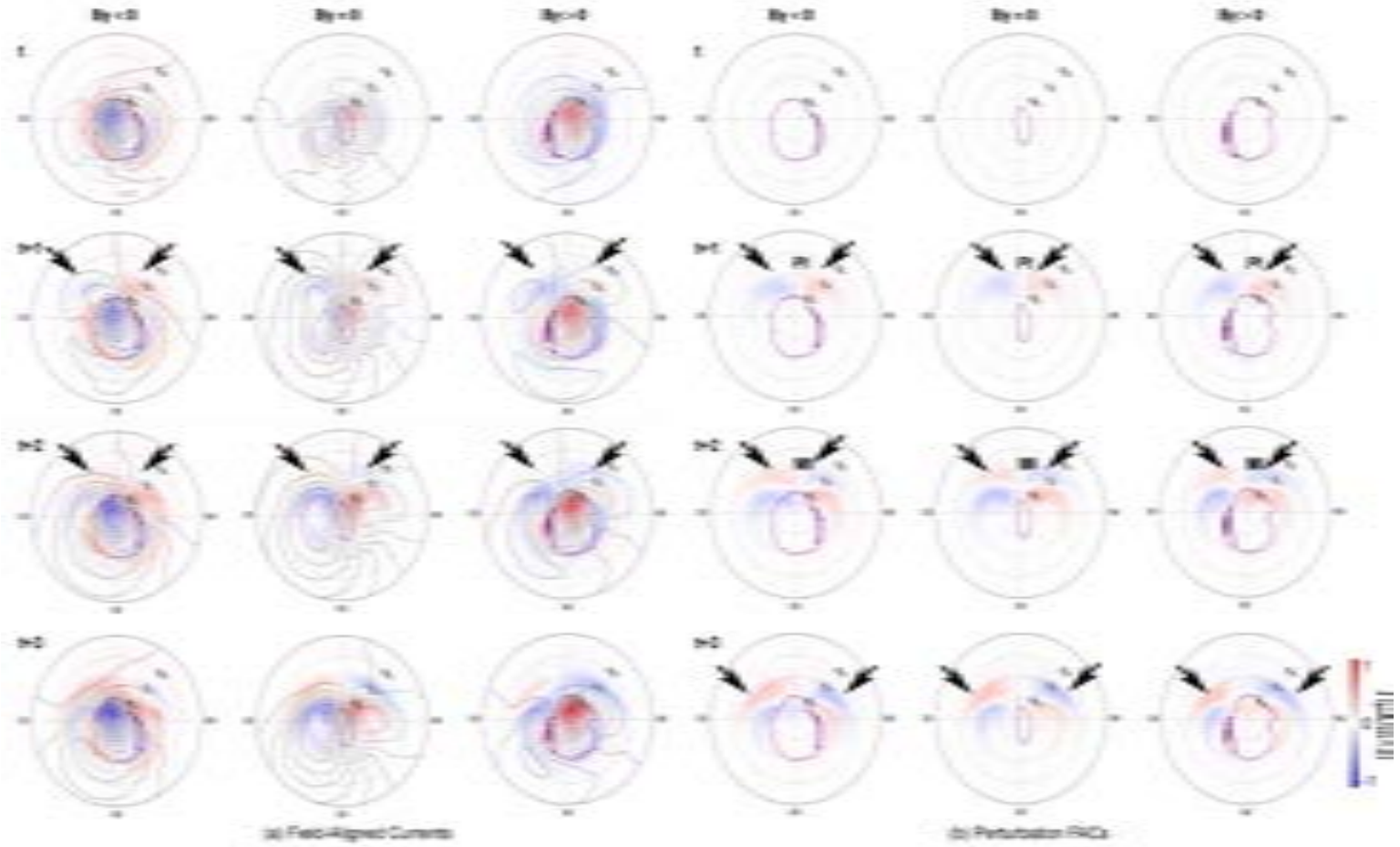

Figure 3.3: (a) The temporal evolution of the FACs in the Northern hemisphere between t and t+3 minutes under different IMF B_Y conditions. From left to right, the first column shows the case for negative B_Y, the second column shows the case for zero B_Y and the third column shows the case for positive B_Y. (b) The temporal evolution of the time differenced FACs are shown for the same time instances. The perturbation FACs that give rise to PI and MI signatures on the ground are labeled.

3.3.3 Contributions from Different Currents Systems to the Magnetic Perturbations at the Ground

In order to understand the sources of the simulated ground magnetic perturbation responses, the contributions from different magnetospheric and ionospheric currents have to be taken into account. In this section the magnetic perturbations caused by FACs, Pedersen, Hall, and magnetospheric currents are discussed. The response of the zero B_Y case is provided as an example.

Figure 3.4 shows the polar plots of perturbation in the north component of the simulated magnetic field computed from FACs, Pedersen currents, Hall currents, magnetospheric currents and the total perturbation (from left to right) at three time instances which are before the event (t-1), during the PI peak (t+3) and during the MI peak (t+7). The subtraction of the baseline value resulted in zero before the compression as can be seen from Figure 3.4a to Figure 3.4e (first row).

During the PI phase (second row), the perturbations from the FAC and Pedersen currents roughly cancelled each other. The perturbation profile due to the Hall current was negative on the dayside, with a negative dip on the high-latitude noon sector, and a positive peak around 5 MLT. The response in the low latitude sectors in between 0 to 6 MLT were positive. The high latitude response to Hall currents between 15-0 MLT was also positive. The contribution from the magnetospheric currents was a weak positive except the high latitude dawn to noon sectors. The overall perturbation profile resembled the Hall perturbation profile with slight variations at the low latitude sectors.

During the MI phase (bottom row), the polarity of the FAC and Pedersen currents were reversed. Between 2-15 MLT the magnetic perturbation response to FACs was negative, whereas it was positive everywhere else. Similarly, between 2-18 MLT the magnetic perturbation response was positive to the Pedersen currents, however at the nightside the high-latitude response was negative. The magnetic perturbation

response to Hall currents at this time was asymmetric. The high latitude response between 8-22 MLT (clockwise) was negative, while elsewhere the response was positive. At lower latitudes, the responses had opposite signs. The MI responses were stronger than the PI responses to the Hall currents. The response to magnetospheric currents remained similar to that of the PI phase. The total perturbation profile again resembled the Hall perturbation profile, with enhanced response at the pre-midnight sector due to the contributions from the FAC perturbations.

Figure 3.5 shows the total magnetic perturbation profiles taken at the PI (top) and MI (bottom) peaks for the three cases. During the PI phase (top row), the response to negative B_Y was a negative perturbation at the high latitudes extending from the midnight region towards the noon. This response was similar in zero B_Y but the amplitude was weaker. However the negative response in positive B_Y was confined to the 0-2 MLT and 8-15 MLT regions, with a patch of positive perturbation around 2-8 MLT. The amplitude of the negative response was also weaker compared to zero and negative B_Y cases, whereas the positive response had stronger amplitude.

During the MI phase (bottom row), the simulated response to positive B_Y was the strongest with a peak amplitude around 160 nT. In comparison, the response to negative B_Y had a peak at the high latitude noon sector that was around 100 nT. There was a magnetic local time asymmetry observed in the response of the negative B_Y case.

3.3.4 Magnetospheric Sources for the Perturbations at the Ground

Simulated magnetometer responses showed significant asymmetries during the compression event due to variations of the perturbed FACs and ionospheric currents. To examine the source of the perturbed FACs, we trace the magnetic field lines that link the disturbance currents at the ionosphere to the equatorial magnetosphere. The red solid lines indicate an upward FACs associated field line, whereas the blue solid

lines show a downward FAC associated field line. The arrows show the velocity vectors in the equatorial plane with different colors representing their flow speed.

3.3.4.1 PI Response

Figure 3.6 shows two time instances taken at t and t+1 for three different B_Y cases. At time t, the FAC configuration of each case was different but as can be seen more clearly from the snapshots at t+1, the compression led to an upward FAC on dawn and a downward FAC on dusk in all three cases. This current was generated as a result of magnetopause deformation and reconfiguration of the magnetospheric return flows to form a counter clockwise rotating vortex on dawn, and a clockwise rotating vortex on dusk sectors.

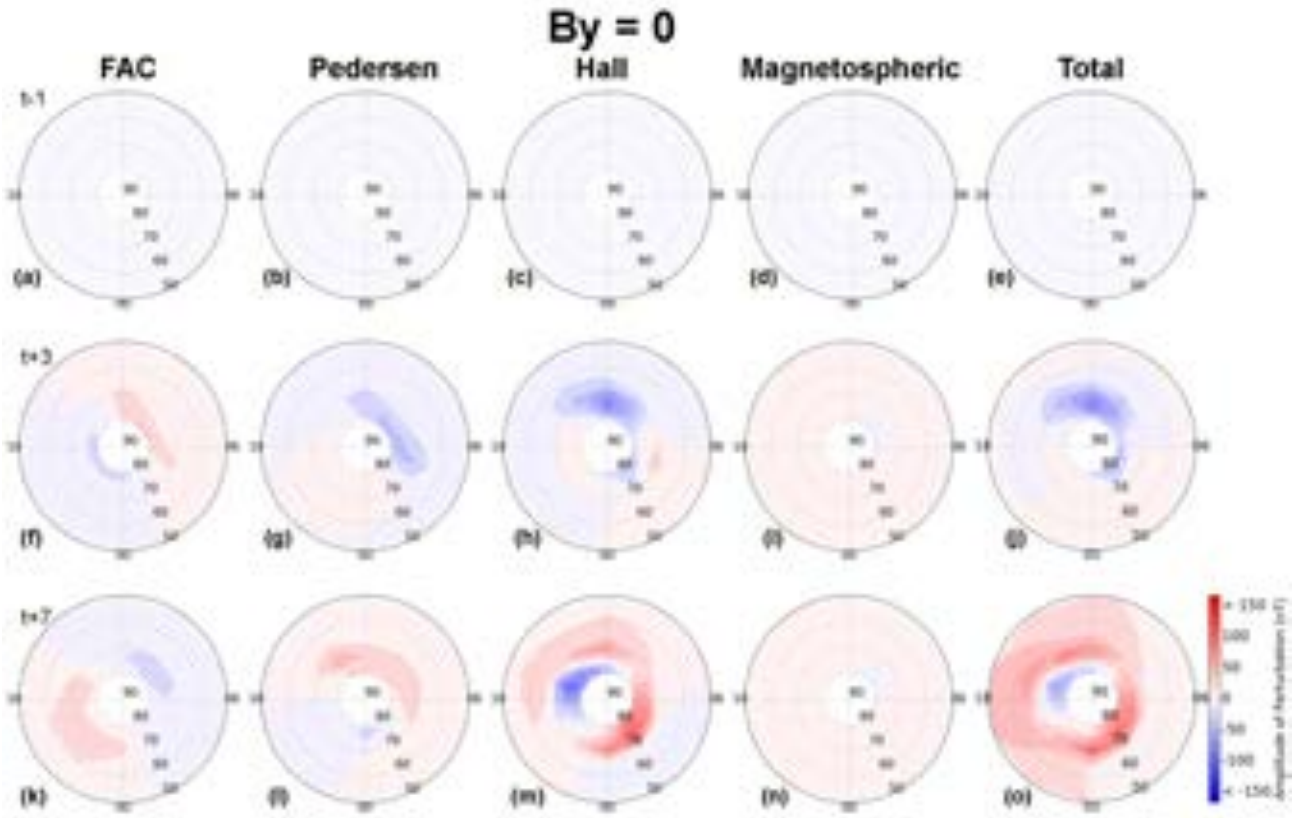

Figure 3.4: The contour plots showing contribution from different current systems in the M-I system for the case where B_Y is zero at three time instances t-1, t+3, and t+7 minutes. From left to right each column shows FAC, Pedersen, Hall, Magnetospheric currents and the total perturbation respectively.

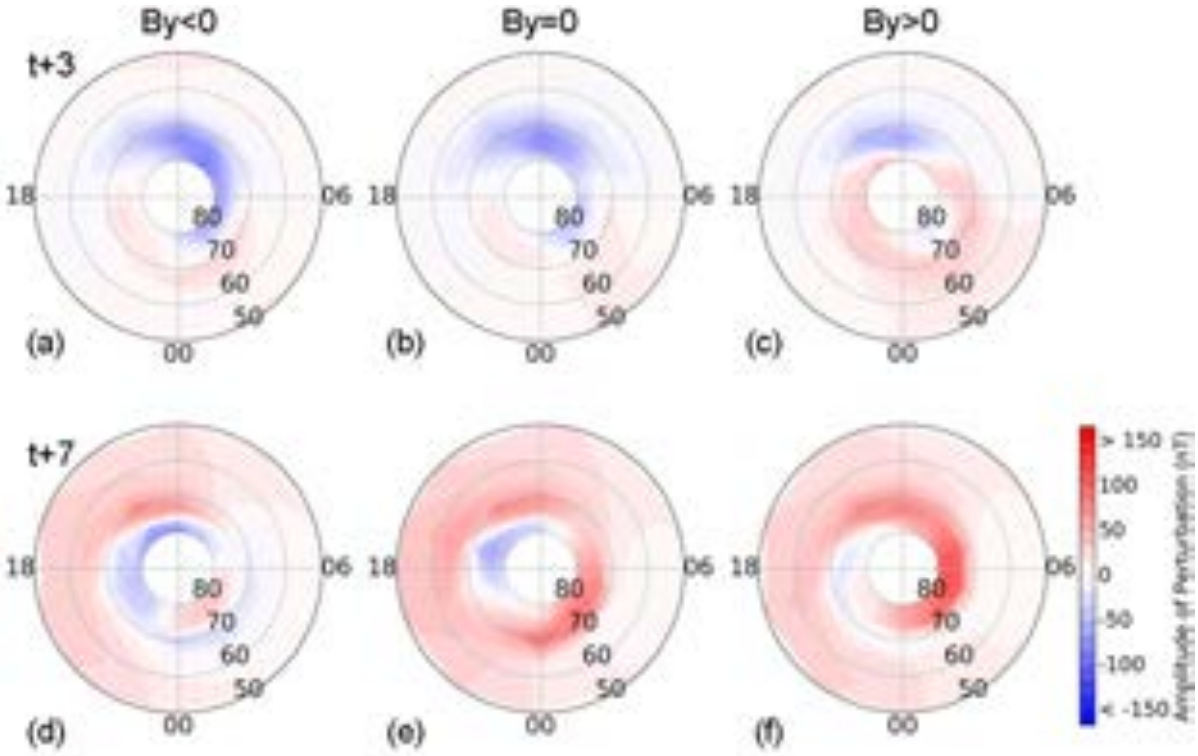

Figure 3.5: The ground magnetic perturbation profiles taken at peak PI (t+3 min.) and MI (t+7 min.) are shown for the northern hemisphere. From left to right the columns show negative B_Y, zero B_Y, and positive B_Y cases.

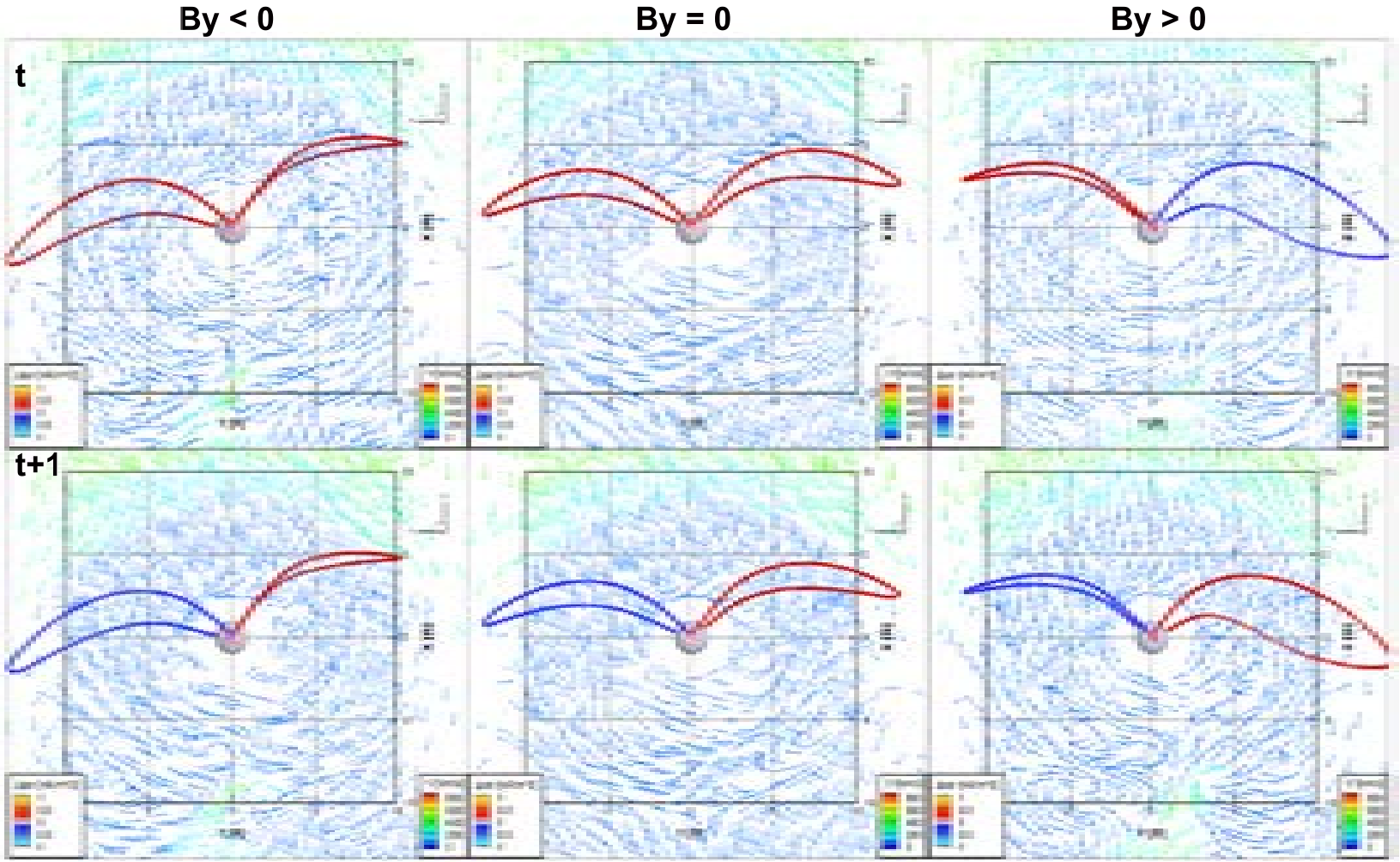

Figure 3.6: The equatorial magnetospheric flow profiles taken before the compression at t (top row), and 1 minute after the compression (bottom row) are shown. The arrows show the velocity vector, whereas solid lines show the magnetic field lines, colored based on the direction of the field-aligned current on the ionospheric foot point (red/blue-upward/downward). From left to right the columns show negative B_Y, zero B_Y, and positive B_Y cases.

3.3.4.2 MI Response

Figure 3.7 shows two time instances taken at t+3 and t+7, in which the evolution and the propagation of the magnetospheric flow systems in the equatorial plane that gave rise to the second perturbation FACs can be seen for three different B_Y cases. For all of the cases, a clockwise rotating vortex on the dawn and a counter clockwise rotating vortex on the dusk sector forms at t+3. These flow vortices were associated with an upward FAC on the dusk and a downward FAC on the dawn. The rotation sense of the vortices were opposite to the ones observed in the PI phase. Similarly the perturbation FACs associated with these vortices also had opposite senses of directions to those seen in the PI phase.

These findings are in alignment with the *Kivelson and Southwood* (1991) study which related the ionospheric vortices to magnetospheric vortices. They argued that as the pressure front propagated towards the tail, the shear flows created vortices that induced a FAC pair that was responsible for the magnetic perturbations observed at the ground. The MI vortices mapped to 7-8 R_E within the magnetosphere, whereas the PI flow anomalies mapped to 9-10 R_E distances. This also explains why the PI FACs mapped to higher latitudes in the ionosphere compared to MI FACs.

Figures 3.6 and 3.7 show that regardless of the initial FAC profiles, the magnetospheric response to solar wind dynamic pressure enhancement was very similar, with slight variations between the locations of the perturbed magnetospheric flow.

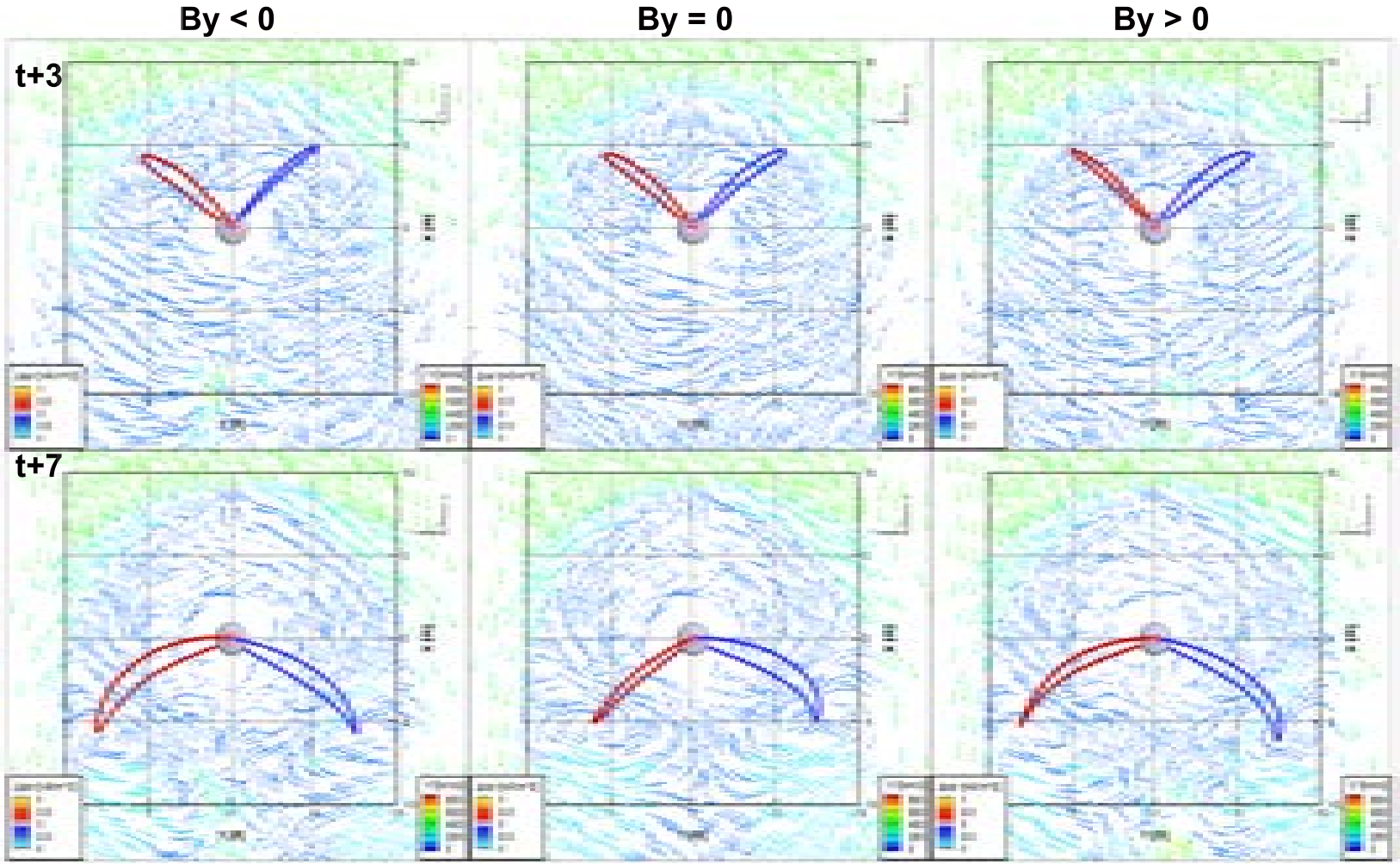

Figure 3.7: The equatorial magnetospheric flow profiles taken before the compression at t + 3 min. (top row), andt + 7 min. after the compression (bottom row) are shown. The arrows show the velocity vector, whereas solid lines show the magnetic field lines, colored based on the direction of the field-aligned current on the ionospheric foot point (red/blue-upward/downward). From left to right the columns show negative B_Y, zero B_Y, and positive B_Y cases.

3.4 Discussion

The high-latitude ground magnetometer perturbations in the global simulations show a two-step response to sudden solar wind dynamic pressure enhancements, namely the PI and MI phases. This two-stage response can be traced back to both the magnetosphere and the ionosphere due to the coupling through FACs. Evaluating the effects of the compression with different IMF B_Y orientations showed that although the magnetospheric and ionospheric responses were very similar, the differences in the pre-existing FAC system were responsible for the asymmetric ground magnetometer response.

3.4.1 PI Signature Under Different IMF B_Y

The PI signature has been historically associated with the wave mode conversion at the magnetopause at the time of compression [*Fujita et al.* (2003a); *Yu and Ridley* (2009)]. Due to the Alfven waves created by mode conversion from magnetosonic waves at the magnetopause, the currents carried by the magnetic field lines to the high-latitude ionosphere were enhanced. In Figure 3.3, the perturbation FAC system due to compression occurred at t+1. This happened within 1 minute of the compression of the magnetosphere and can be seen more clearly in both negative and positive IMF B_Y cases. When B_Y was zero, the perturbation currents were 0.1-0.2 $\mu A/m^2$ weaker than the nonzero B_Y case during the PI phase. The simulated locations of the perturbation FACs were upward in the pre-noon sector and downward in the post-noon sector around 70° magnetic latitude, which is consistent with those at 14 MLT at 73° magnetic latitude shown in Tian et al. [2016].

Figures 3.2a and 3.2b show that the PI-related response varies with magnetic latitude, longitude and time. The overall PI duration was around 1 minute at 50° magnetic latitude. As the latitude increased, the duration of the PI response also increased by 1 minute. At higher latitudes, the duration of the PI signature further

increased to 4 minutes. PI signatures peaked at t+3 for all three cases at the 5 MLT region. The largest negative perturbation was around 90 nT at 80° magnetic latitude, for the negative B_Y case. This peak value decreased to 60 nT for the zero and positive B_Y cases.

3.4.2 MI Signature Under Different IMF B_Y

The magnetospheric sources for the MI responses have been found to be the twin vortex structures [*Motoba et al.* (2003); *Yu and Ridley* (2009); *Sun et al.* (2014)]. The MI vortices appeared at t+3 in all three cases on the dayside and propagated towards the nightside. In all three cases, vortices rotated clockwise on the dawnside and counterclockwise on the duskside. The magnetospheric vortices were around 3 R_E wide, which is consistent with the derived spatial scales from Time History of Events and Macroscale Interactions during Substorms (THEMIS) observations by *Tian et al.* (2016). The magnetospheric vortices mapped back to the ionosphere in a reversed sense, i.e., clockwise at dusk and counterclockwise at dawn, which is consistent with the theoretical studies [*Motoba et al.* (2003); *Tanaka* (2007); *Zhao et al.* (2015)].

The MI FAC system had the same sense of direction as the R1 current systems and the pair was centered at 67° magnetic latitude when they formed which was slightly lower than the PI FAC system. The clockwise-rotating dawn vortex was associated with the downward FACs, while the counterclockwise-rotating dusk vortex was associated with upward FACs. The ionospheric FAC pairs propagated from the dayside towards the nightside ionosphere together with their magnetospheric counterparts.

In contrast to the *Araki* (1994a)model of SIs, where the polarity changes only between morning and afternoon sectors at the high latitudes, the simulated magnetic perturbations showed a more complex variation for PI-MI signatures. During negative and zero IMF B_Y conditions, there were no bipolar signatures between 11 and 13 MLT at 80° magnetic latitude. However the bipolarity occurred from negative to positive

at 10-23 MLT below 70° magnetic latitude and from positive to negative at 14-23 MLT above 70° magnetic latitude for these cases. There was also a weak positive to negative change between 60° and 70° around 3 MLT. This change can be seen at 7 MLT for positive B_Y case. The high-latitude response at 12 MLT also did not show bipolarity during positive B_Y.

3.5 Summary and Conclusions

The effects of sudden enhancements in the solar wind dynamic pressure under different IMF B_Y configurations were investigated using a global MHD model. In particular, 100 uniformly distributed virtual magnetometers were used to understand the global behaviour of the ground magnetic perturbations as functions of magnetic latitude, longitude, and time. The magnetospheric and ionospheric sources of these perturbations were investigated through magnetospheric flows, ionospheric FACs and magnetic field perturbations from magnetospheric and ionospheric currents. The findings can be summarized as follows:

1. Two different pairs of transient FACs occurred, with different directions at dawn and dusk sectors. These perturbations FACs for both PI and MI phases did not show significant differences during different IMF B_Y orientations, however the pre-existing NBZ current systems differed drastically for different y directions. The superposition of the transient FACs with these B_Y dependent NBZ currents created asymmetric responses.

2. The magnetic field perturbation contributions from FAC and Pedersen currents almost cancel each other, however there were asymmetries associated with these current systems as well. The total magnetic perturbation at the ground level was mostly due to the Hall current systems, with 12 MLT being the region where peak perturbation was recorded during negative B_Y, and 6 MLT being

the region where the peak occurred during the positive B_Y. For the zero B_Y simulations, there were two peaks located at 6 and 12 MLTs.

3. The magnetospheric sources for the PI and MI signatures were also identified. PI FACs mapped to the magnetopause boundary, whereas MI FACs mapped to well-defined flow vortices at dawn and dusk sectors. These vortices occurred at the dayside and propagated towards the nightside while at the same time the MI FACs occurred at pre and post-noon sectors, and propagated towards the nightside through the dawn and dusk sectors.

CHAPTER IV

A Case Study of a Sudden Solar Wind Dynamic Pressure Increase on the Geospace System

4.1 Introduction

The magnetospheric response to sudden dynamic pressure enhancements has been widely studied through theory and observations. *Kivelson and Southwood* (1991) was first to show that flow perturbations due to compression can excite a pair of vortices at dawn and dusk sectors with opposite senses of rotation. Their findings on the direction of the FACs as a result of such perturbed flows, had been confirmed by modeling studies and significantly resembled the FACs on the top of the ionosphere [*Fujita et al.* (2003a), *Fujita et al.* (2003b), *Kataoka et al.* (2004), *Motoba et al.* (2003), *Ozturk et al.* (2017), *Samsonov and Sibeck* (2013), *Yu. and Ridley* (2011), *Zhao et al.* (2015)].

The FACs at the top of the ionosphere and the horizontal ionospheric currents (Hall and Pedersen) can be reconstructed from ground magnetometer observations [*Kamide et al.* (1976), *Matsushita and Xu* (1982), *Untiedt and Baumjohann* (1993), *Weygand et al.* (2011), *Weygand et al.* (2012)]. It is known that the Hall currents are the most significant contributors to the observed magnetic field perturbations at ground levels under the assumption of a uniformly conducting ionosphere [*Fukushima*

(1969)]. Therefore, the reconstructed currents are very close approximations to the Hall current configurations [*Keiling et al.* (2009)].

Fukushima (1969) showed that the ionospheric flow patterns are antiparallel to the Hall currents. During sudden solar wind dynamic pressure enhancements these convection flows are significantly perturbed and traveling convection vortices are observed [TCVs; *Clauer et al.* (1984), *Friis-Christensen et al.* (1988), *Glassmeier and Heppner* (1992), *Honisch and Glassmeier* (1986), *Lanzerotti et al.* (1991)]. The PI and MI FACs that form as a result of sudden dynamic pressure enhancement [*Fujita et al.* (2003a), *Fujita et al.* (2003b), *Yu and Ridley* (2009), *Ozturk et al.* (2017)], can lead to TCV type twin vortices that form on the dayside and propagate towards the nightside. There are also theoretical and observational studies that showed connections between TCVs and magnetospheric vortices [*Glassmeier and Heppner* (1992), *Glassmeier et al.* (1989), *Keiling et al.* (2009), *Kim et al.* (2015), *Slinker et al.* (1996)].

The perturbation FACs significantly alter the ionospheric convection which in turn affects the ionosphere-thermosphere system. Even though the magnetospheric sources of the ionospheric perturbations in the convection profiles have been studied extensively, how the perturbed flows affect the I-T system is still not well understood. One of the most important studies on the topic was conducted by *Schunk et al.* (1994) using the Utah State University time-dependent ionospheric model. A pair of oppositely directed FACs were introduced to the simulation and propagated from dayside to the nightside with a speed of 3 km/s, mimicking the TCV observations. They showed that the local ion and electron temperatures were enhanced on the path of TCV. As a result, the NO^+ density increased, while the electron and O^+ densities were depleted [*Schunk et al.* (1994)].

The response of the I-T system to solar wind dynamic pressure enhancements has been discussed in various studies [*Valladares et al.* (1999), *Zou et al.* (2017), *Kim et al.* (2015), *Shi et al.* (2017)]. *Valladares et al.* (1999) used Greenland magnetome-

ter arrays and the Sondrestorm Super Dual Auroral Radar Network (SuperDARN) to show that magnetic perturbations larger than 100 nT at the ground were associated with elevated ion temperatures and plasma density depletions *Valladares et al.* (1999). Similarly, using the Poker Flat Incoherent Scatter Radar (PFISR), *Zou et al.* (2017), showed that ion temperatures increased by over 3000 K when PI and MI FACs propagated above the site. In addition, they found that there was a persistent electron temperature enhancement and an ensuing density drop in the F region [*Zou et al.* (2017)]. In addition, *Kim et al.* (2015) used SuperDARN and the European Svalbard Incoherent Scatter Radar to show electron and ion temperature enhancements. Their study also employed ground magnetometers to show pressure induced ionospheric vortical convection patterns in association with the enhanced temperature. Finally, using the Scanning Doppler Imager (SCANDI) they demonstrated significant variations in the thermospheric winds, providing evidence that the pressure can perturb the thermospheric system [*Kim et al.* (2015)]. Another significant study that shows thermospheric disturbances as a response to solar wind dynamic pressure enhancements was conducted by *Oliveira et al.* (2017). Applying the superposed epoch analysis (SEA) technique to the Challenging Minisatellite Payload and Gravity Recovery and Climate Experiment (CHAMP) measurements, they showed that the neutral mass densities were enhanced as a response to compression [*Oliveira et al.* (2017)]. Similarly, *Shi et al.* (2017), reported enhanced neutral mass density from CHAMP and Gravity Recovery and Climate Experiment (GRACE) measurements, coinciding with increased Poynting flux measurements from the Defense Meteorological Satellite Program (DMSP) during sudden dynamic pressure enhancement events. The OpenGGCM simulations for the event showed that the location of enhanced Poynting Flux coincided with the transient FAC systems [*Shi et al.* (2017)]. These studies show that the pressure enhancements in the solar wind not only can strongly influence the ionosphere system locally, but also can also cause global and long-lived

effects throughout the I-T system.

At high latitudes Poynting Flux can be used as a proxy of Joule heating, which is a key parameter when describing the momentum and energy transferred from the magnetosphere to the I-T system [*Knipp et al.* (2004)]. The sparseness of continuous high resolution measurements of ionospheric electric fields, electron densities and neutral winds make quantification of Joule heating using experimental measurements very difficult [*Deng and Ridley* (2007), *Thayer* (1998), *Verkhoglyadova et al.* (2016)]. The numerical modeling of the Joule heating is also challenging because the input used in most I-T models are empirical models which spatially and temporally smooth the electric field data [*Codrescu et al.* (1995), *Foster et al.* (1986), *Heelis et al.* (1982), *Thayer* (1998), *Weimer* (1996)]. Combined with the lack of realistic conductivity models, numerical modeling of Joule heating usually yields in a systematic underestimation [*Deng and Ridley* (2007), *Huang et al.* (2016), *Johnson and Heelis* (2005), *Verkhoglyadova et al.* (2016)]. In addition to the smoothing, most empirical models of the ionospheric electric fields do not accurately capture the dynamics of the active periods such as the solar wind dynamic pressure enhancements. Therefore, employing electrodynamics solutions from a first-principles model with high temporal and spatial resolution has the potential to significantly improve our current understanding of the geospace response to solar wind dynamic pressure enhancement events.

4.2 Methodology

The 17 March 2015 event, which was one of the most geoeffective events of solar cycle 24 [*Kataoka et al.* (2015), *Wang et al.* (2016)] was chosen for examination with MHD and global I-T models. The ionospheric disturbances have been reported in many studies [*Cherniak et al.* (2015), *Fagundes et al.* (2016), *Jacobsen and Andalsvik* (2016), *Liu et al.* (2016), *Verkhoglyadova et al.* (2016)]. In particular PFISR was at an ideal location to capture the propagation of shock-induced FAC and convection

vortices [*Zou et al.* (2017)].

4.2.1 Simulation Setup

For this study, the global MHD simulation was driven by the solar wind and interplanetary magnetic field (IMF) data obtained from the Wind spacecraft at L1, propagated to the upstream boundary at X = 32 R_E. The simulation results were shifted by 16 minutes to minimize the timing uncertainties stemming from the propagation of the solar wind values in the simulation domain. This value was determined by comparing the perturbations in the simulation to the observed compression time in the sym-H index which was at 0445 UT. Figure 4.1a shows the propagated solar wind measurements and IMF values for B_Y, B_Z, V_X, number density and the sym-H index between 0430 UT and 0515 UT. Figure 4.1b shows the B_Y, B_Z, V_X, number density and the pressure values taken from the simulations at the subsolar point for comparison. The red line marks 0445 UT, the arrival of the compression front to the Earth. Both the velocity and density values prior to compression were flat in WIND observations, however the simulated values in Figure 4.1b showed mild enhancements at 0442 UT, around 50 km/s and $3cm^{-3}$ respectively. These artificial compression signals in the upstream conditions may sometimes occur in numerical simulations, because the MHD solvers allow for small amounts of divergence of B to occur, which is then stabilized with waves generated close to discontinuities [*Powell* (1994), *Toth* (2000)]. Apart from this minor enhancement, the IMF values in the simulation closely resembled the WIND measurements. The V_X increased from 420 to 510 km/s, while the density increased from 18 to 58 cm^{-3}. The IMF B_Y was close to zero before the compression, leading to a symmetric configuration in the ionospheric FACs. However, with the start of the compression, B_Y turned positive and stayed positive until 0504 UT. This variation in B_Y is expected to create a dawn-dusk asymmetry in the ionospheric FACs [*Tanaka* (2001)]. IMF B_Z stayed northward, further intensifying

during the compression to 25 nT.

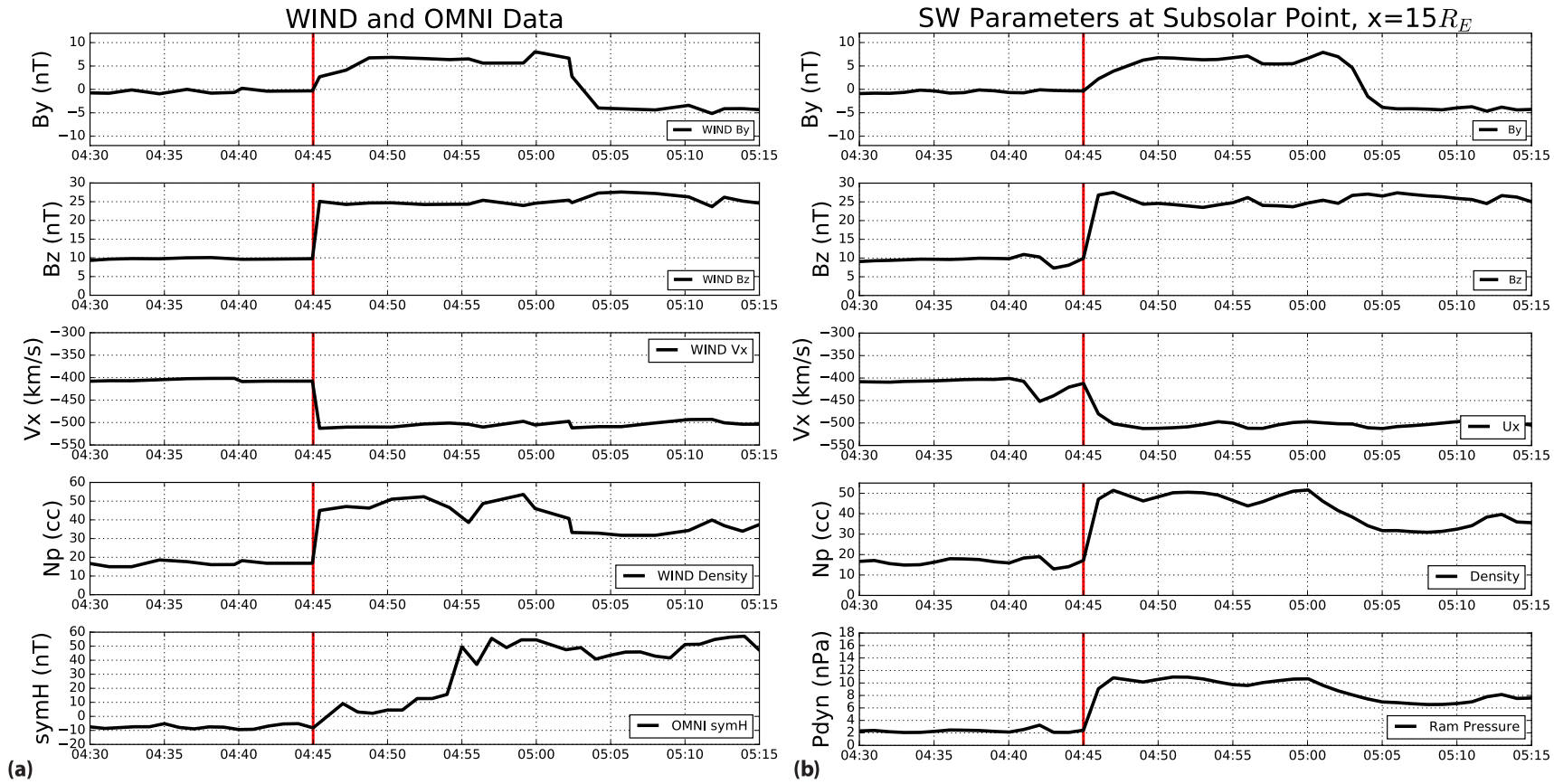

Figure 4.1: The Wind measurements of the IMF and solar wind plasma parameters, obtained from CDAWeb and the sym-H index, taken from OMNIWeb databases are shown on the left (a). Panels show IMF B_Y, B_Z, x component of the solar wind velocity, proton density and the sym-H index from top to bottom. The same parameters (except sym-H) are shown on the right taken from the simulation at the subsolar point (X=15 R_E) (b). The last panel on the right shows the variation of the simulated dynamic pressure. The solid red lines show the arrival time of the compression front, as detected by ground magnetometers.

For this study, the GM inner boundary was set to 2.5 R_E from the center of the Earth. The computational domain was a three-dimensional box in geocentric solar magnetospheric coordinates that started from 32 R_E upstream of the Earth in the X direction to 224 R_E tailward and -128 R_E to +128 R_E both in the Y and Z directions. The finest resolution was closest to Earth, where the cells had 1/8 R_E grid resolution.To understand the global magnetic signatures on the ground, 600 virtual ground magnetometers were implemented in each hemisphere uniformly from the magnetic equator up to 80° latitude (4° in latitude by 12° in longitude).

The results obtained from the coupled GM-IM-IE modules including convection and auroral precipitation then were used to drive the GITM. For this study, a spatial resolution of 4° in longitude to 1° in latitude was used for the region between 100 and 600 km. The GITM simulation was first driven by the empirical Weimer convection model *Weimer* (2005) and the Ovation aurora model *Newell et al.* (2002), from 15 March 2015 0000 UT, that was, 2 days before the event, to 17 March 2015 0405 UT, that was, 40 min before the compression, in order to allow the model to converge to a solution that was not affected by the initial conditions. These empirical models were run with the Wind measurements of the solar wind and IMF as inputs. From 0405 UT onward, the electric potentials and auroral precipitation obtained from the MHD simulation were used to drive GITM, updating the electrodynamic patterns every 10 seconds to better capture the temporal and spatial variations associated with the solar wind drivers.

4.2.2 Validation of the Simulation Results

In order to validate the model, the virtual magnetometer responses corresponding to the same locations of the SuperMAG ground magnetometers were used and the simulated results were compared with the measurements. Figure 4.2 shows the comparison of the Poker Flat (PKR) magnetometer measurements (red) with the virtual

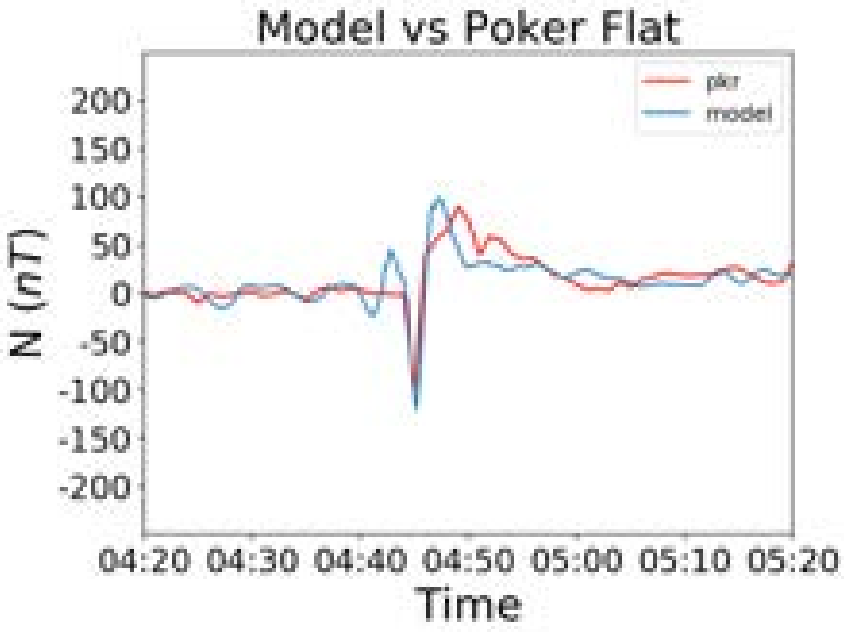

Figure 4.2: The comparison of the N-component of the Poker Flat (PKR) magnetometer observations (red) with the simulated magnetometer response (blue) extracted at the same location of PKR, during the solar wind dynamic pressure enhancement is shown. The negative preliminary impulse signature was observed at 0445 UT.

PKR magnetometer (blue) for the magnetic North component. After the baseline was extracted, the PKR magnetometer recorded a sharp decrease around 120 nT starting at 0445 UT, which was the PI signature associated with the SI. The PI dip was then followed by a positive perturbation of 100 nT that corresponded to the MI signature of the SI. The virtual magnetometer responded to the minor numerical compression shown in Figure 4.1a at 0442 UT. The good agreement between the MHD model results and the PKR observations demonstrated that the global MHD model captured the ionospheric drivers well at this location and could be used to drive GITM to further investigate the I-T responses over Poker Flat.

4.3 Magnetospheric Response

The magnetosphere response to compression is shown in Figure 4.3 for two time steps, 0446 UT and 0447 UT which corresponds to the MI phase. The formation of the magnetospheric vortices at the dayside (0446 UT) and their propagation towards the nightside (0447 UT) can be seen clearly. The vortex on the dawn, which was centered at X=3 R_E, Y=-5 R_E, had a clockwise sense of rotation and was associated with a downward FAC. This vortex mapped to the 69° magnetic latitude and 9 MLT at the top of the ionosphere at 0446 UT. The vortex on the dusk, which was centered at X=6 R_E, Y=-4 R_E, had a clockwise sense of rotation and was associated with a downward FAC. This vortex mapped to the 72° magnetic latitude and 15 MLT at the top of the ionosphere at the same time.

The propagation of these two vortices can be seen in Figure 4.3b at 0447 UT. The dawn vortex was centered at X=-1 R_E, Y=-6 R_E, mapping to 7 MLT and 68° magnetic latitude. Similarly, the dusk vortex was centered at X=-1 R_E, Y=+6 R_E, mapping to 17 MLT and 66° magnetic latitude at this time step. These vortices propagated towards the nightside and eventually dissipated around 0515 UT.

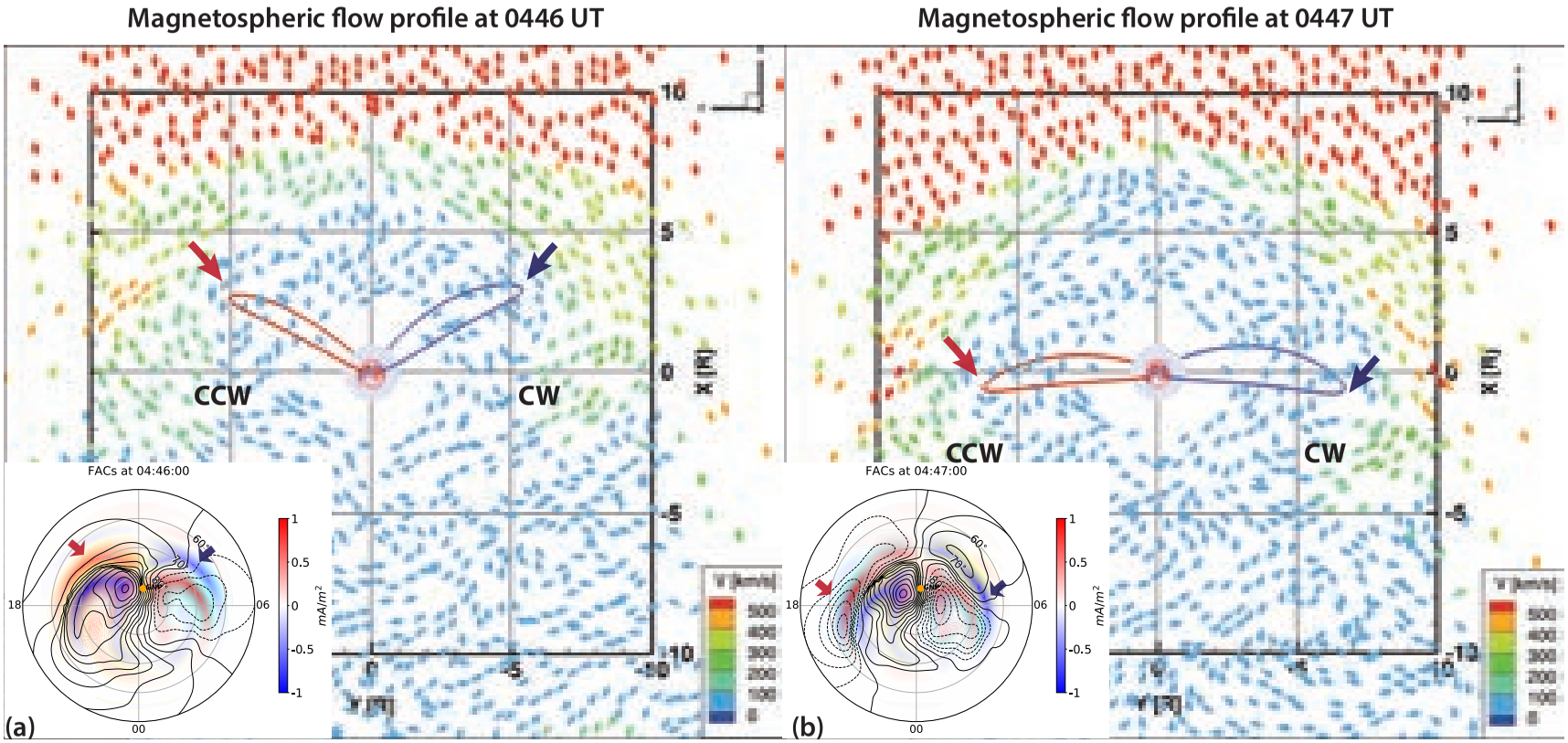

Figure 4.3: The simulated equatorial magnetospheric flow profiles taken at 0446 UT(a) and 0447 UT(b) are shown. The arrows show the flow vectors color coded according to their velocities. The magnetic field lines that show the perturbed flow associated with the main impulse phase are shown and color coded according to the direction of the current carried (red, upward; blue, downward). The footprints of these magnetic field lines on the top of the ionosphere are shown in the bottom left corners.

4.4 Ionospheric Response

The ionospheric response to the sudden solar wind dynamic pressure enhancement was examined through FACs, Joule heating, ion temperature and convection profiles and the global variations in the N component of the magnetic perturbations recorded by the virtual ground magnetometers. The variation of these profiles at key time steps are shown in Figure 4.4. The ionospheric temperatures and convection results were extracted from the GITM simulations, and they are in geographic coordinates as opposed to the other profiles shown in Figure 4.4.

The FAC profile at the quiet time, 15 minutes before the arrival of the compression front, showed symmetrical upward and downward FAC profiles since the IMF B_Y was very close to zero at the time. The Joule heating profile was mostly zero as shown in the second row of Figure 4.4a. The non zero locations corresponded to the boundary between upward and downward FACs of the NBZ current system at the dawn and dusk sectors. The electric field potentials were condensed at these locations. The ion temperature and convection profiles at 227 km are shown in the third row. This altitude was chosen to best display the response of the ions to convection. The ion temperature was around 1000 K, with slight enhancements to 1200 K at the midnight region. The N components of the magnetic field perturbations are shown in the fourth row. The overall profile was very close to an unperturbed state, with weak positive perturbations at high latitude midnight and negative perturbations at the low latitude pre-midnight sector.

The system responded to the compression immediately at 0445 UT, which corresponded to the PI phase of the SI. The perturbed profiles at this time instance are shown in Figure 4.4b. A perturbation FAC pair occurred on the dayside as a response to compression, with an upward cell on the dawn and a downward cell on the dusk, both centered around 70° magnetic latitude. Respectively, the Joule heating was enhanced above 25 W/m^2 at the noon sector around 70° magnetic latitude, which was

located in between the oppositely directed PI FAC pairs. The ion temperature at the same location was also immediately enhanced to 2500 K. As a response to PI-FACs, a clockwise rotating ion convection vortex occurred at the dawn and a counter clockwise rotating ion convection vortex occurred at the dusk regions. Largest convection flows were located again at the region between PI-FACs. The PI signature at the virtual ground magnetometers showed the dawn-dusk asymmetry previously discussed in the Araki's model *Araki* (1994b). The high latitude (70°-80°) dawn sector showed negative perturbations, whereas the dusk sectors showed positive perturbations. The mid latitude (60°-70°) virtual magnetometers recorded positive perturbations at the dawn sector and negative perturbations at the dusk sector. The lower latitude virtual magnetometers (¡ 60°) showed positive perturbations at the dayside and negative perturbations at the nightside.

The system response at 0446 UT, 1 minute after the compression, is shown in Figure 4.4c. Another pair of perturbation FACs arose on the dayside, marking the start of the MI phase. This FAC pair had an upward cell on the dusk and a downward cell on the dawn, opposite to the PI-FAC pair, centered around 68° magnetic latitude. The magnetospheric sources of these FACs are shown in the Figure 4.3a. At this time instance, Joule heating at dawn and dusk regions were enhanced. Similarly, the ion temperatures and convection speeds were enhanced at these locations, dusk-side temperatures and velocities being higher than the dawn-side. The magnetic perturbation profile stayed similar to 0445 UT, despite weakening. One exception was seen at 9 MLT high-latitude, where a positive perturbation was recorded.

The perturbations associated with the MI phase became more dominant at 0447 UT, which is shown in Figure 4.4d. The MI-FACs propagated towards the flanks and started extending to the nightside. The Joule heating was highest at the locations in between MI and PI FACs at dawn and dusk sectors. The biggest change was seen at the ion convection profiles. The ion convection vortices had changed senses

of rotation, as opposed to the ones at PI phase. The overall negative magnetic perturbation patches weakened, whereas the positive perturbation recorded at 9 MLT strengthened. In addition low latitude response became positive at the nightside.

At 0448 UT, the MI-FACs dominated the FAC profile at the top of the ionosphere as can be seen from Figure 4.4e. The MI-FACs elongated from dayside to the nightside. The Joule heating profile was highest at the same locations, between PI and MI FACs at this time step. However, the ion convection speeds were faster at this time instance, correspondingly the ion temperatures were higher than the previous time instance. Overall magnetic field perturbations showed a negative behaviour at high-latitude dusk and low-latitude dawn, in addition to the positive behaviour at low-latitude dusk and high-latitude dawn. Due to the compression of magnetopause currents, overall low-latitude response became positive.

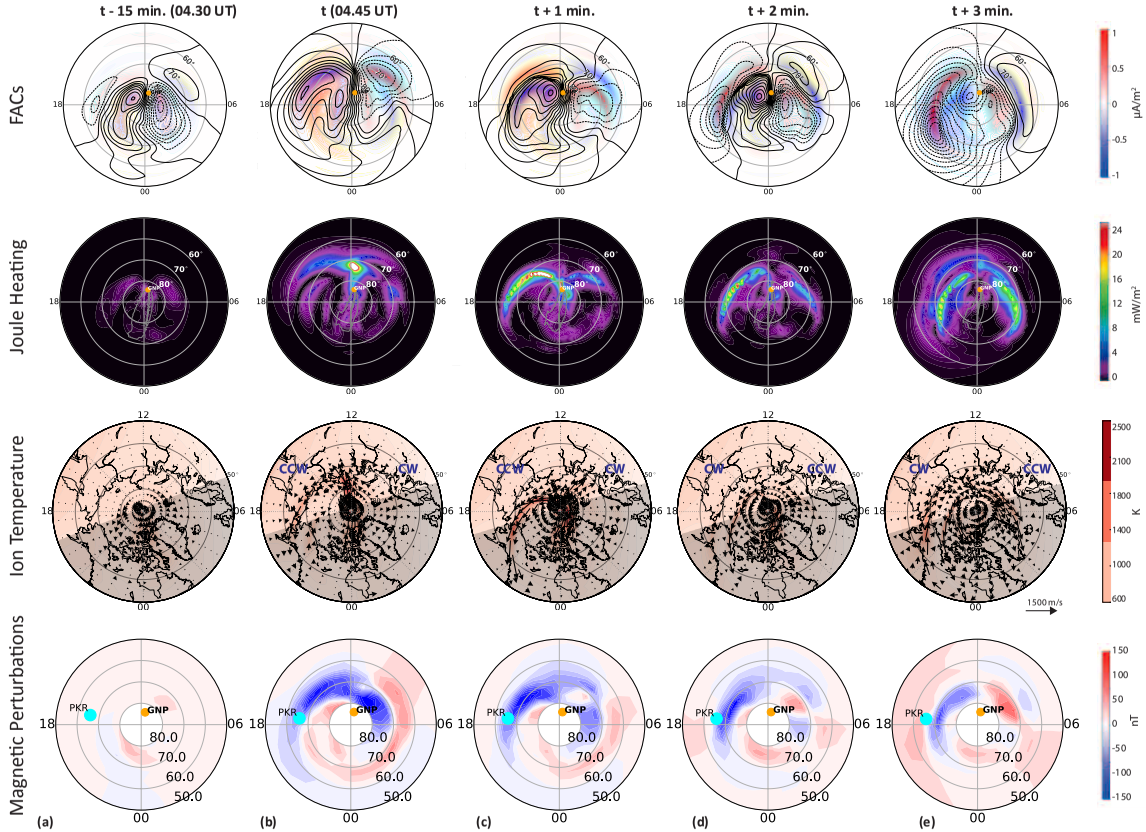

Figure 4.4: The simulated FACs (first row), Joule heating (second row), ion temperature and convection profiles at 227 km (third row), and the N component of the magnetic field perturbations (fourth row) are shown at the quiet time (a), 0445 UT (b), 0446 UT (c), 0447 UT (d) and 0448 UT (e). The cyan dot shows the location of the PKR magnetometer, and the orange dot shows the location of the geographic north pole (GNP) in the fourth row.

The ionospheric and thermospheric responses to SI at 19 LT were further investigated. This location corresponded to where PFISR was located (blue dot in Figure 4.4). The ion and neutral temperature profiles between 100 km to 600 km from 50° to 90° latitudes were extracted and displayed in three time instances 0430 UT, 0445 UT, 0446 UT in Figure 4.5. The ion convection flows were also contoured with solid and dashed lines over the temperature profiles. The unperturbed ion and neutral temperature profiles are shown in Figures 4.4a and d. The ion temperature profile displayed an altitude dependent profile, with the exception of the high temperature region near the geographic pole. The neutral temperature profile showed peaks at two latitudes, 50° and 90°.

Both the ion and neutral temperature profiles showed an immediate response to the PI phase shown in Figures 4.4b and e. There were mild enhancements, around 500 K in the ion temperature at 64°, 75°, 82° and 89° latitudes, corresponding to the locations of enhanced Joule heating rates in the Figure 4.4b. The neutral temperature showed an enhancement of 10 K around 65° latitude.

The beginning of the MI Phase, 0446 UT, is shown in Figures 4.4c and f. A significant enhancement of 1000 K was seen at the ion temperature profile around 68° latitude, and another enhancement of 500 K was seen around 88° latitude, extending all the way down to 120 km. Similarly, the neutral temperature profile showed an enhancement around 20 K at the same locations, extending to 200 km. The enhanced temperature regions were colocated with the regions of high ion convection speeds. The flow speeds exceed 750 m/s at the 68° latitude, and 1000 m/s at the pole region. During these time instances, there was also a constant background cooling in the ion and neutral temperature profiles, due to the region being close to the terminator.

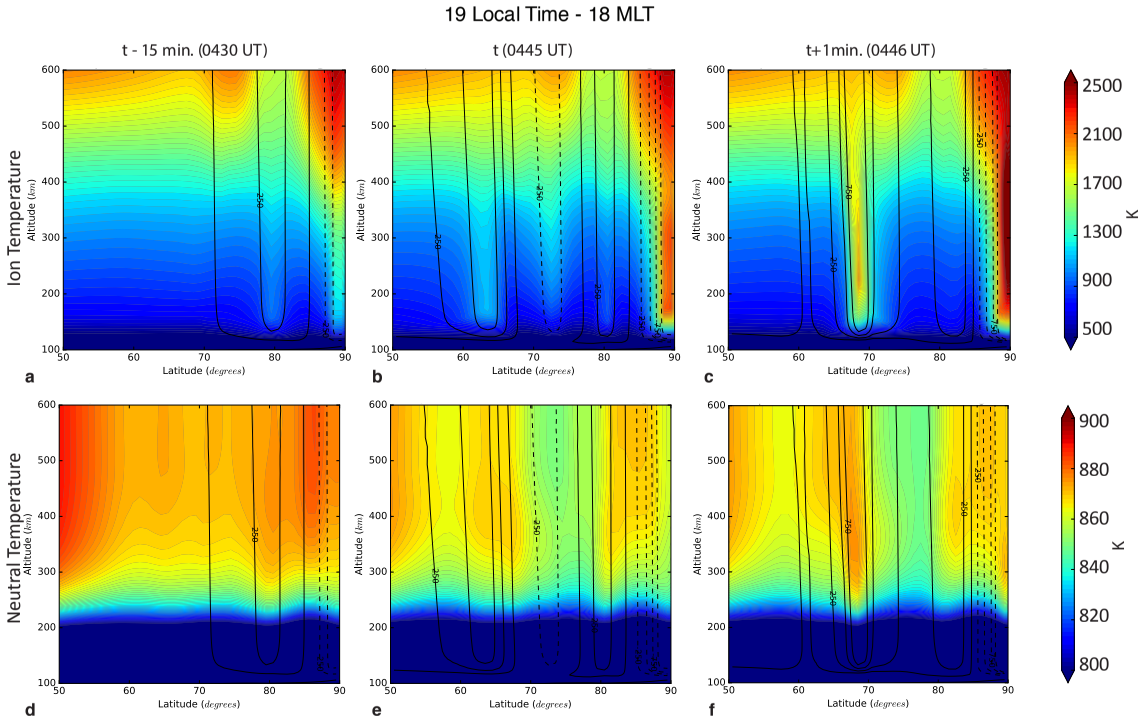

Figure 4.5: The vertical (100-600 km) profiles for the ion temperature (top row) and neutral temperature (bottom row) taken at 19 LT (18 MLT) between 50° and 90° latitudes taken at quiet time (a/d), 0445 UT (b/e) and 0446 UT (c/f) are shown. The solid (dashed) lines show the eastward (westward) convection velocity.

The altitude profiles of the simulation outputs were extracted along the heating channel (at 198° longitude and 68° latitude) were extracted which was also very close to the PFISR location (at 214° longitude and 65° latitude). The modeled altitude profiles for ion temperature, electron temperature, and density were averaged every 5 min to match the PFISR observations, which were long pulses that were integrated every 5 min to improve the signal to noise ratio. The comparisons of the modeled results with the PFISR measurements are shown in Figure 4.6. The averaged GITM ion temperature increased around 500 K during the compression. However, the vertical profile at 0446 UT without averaging (dotted line) shows that the peak enhancement was about 1000 K above the background temperature at the time of compression and the averaging results in an under-estimation of the overall profile.

The PFISR observations demonstrated that the peak ion temperature enhancement was about 2000 K and occurred around 200 km. The simulated electron temperature also showed an enhancement around 200 K during the perturbation but then dropped to values lower than the unperturbed state after 0455 UT. Conversely, the PFISR measurements of electron temperature showed a larger increase over a longer duration. The electron density, shown in the bottom panels, decreased around 20% after the compression in the GITM simulations. The drop in the electron density was more drastic in the PFISR measurements, with a peak drop of about 50% at 300 km.

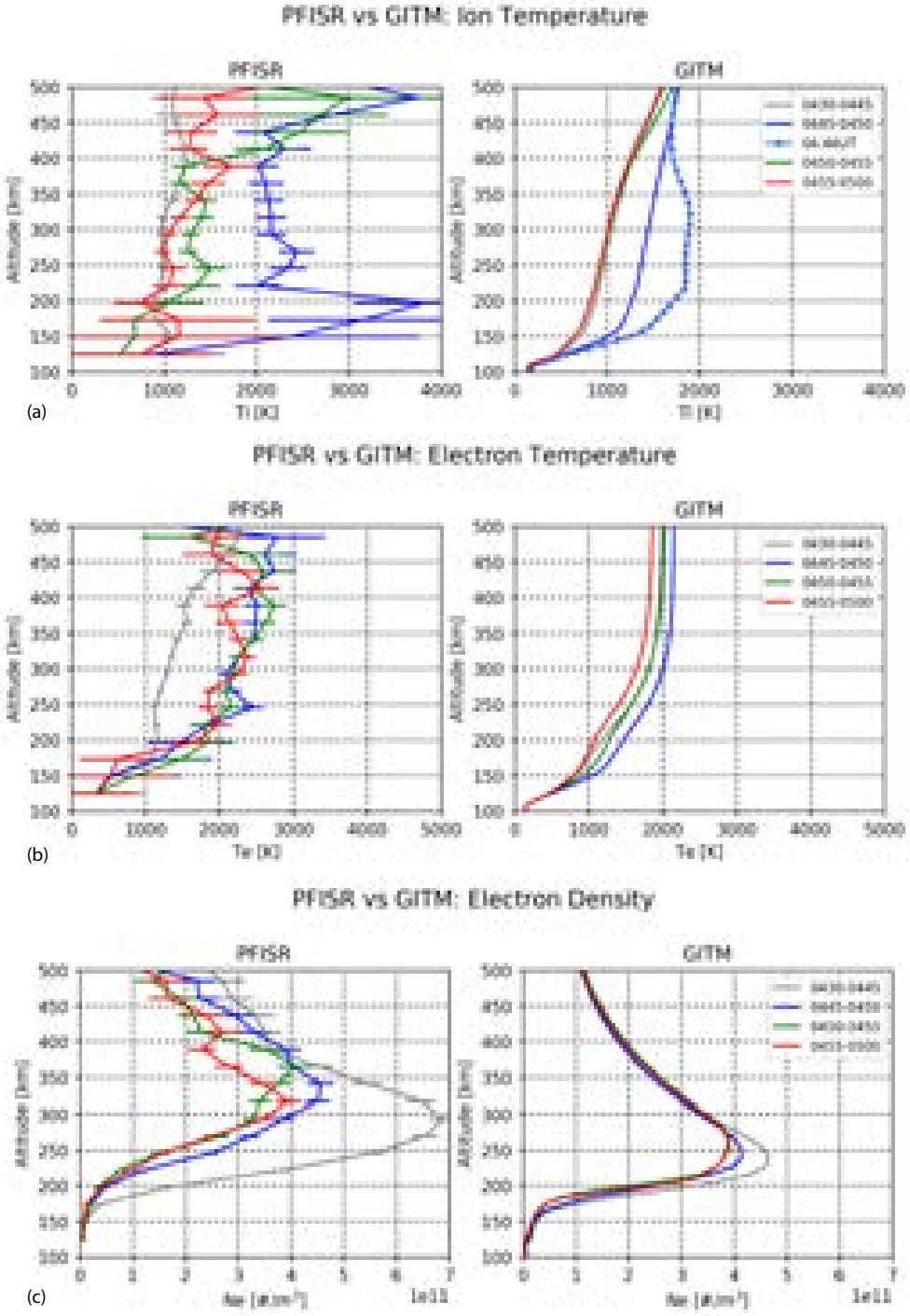

Figure 4.6: The vertical (100-600 km) profiles of ion temperature (a), electron temperature (b) and electron density (c) are shown. The panels on the left show PFISR observations, whereas the panels on the right show the simulated responses extracted at the same location. The colors show the time-averaged profiles for before the event (0430-0445 UT) in gray, during (0445-0450 UT) in blue, immediately after (0450-0455 UT) in green and after (0455-0500 UT) in red. The dotted line shows the profile extracted at 0446 UT.

Overall, the comparison of PFISR observations with GITM simulation results showed that the I-T system was significantly perturbed, but the amplitudes of the perturbations were larger than the simulation results showed, especially in electron density and temperature. Figure 4.7 shows the altitude profiles for densities of NO^+ and O^+, as well as the neutral temperature taken at the same location as the heating channel. The top panels shows that NO^+ was initially enhanced by 20% at around 180 km, followed by a subsequent 10% decrease. However the O^+ decreased by 25% during the compression, similar to the electron density drop shown in Figure 4.6c. The drop in both species is consistent since the O^+ is the main constituent in the F region. The neutral temperature shown in the bottom panel of Figure 4.7 was initially enhanced above 200 km, but later demonstrated a wave-like structure. The initial enhancement was about 10 K, which later dropped 10 K below the initial temperature, later recovering and approaching closer to the initial temperature profile.

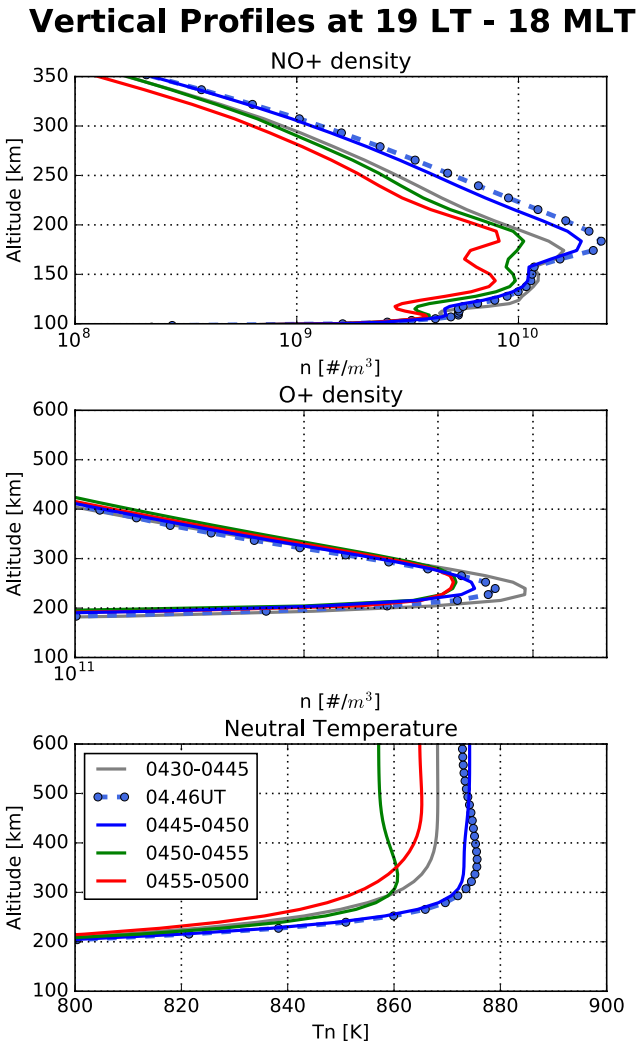

Figure 4.7: The vertical (100-600 km) density profiles for NO^+ (top) and O^+ (middle) and the neutral temperature are shown. The colors show the time-averaged profiles for before the event (0430-0445 UT) in gray, during (0445-0450 UT) in blue, immediately after (0450-0455 UT) in green and after (0455-0500 UT) in red. The dotted line shows the profile extracted at 0446 UT.

4.5 Discussion

The Earth's magnetosphere was rapidly compressed as the solar wind dynamic pressure suddenly increased, causing deformation of the magnetopause boundary, reconfiguration of the magnetospheric and ionospheric flow profiles as well as the M-I

current systems. The perturbation FACs that arose as a response to SI, were similar to those shown by various other numerical simulation studies [*Slinker et al.* (1996), *Fujita et al.* (2003a), *Kataoka et al.* (2003), *Yu. and Ridley* (2011), *Ozturk et al.* (2017)] and to equivalent current systems constructed from observations [*Kamide et al.* (1976), *Matsushita and Xu* (1982), *Untiedt and Baumjohann* (1993), *Weygand et al.* (2011), *Weygand et al.* (2012)]. These perturbation FACs were super-imposed on the preexisting NBZ current system. The resulting ion convection patterns had similar physical properties to those of the TCVs [*Clauer et al.* (1984), *Engebretson et al.* (2013), *Friis-Christensen et al.* (1988), *Glassmeier and Heppner* (1992), *Honisch and Glassmeier* (1986), *Kim et al.* (2015), *Lanzerotti et al.* (1991), *Zesta et al.* (2002)]. The simulated ionospheric convection vortices arose near 70° latitude on the dayside and propagated towards the nightside. The convection electric field and auroral precipitation patterns from the coupled MHD model that were used to drive GITM simulations, proved to be very effective to drive the I-T system. The GITM simulations showed enhanced ion temperature and velocities at locations where electric field potentials were densest. Despite the short duration of the perturbations, the neutral temperatures were also enhanced by around 20 K.

During the propagation of the ionospheric convection vortices, simulation results showed significant ion temperature enhancements that exceed 1000 K extending to 200 km altitude. These results are consistent with the PFISR observations shown by *Zou et al.* (2017). Likewise, the EISCAT radar data presented by *Kim et al.* (2015) showed enhancements between 1000-3000 K in the ion temperature as a response to the TCV propagation between 150 to 300 km. Another TCV simulation by *Schunk et al.* (1994) showed a similar enhancement in ion temperature which was around 3000 K with the peak occurring at 220 km. One possible reason for the underestimated ion temperature enhancements between the GITM simulations and the PFISR observations could be the disparity in the ion convection vectors, which peak at around 720

m/s in the GITM simulations but reach up to 2000 m/s in the PFISR observations as reported in *Zou et al.* (2017).

Another underestimated response was observed in the electron temperature variations both amplitude and duration-wise. Estimating electron temperature is the key to successfully model the electron recombination processes in the I-T system. The peak enhancement in electron temperature, which was about 300 K occurred at 200 km in GITM simulations at the location of the heat channel. This enhancement was not as large as the electron temperature enhancements reported in *Kim et al.* (2015) and *Zou et al.* (2017). The EISCAT observations showed an electron temperature enhancement of 1000-3000 K between 200 and 300 km, while the PFISR observations reported in the latter showed an increase of 500-1000 K between 150 and 450 km. The electron temperatures also remained higher for a longer duration as shown in the PFISR observations plotted in Figure 4.6a.

The modeled ion and electron temperatures showed similar behaviour to the observed ones during the TCV events; however, the magnitude difference is noteworthy. The disparity between the unperturbed electron density and temperature profiles in GITM results and the PFISR observations indicates that there exists a fundamental process that was either not included in GITM that can cause rapid heating of the electrons or was missed in the MHD simulation or not passed to the GITM. For example, as investigated in detail by *Zhu et al.* (2016), the electron heat flux has great effects in the plasma temperature and density. In the current GITM version, the electron heat flux was added uniformly in the subauroral region mimicking the ring current effects but not in the auroral zone, which can lead to an underestimation of the plasma temperature there. In addition, the underestimated electron temperature also affects the calculation of ion temperature [*Wang et al.* (2016)] causing lower enhancements in the ion temperature during the perturbed state.

Another reason for the low ion temperatures in the simulations results, in addition

to the low auroral precipitation, can be the underestimated Joule heating in the model [*Deng and Ridley* (2007), *Verkhoglyadova et al.* (2017), *Zhu et al.* (2016)]. In GITM, the ion and electron temperatures are solved for in a time-accurate mode, which indicates how strongly the ion temperatures are controlled by the localized, instantaneous Joule heating. The Joule heating shown in Figure 4.4 was calculated from the IE/RIM model results and even though it is higher than the heating in *Verkhoglyadova et al.* (2017), which used the electric potentials derived from the *Weimer* (2005) model to drive the GITM simulations for the same event, it might not be sufficient overall.

The rise in the ion temperature leads to increased rates for charge exchange reactions, causing rapid conversion of O^+ to NO^+, followed by enhanced recombination [*Schunk and Nagy* (2009)]. This process is responsible for the observed and simulated drops in the O^+ and electron densities. The simulated electron density was in general lower compared to the PFISR observations. This could again be a result of the underestimated auroral precipitation from the MHD model [*Deng and Ridley* (2006), *Slinker et al.* (1996), *Sojka et al.* (1997), *Wilson et al.* (2006), *Zhang et al.* (2014)].

Despite the short duration of the perturbation (30 minutes overall), the enhancement in the neutral temperature was noteworthy (5-15 K). In order to understand how the separate phases of the SI can affect the thermosphere, the three transfer rates that were shown in Equation 1.38 were calculated using state variables from the GITM simulation results at the same location where the highest heating occurred. The values of these three heating terms, collisional, frictional and vertical conduction rates at 0446 UT are shown in Figure 4.8. The ion to neutral collisional heat transfer and the ion-neutral frictional heating rates were very similar and peaked at 240 km. The collisional heat transfer rate was around 0.1 K/s larger than the frictional heating term between 200 and 400 km. After the ion and neutral temperatures were enhanced near 240 km, the temperature gradient led to enhanced vertical thermal conduction.

Between 100 and 370 km, vertical heat conduction was negative, and above 370 km, it was positive. This can be inferred as the thermosphere below 370 km was cooled by conducting heat upward and downward, whereas above 370 km, the thermosphere was heated by the upward conduction from lower altitudes, since the peak in neutral temperature was around 370 km as shown in Figure 4.5f.

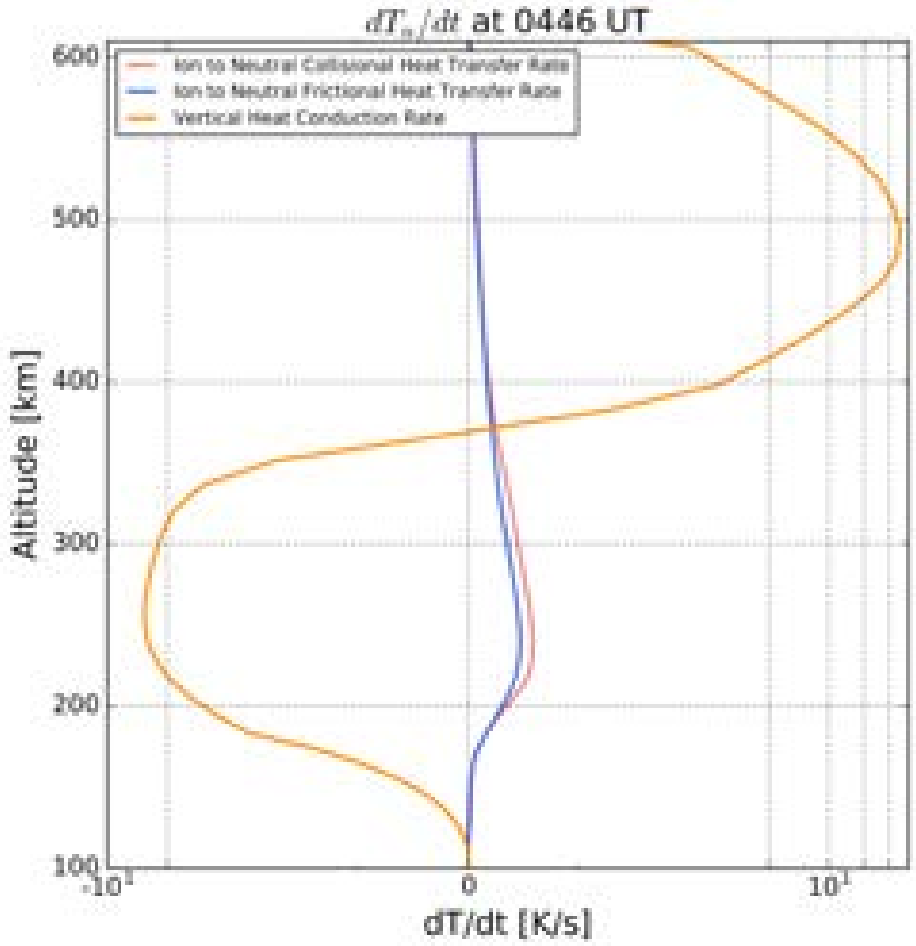

Figure 4.8: The vertical profile (100-600 km) of the contributions from the ion to neutral collisional heat transfer (red), ion to neutral frictional heat transfer (blue) and neutral vertical heat conduction rates (orange) are shown at 0446 UT at the simulated PFISR location.

The temporal variation of the neutral and ion velocities extracted at 240 km are shown in Figure 4.9a. The initial response of the ion and neutral velocities to the

numerical shock discussed in the methodology section (see Section 4.2.2) can be seen prior to 0445 UT. Overall, there were two peaks in the ion velocity, one at 0446 UT and another one at 0448 UT which were around 1000 m/s over the background speeds with the PI peak being larger than the MI peak. The neutral velocity only had two peaks, one associated with the numerical pressure enhancement and one after 0445 UT, which was directly associated with enhanced ion velocities.

The temporal evolution of the ion to neutral collisional (red) and frictional (blue) heating rates at 240 km are shown in Figure 4.9b. Similar to the ion velocity, there were four peaks in both rates. The peaks after 0445 UT, are directly associated with PI and MI phases of the SI and both terms were enhanced by an order of magnitude. The collisional heating term was larger than the frictional heating term at 240 km. Combined, the collisional and frictional heating terms were able to deliver 1 K/s of heating to the neutrals at 0446 UT, which was around 60 K/minute. From these rates and velocity variations, it is clear that the thermosphere response to an SI was immediate and caused by frictional and subsequent collisional heating from ions to neutrals. There was a constant background cooling in the system, that was not shown in Figure 4.9b, due to the decrease in the solar EUV radiation. This resulted in vertical conduction extracting heat from the upper thermosphere system.

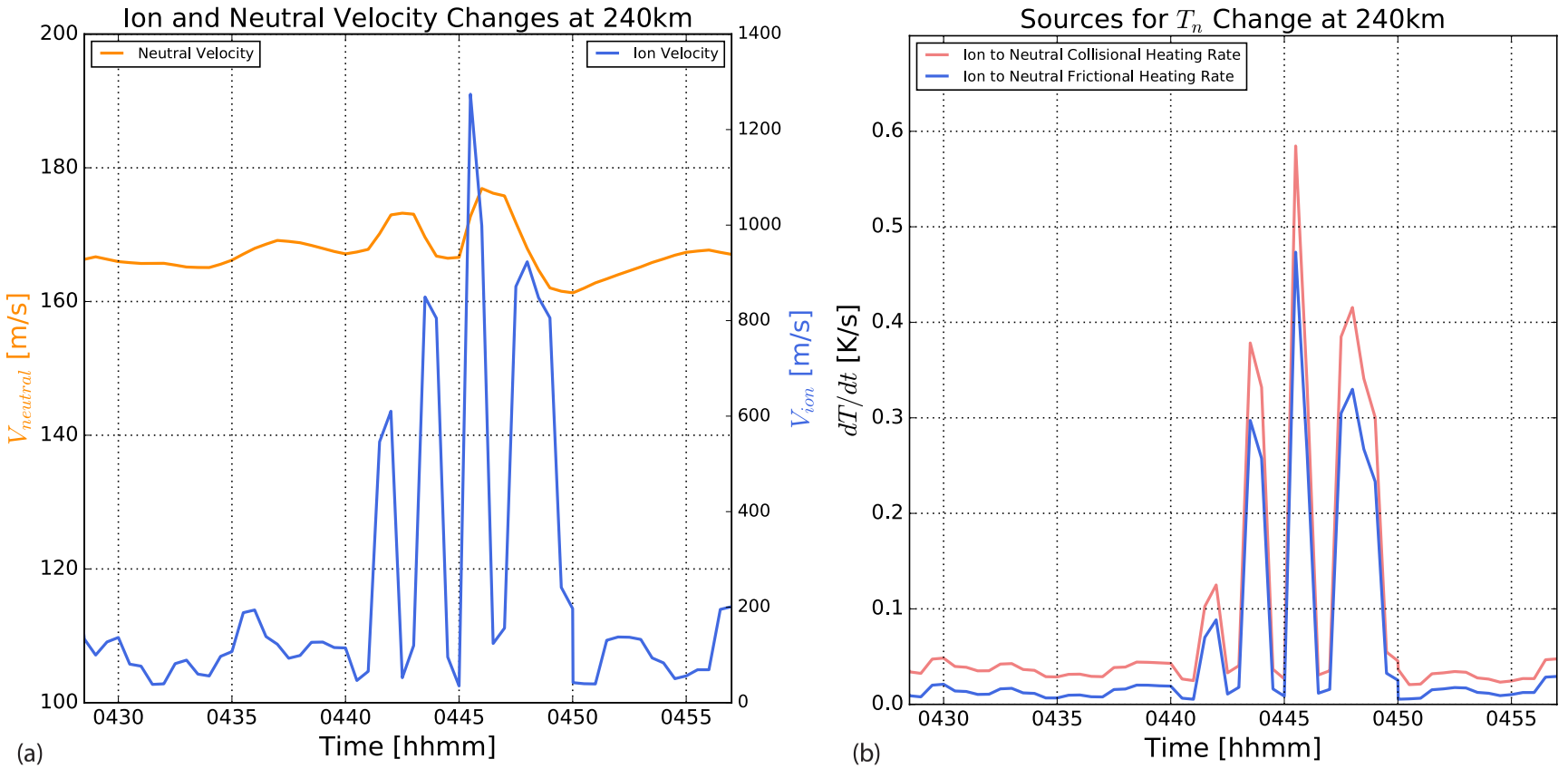

Figure 4.9: The temporal variations of the ion (blue) and neutral (orange) velocities are shown on the left (a), while the collisional (red) and frictional (blue) heating rates are shown on the right (b) at 240 km over the PFISR location.

4.6 Summary and Conclusions

The investigation of the 17 March 2015 sudden storm commencement through global numerical simulations revealed that the solar wind compression of the magnetosphere significantly perturbed the ionosphere and thermosphere systems. The scarcity of available observations prohibited the examination of these three systems all at once, but with the help of high-resolution, global solutions the transient response to compression was captured. The findings of this study can be summarized as follows:

1. The high-latitude electric field potentials and the convection patterns were perturbed during the compression. The ionospheric flow speeds exceeded 1000 m/s, in particular between PI and MI FACs.

2. The ion temperature enhancements were above 1000 K where the ion convection speeds were highest, due to the frictional heating. The observed ion temperature enhancement was even higher than the modeled results, indicating the frictional heating rates were underestimated.

3. The peak collisional and frictional heat transfer rates between ions and neutrals and the peak ionospheric density were co-located at 240 km. Both heating rates were similar in magnitude and delivered 60 K/min to the neutrals.

4. The O^+ and electron density dropped due to charge exchange rates increasing proportionately with the ion temperature. NO^+ density increased.

5. The underestimated perturbation in electron temperature indicated that modeling efforts lack some magnetospheric heat source for electrons, such as heat flux.

CHAPTER V

A Case Study of a Sudden Solar Wind Dynamic Pressure Decrease on the Geospace System

5.1 Introduction

The solar wind dynamic pressure directly affects the shape and size of the Earth's magnetosphere. The variation in the solar wind causes global changes in the magnetospheric configuration, disrupts the magnetospheric and ionospheric current systems and results in large scale flow perturbations [*Samsonov and Sibeck* (2013), *Kivelson and Southwood* (1991), *Fujita et al.* (2003a), *Fujita et al.* (2003b), *Yu. and Ridley* (2011)]. The response of the geospace system to the sudden enhancement of the solar wind dynamic pressures, known as sudden storm commencements (SSCs) or sudden impulses (SIs), [*Araki* (1994a)] has been traditionally studied using ground magnetometer observations of magnetic field perturbations at the ground level. These signatures had temporal, latitudinal, and longitudinal dependencies [*Araki* (1994a), *Araki* (1994b), *Sun et al.* (2014)] indicating that they have different magnetospheric and ionospheric sources [*Fujita et al.* (2003a), *Fujita et al.* (2003b), *Kivelson and Southwood* (1991)]. The high-latitude magnetometer observations of SIs showed that the compression signature can be decomposed as a short-lived Preliminary Impulse (PI) and a succeeding longer-lived Main Impulse (MI) [*Araki* (1994a), *Araki* (1994b)].

These impulse signatures create a bipolar response, with a polarity dependent on the magnetic local time. Therefore, investigating the physical processes which lead to the formation and propagation of the SI signatures, became an important aspect of understanding solar wind magnetosphere interaction.

Apart from the SI events related to the solar wind dynamic pressure enhancements, which will be referred to as SI^+ from here on, the solar wind dynamic pressure decrements can also cause global disruptions in the geospace system. *Araki and Nagano* (1988) showed that high-latitude ground magnetometers also observed bipolar responses but different polarities during sudden expansions of the magnetosphere after the solar wind dynamic pressure dropped. In addition, they used geosynchronous spacecraft measurements to show that the magnetic field parallel to Earth's rotation axis also decreased as a result of expansion. Ground magnetometer observations at lower latitudes showed that these perturbations were preceded by an initial positive perturbation. Apart from this initial positive perturbation at the low-latitudes, they concluded that SI^-s can be well explained by the same model derived for SI^+s [*Araki* (1994a)]. However, only a total of five events were investigated in this study, which was not sufficient to conclusively determine whether the SI^- events were mirror images of the SI^+ events. In addition, this model was not able to explain the initial positive perturbation observed at the low-latitudes.

To explain the distribution and the polarization of the SI^-s further, *Takeuchi et al.* (2000), conducted a study using higher temporal resolution data from ground magnetometers. Their study further distinguished the SI^- signatures from the mirror image of an SI^+, by showing the resemblances between two impulse signatures for certain locations on the ground. They further investigated the SI^- response with a larger data set consisting of 28 events [*Takeuchi et al.* (2002)], concluding that the SI^- generation can be explained by simply reversing the direction of the electric field which occurs due to the motion of the magnetopause. They also concluded that

compression and expansion mechanisms would lead to oppositely rotating ionospheric vortices but since the magnetic field produced by the vortices change direction at a fixed point on the ground due to the tailward propagation of these vortices, SI^{-}s and SI^{+}s both can produce polarity distributions alike.

As opposed to the SI^{+}s, there is no evident link between geomagnetic storms and SI^{-}s, but there are studies on the relationship between SI^{-}s and geomagnetic activity. *N.Sato et al.* (2001) was the first one to show that the optical aurora can be enhanced due to solar wind dynamic pressure drops. They investigated a sharp dynamic pressure drop from 12 nPa to 2 nPa and used DMSP-F13 satellite measurements to show enhanced electron precipitation, and an associated upward FAC system. They argued that field line resonance might be the reason for the acceleration of electrons, as opposed to loss-cone instability which is responsible for the enhanced optical emissions during SI^{+}s. *Liou* (2007) further investigated the link between SI^{-}s and geomagnetic activity with a data set of 13 large solar wind dynamic pressure decrement events. Using the ultraviolet imager on board Polar satellite and ground magnetometer observations, they found that 3 out of the 13 events were associated with substorms, however an increase in the open flux was necessary regardless of the amplitude of the dynamic pressure drop that triggered a substorm. Another optical emission study by *Belakhovsky and Vorobjev* (2016) showed that the auroral intensity was increased and the auroral structures propagated poleward as a response to the SI^{-}. Their results highlighted that the auroral response to SI^{-}s were highly complex and could prevail even after 15 minutes from the onset of the dynamic pressure drop, later leading to the dimming of the aurora.

The formation and propagation of global perturbations as a response to SI^{-}s are not well understood, since most of the aforementioned studies rely on scarce observational data. One important modeling work on SI^{-}s was conducted by *Fujita et al.* (2004). They found that similar to the SI^{+}, oppositely directed FAC pairs form

as a result of magnetospheric expansion, namely at the PI^- and MI^- phases, which map to vortical flows in the magnetosphere. However, the formation mechanisms for these vortices remain unclear. *Zhao et al.* (2015), used equivalent ionospheric currents deduced from ground magnetometer observations and Themis observations in addition to an MHD model to find the magnetospheric footpoints of observed ionospheric vortices. Their results showed a counter clockwise rotating vortex in the dawn sector, associated with the MI^- phase, however the origins of PI^- phase remained unclear.

In this chapter, a sudden solar wind dynamic pressure decrease was investigated using global MHD and I-T models as well as spacecraft and ground magnetometer observations. The purpose of this study is to investigate the magnetospheric and ionospheric sources for the PI^- and MI^- signatures, study the polarity distribution of the ground magnetometer responses to SI^-s, identify the ionospheric regions which are most prone to SI^- events and understand how the ionosphere and thermosphere systems are affected in these regions.

5.2 Methodology

5.2.1 Simulation Setup

The 11 June 2017 event was chosen as a case study to investigate the solar wind dynamic pressure decrements and their effects on the geospace system response. Similar to the 17 March 2015 case study, the ionospheric electrodynamics were simulated through a coupled GM-IM-IE simulation. The solar wind and IMF data were taken from the OMNI Database. The input parameters are shown in Figure 5.1.

Since the drivers for the simulation were taken from the OMNI Database, the simulation times were shifted by 7 minutes, which was roughly the time for the solar wind to propagate from 32 R_E, the outer boundary of the simulation domain, to the

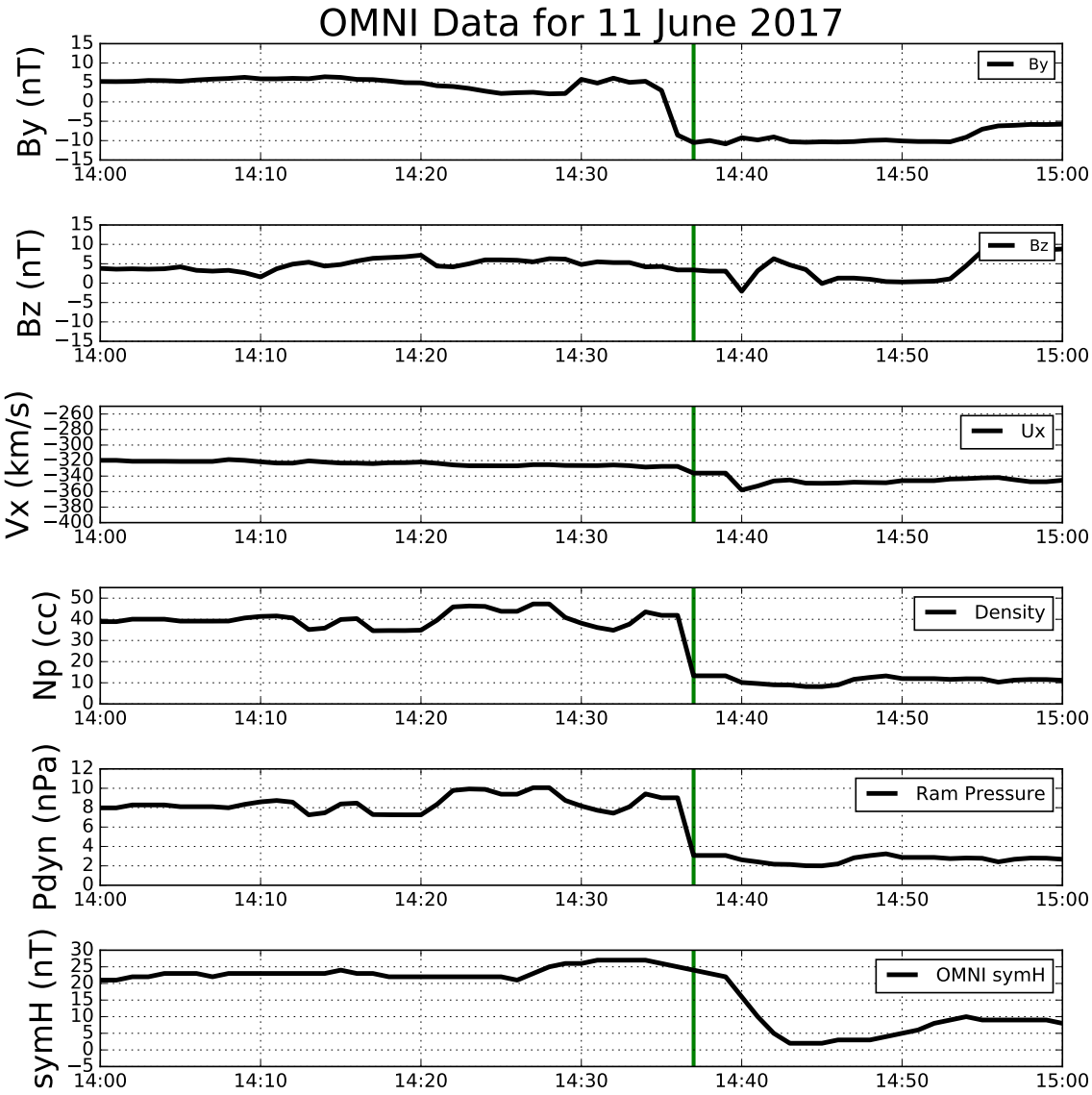

Figure 5.1: The input values used for IMF B_Y, B_Z, solar wind plasma parameters V_X and n_p are shown as well as the dynamic pressure and the sym-H index taken from the OMNI Database between 1400 UT to 1500 UT. The solid green line shows the time of dynamic pressure drop.

Earth with the solar wind speed. Figure 5.2 shows the IMF and solar wind parameters extracted at the subsolar point, x=17 R_E. The green line shows the arrival of the solar wind dynamic pressure drop at the nose of the magnetopause (10 R_E), the red line shows the arrival of the dynamic pressure drop at the Earth. The IMF B_Y was very close to 0 during the event, turning negative at 1438 UT and then positive at 1439 UT. The IMF B_Z was northward and did not show any strong variations during the interval. The change in solar wind velocity was around 20 km/s, during the event with no significant perturbations. The solar wind density dropped from 42 $\#/cm^3$ to 10 $\#/cm^3$. The solar wind dynamic pressure dropped from 4 nPa to 1nPa. The sym-H index dropped from 25 nT to 0 due to dynamic pressure decrease.

Similar to the previous case study, the GM inner boundary was set to 2.5 R_E from the center of the Earth. The computational domain was a three-dimensional box in geocentric solar magnetospheric coordinates that started from 32 R_E upstream of the Earth in the X direction to 224 R_E tailward and -128 R_E to +128 R_E both in the Y and Z directions. The finest resolution was 1/8 R_E grid close to the Earth. 600 virtual ground magnetometers were implemented in each hemisphere uniformly from the magnetic equator up to 80° latitude (4° in latitude by 12° in longitude).

The GITM simulations were driven with OMNI data from 9 June 2017 1400 UT to 11 June 2017 1400 UT. The Weimer *Weimer* (2005) empirical model was used for convection, while the Ovation aurora model *Newell et al.* (2002) was used for particle precipitation during this interval. The particle precipitation and electric field solutions obtained from the global MHD model were then used to drive the GITM simulations starting from 11 June 2017 1400 UT and onwards to 1700 UT, updating the electrodynamic patterns every 10 seconds. The GITM simulations were run with a spatial resolution of 4° in longitude and 1° in latitude for an altitude range between 100 and 600 km.

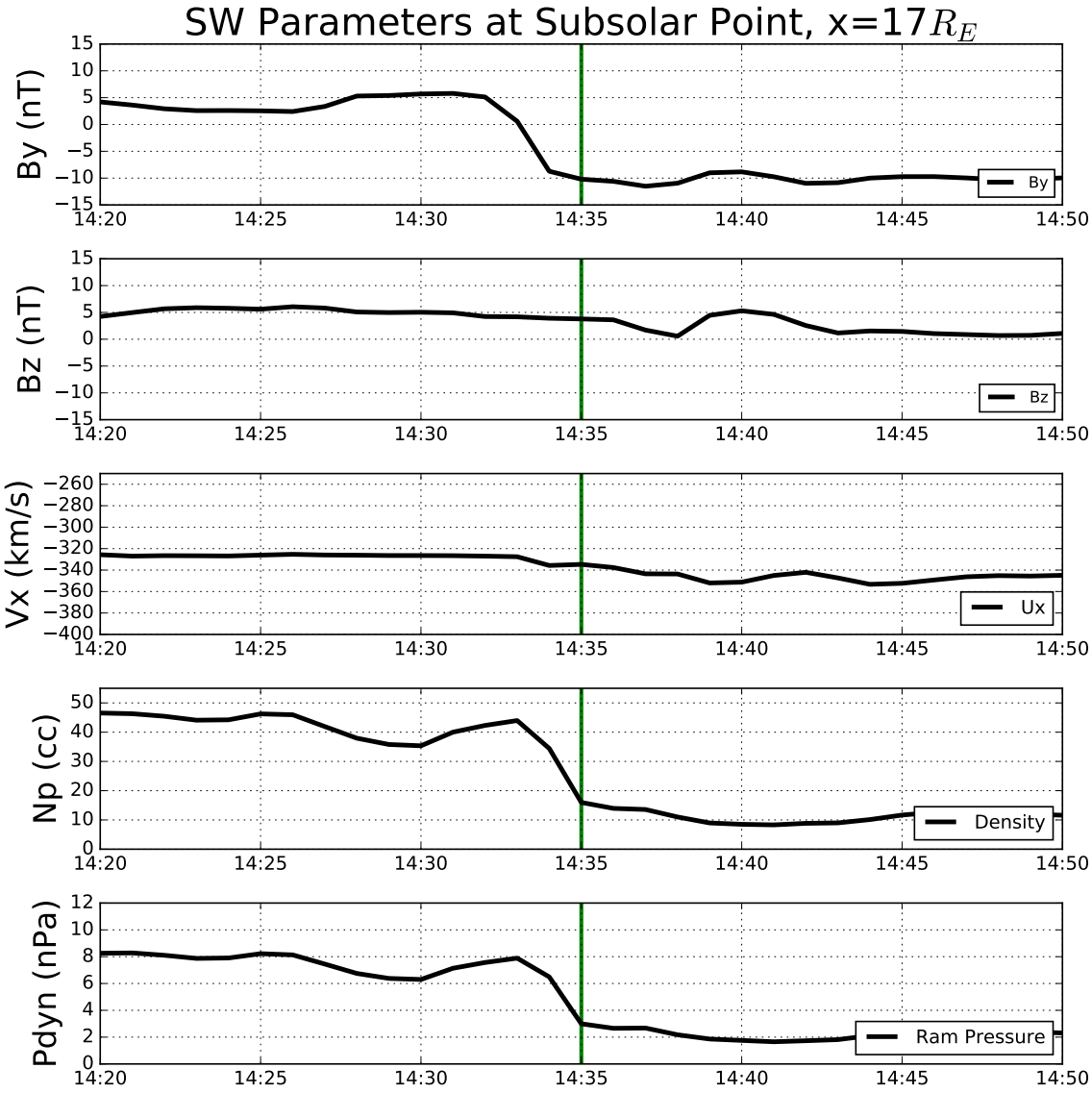

Figure 5.2: The simulated IMF B_Y, B_Z, solar wind V_X. N_P and P_{dyn} values extracted from the subsolar point at 17 R_E are shown between 1430 UT to 1500 UT. The solid green line shows the time of the pressure drop.

5.2.2 Spacecraft Positions

The locations of the THEMIS-D and MMS-1 spacecraft are shown in Figure 5.3. THEMIS-D was located in dayside dusk sector [3.4, 10.7, -2.1 R_E], very close to the magnetopause before decompression. MMS-1 was located in the tail dawn sector [-22.4, -9.9, 5 R_E] during the event. The ESA instrument from THEMIS-D was used to understand the magnetospheric flows at this location whereas the FGM instrument from MMS-1 was used to understand the propagation of the decompression front.

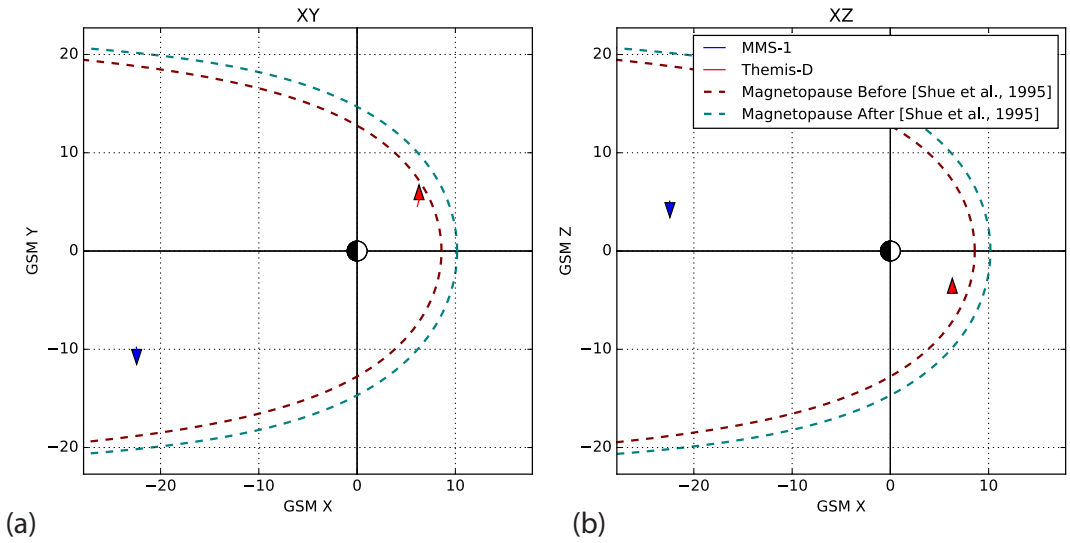

Figure 5.3: The positions of MMS-1 (blue) and THEMIS-D (red) spacecraft are shown in GSM XY (a) and XZ (b) coordinates. The magenta dashed lines show the magnetopause boundary calculated with the Shue model, based on the IMF and solar wind values before the dynamic pressure drop. The teal dashed lines show the magnetopause boundary after the dynamic pressure drop.

5.3 Results

5.3.1 Magnetospheric Response

Figure 5.4 shows the evolution of the global magnetosphere system. The equatorial flow profile can be seen on the right with the solar wind and magnetosheath flow vectors shown as green colors that corresponded to speeds above 200 km/s. There were two channels of sunward flows located at dawn and dusk just before the decompression.

At 1438 UT, shown in Figure 5.4b, the nose of the magnetopause started to expand. This resulted in two flow vortices at the dayside magnetosphere, one having a clockwise sense of rotation in the dawn sector and the other having a counter clockwise sense of rotation in the dusk sector. These vortices will be referred to as PI^- vortices from here on. There were also significant sunward flows at the subsolar magnetopause. Figure 5.5 shows the continuation of the evolution of the magnetospheric topology during the event. The top panels show the low density region in the solar wind which propagated towards the tail, corresponding to 1440 UT. A new pair of flow vortices emerged with opposite senses of rotation to their predecessor counterparts at dawn and dusk. Both pairs of vortices emerged inside the dayside magnetopause and propagated towards the nightside, eventually dissipating around 1450 UT (Figure 5.5c). These vortices will be referred to as MI^- vortices from here on.

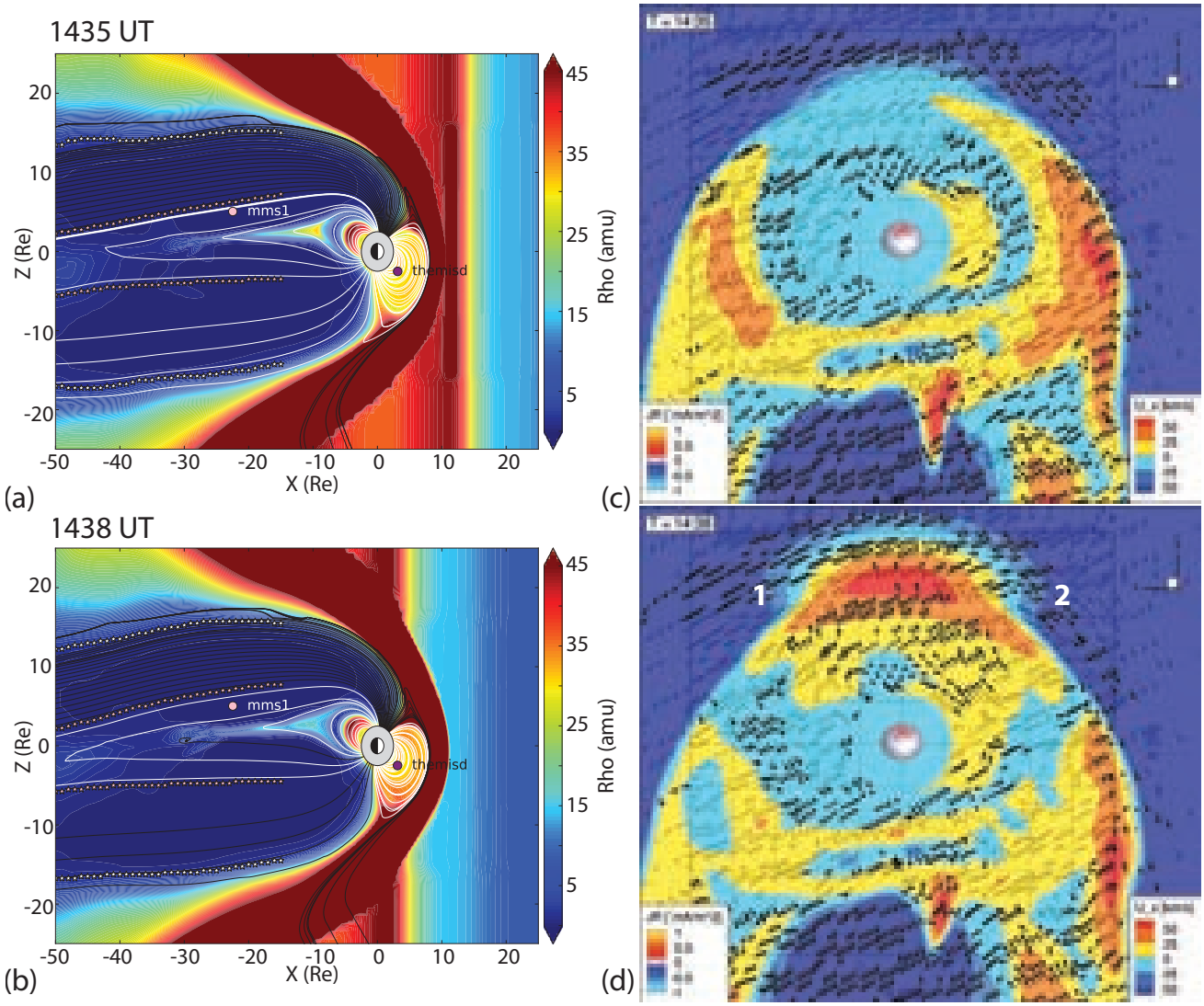

Figure 5.4: The pressure contours in the XZ plane with open (black) and closed (white) magnetic field lines are shown on the left for 1435 UT (a), 1438 UT (b). The purple dot shows the location of THEMIS-D, whereas the pink dot shows the location of MMS-1. On the right, contours of V_X are plotted with magnetospheric flow vectors. The blue (red) lines show the magnetic field lines centered at the flow vortices that carry downward (upward) FACs at 1438 UT.

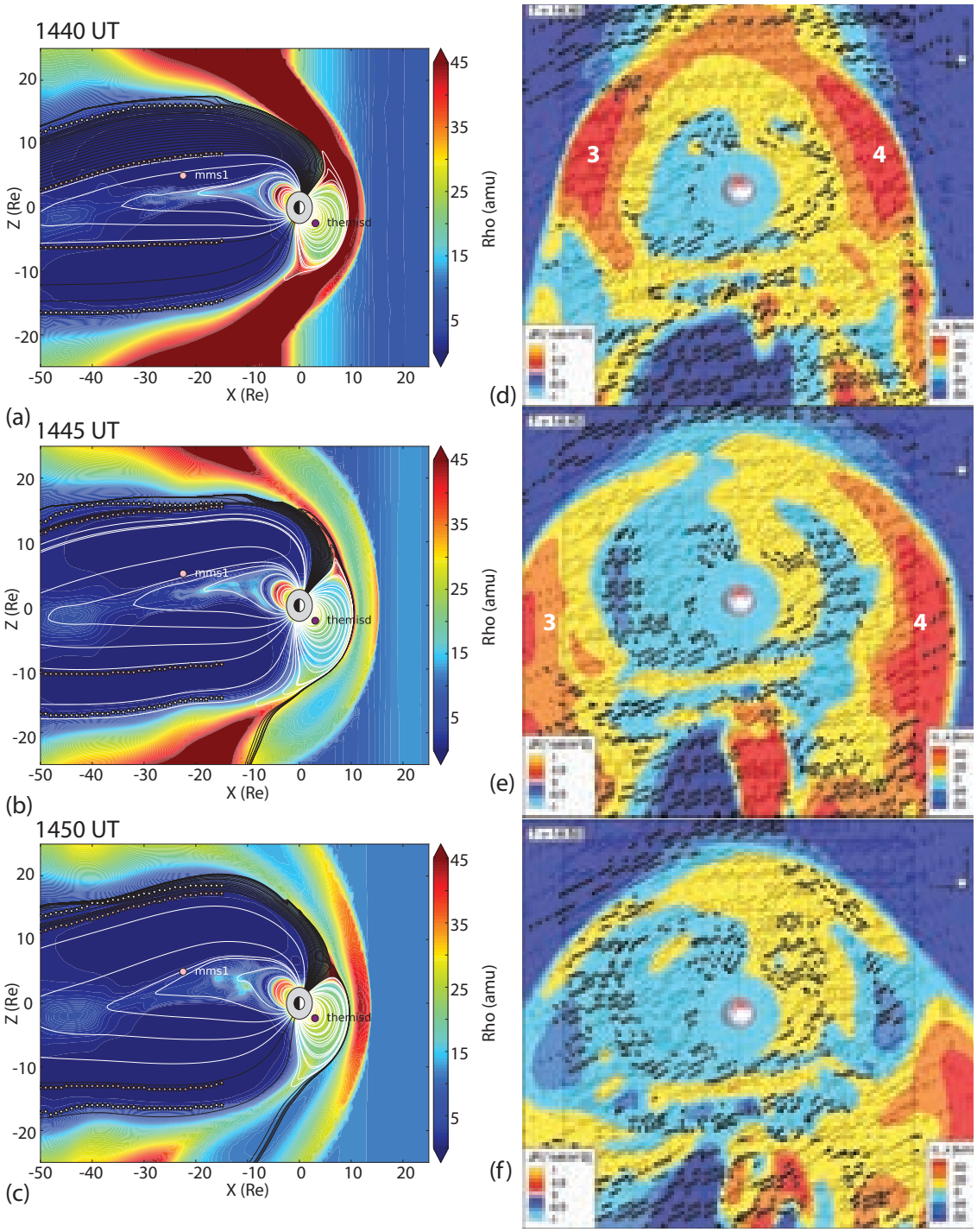

Figure 5.5: The pressure contours in the XZ plane with open (black) and closed (white) magnetic field lines are shown on the left for 1440 UT (a), 1445 UT (b) and 1450 UT (c). The purple dot shows the location of THEMIS-D, whereas the pink dot shows the location of MMS-1. On the right, contours of V_X are plotted with magnetospheric flow vectors. The blue (red) lines show the magnetic field lines centered at the flow vortices that carry downward (upward) FACs at 1440 UT.

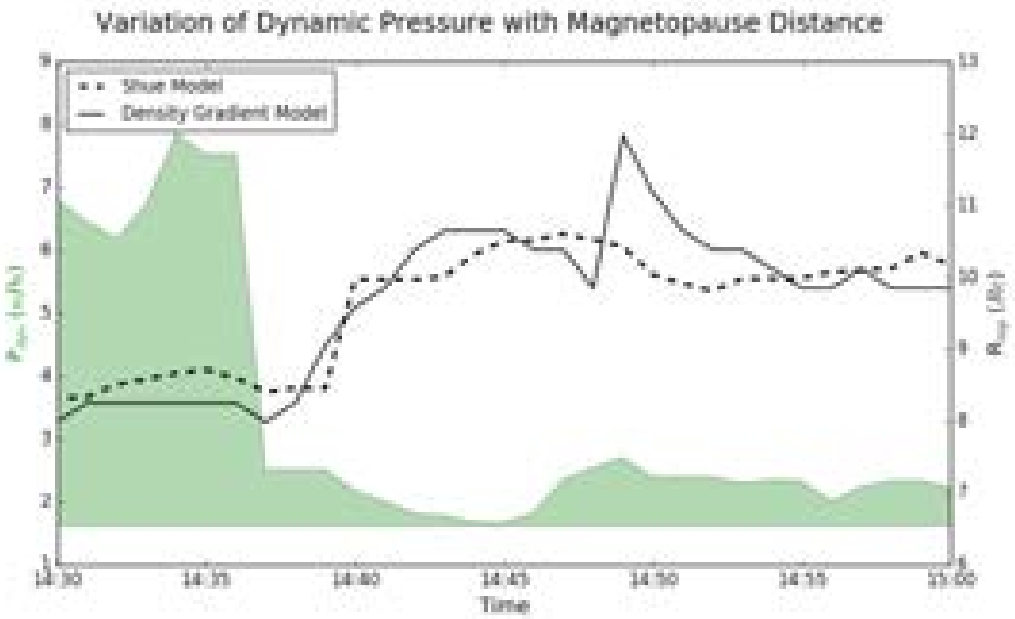

Figure 5.6: The variation of the magnetopause distance calculated with the Shue model (dashed) and density gradient (solid) with the solar wind dynamic pressure in between 1430 UT to 1500 UT are shown.

The evolution of the magnetopause location at the subsolar point was also investigated during this time interval as shown in Figure 5.6. The magnetopause location was calculated using the Shue model driven by the OMNI data, as well as the simulated magnetopause location calculated with the density gradient method described in *Garcia and Hughes* (2007). At 1437 UT, the dynamic pressure dropped from 7.5 nPa to 2.4 nPa, at this instance the Shue model showed the magnetopause location increased from $8R_E$ to $10R_E$. The simulation results showed an expansion from $8R_E$ to $10.5R_E$ at this instance in agreement with the Shue model.

Figure 5.7 shows the THEMIS-D ESA (left) and MMS-1 FGM (right) observations (bottom) compared with the simulated satellite measurements (top). THEMIS-D was recording tailward flows in the dusk sector, however as the magnetosphere started to expand, the flows became sunwards. The V_Y component was mostly positive both in simulations and the observations with mild intervals of negative values before 1455

UT. These flow variations indicated that a series of flow perturbations were recorded in the dusk sector first with a sense of counter clockwise then with a sense of clockwise rotation.

The MMS-1 FGM measurements presented in Figure 5.7b show the propagation of the perturbation to the tail. Considering the dipole structure of the Earth's magnetic field, a decompression indicates that B_X should decrease, whereas the B_Z component should increase. The behaviour was very clear in the MMS-1 observations, marking the time of arrival as 1450 UT. The time of arrival and the drop of B_X was well captured with the simulation. One explanation for not capturing the behaviour of B_Z is that MMS-1 in the simulations was further away from the current sheet than observations indicate.

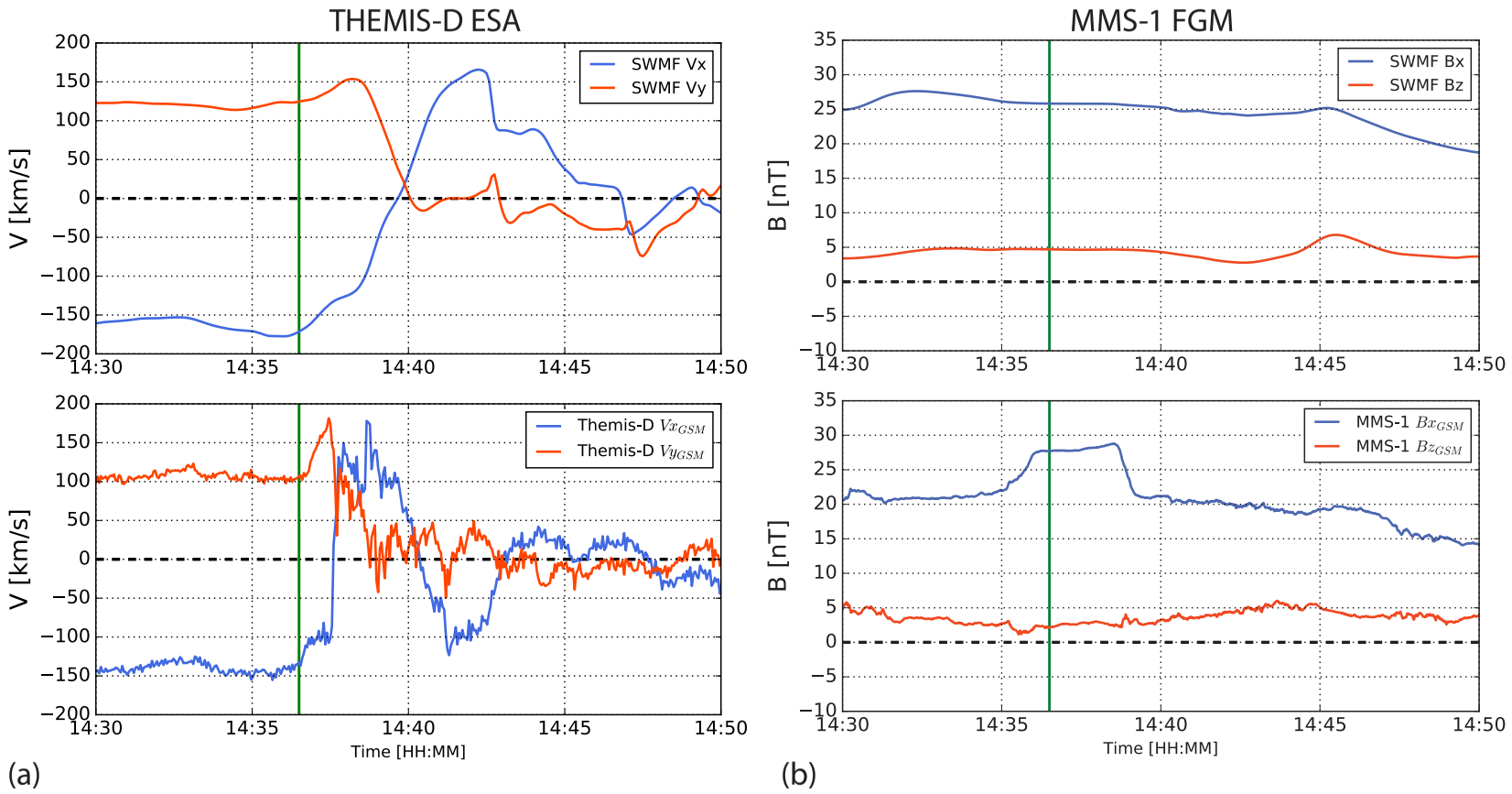

Figure 5.7: The comparison of satellite measurements (bottom panels) and simulated satellite responses (top panels) for THEMIS-D ESA (left) velocity measurements and MMS-1 FGM (right) magnetic field measurements are shown between 1430 UT-1500 UT. The red line shows the y component and the blue line shows the x component of the velocity on the left. On the right, the blue line shows the x, the red line shows the z component of the magnetic field vector.

5.3.2 Ionospheric Response

The behaviour of the FACs, transient FACs, the Joule heating and the ground magnetometer profiles were studied in more detail to understand the ionospheric response to magnetospheric expansion. These profiles are shown in Figure 5.8 at the same time instances as the magnetospheric snapshots shown in Figures 5.4 and 5.5. Due to the IMF B_Z being north, the FAC profile resembled the NBZ current system closely before the magnetospheric expansion started. Figure 5.8b shows the response 1 minute after the expansion started. The overall FAC profile did not change significantly, however the perturbation FAC systems, which were obtained by subtracting the FAC profile from the previous minute, showed an upward FAC on dusk and a downward FAC on dawn, consistent with the magnetospheric flow vortices. The Joule heating profile shown in the third row of Figure 5.8b, displayed a weakening in the dusk region. The magnetic field perturbations at the ground, shown in the fourth row of Figure 5.8b, indicated a positive perturbation (green contours) at low latitudes between 3 to 14 MLTs, at middle latitudes between 12 to 15 MLTs, and at the high-latitude midnight sector. At the same time instance, the high latitude northward magnetic response at the dawn sector was negative.

Figure 5.8c shows the perturbed profiles at 1440 UT. The electric field potential contours have enlarged, indicating the expansion of the magnetosphere. At this time the perturbation FACs shown inthe second row had different directions to those at the PI^- phase. These MI^- FACs were upward in the dawn and downward in the dusk sectors. The PI^- FACs had moved tailward at this instance. The Joule heating profile in the third row had weakened but extended further equatorward and there was a clear dawn-dusk asymmetry with dawn sector having more heating. The ground magnetic perturbations also showed a clear dawn-dusk asymmetry in this instance. The virtual magnetometers recorded a positive perturbation in the mid-latitudes between 4-13 MLT. The response was negative everywhere else, with two strong peaks, one in the

high-latitude dawn sector and one in midnight sector.

At 1445 UT, the FAC profile started to differ from the earlier stages, as shown in Figure 5.8d. The electric field potentials became denser in the dusk sector, whereas PI^- and MI^- FACs started to disappear. The Joule heating became stronger in the dusk sector. The ground magnetic perturbations were negative with the exception of the high-latitude region located between 6-13 MLT. The negative perturbation peaked at the high-latitude pre-noon sector.

At 1450 UT, the dayside FAC profile did not show significant perturbations, however the electric field potentials in the nightside, especially in dusk region, were denser. The transient currents showed the closure currents for the MI^- FACs with opposite directions. The Joule heating in the dawn side significantly weakened, but strengthened in the dusk sector, corresponding to stronger electric field regions. Overall, the ground magnetic perturbation profile was very similar to that at 1445 UT, with a stronger negative dip in the mid-latitude region between 6-14 MLT, a stronger positive peak in the high-latitude region at the same local time sector, and a stronger negative dip in the high-latitude region between 18-06 MLTs.

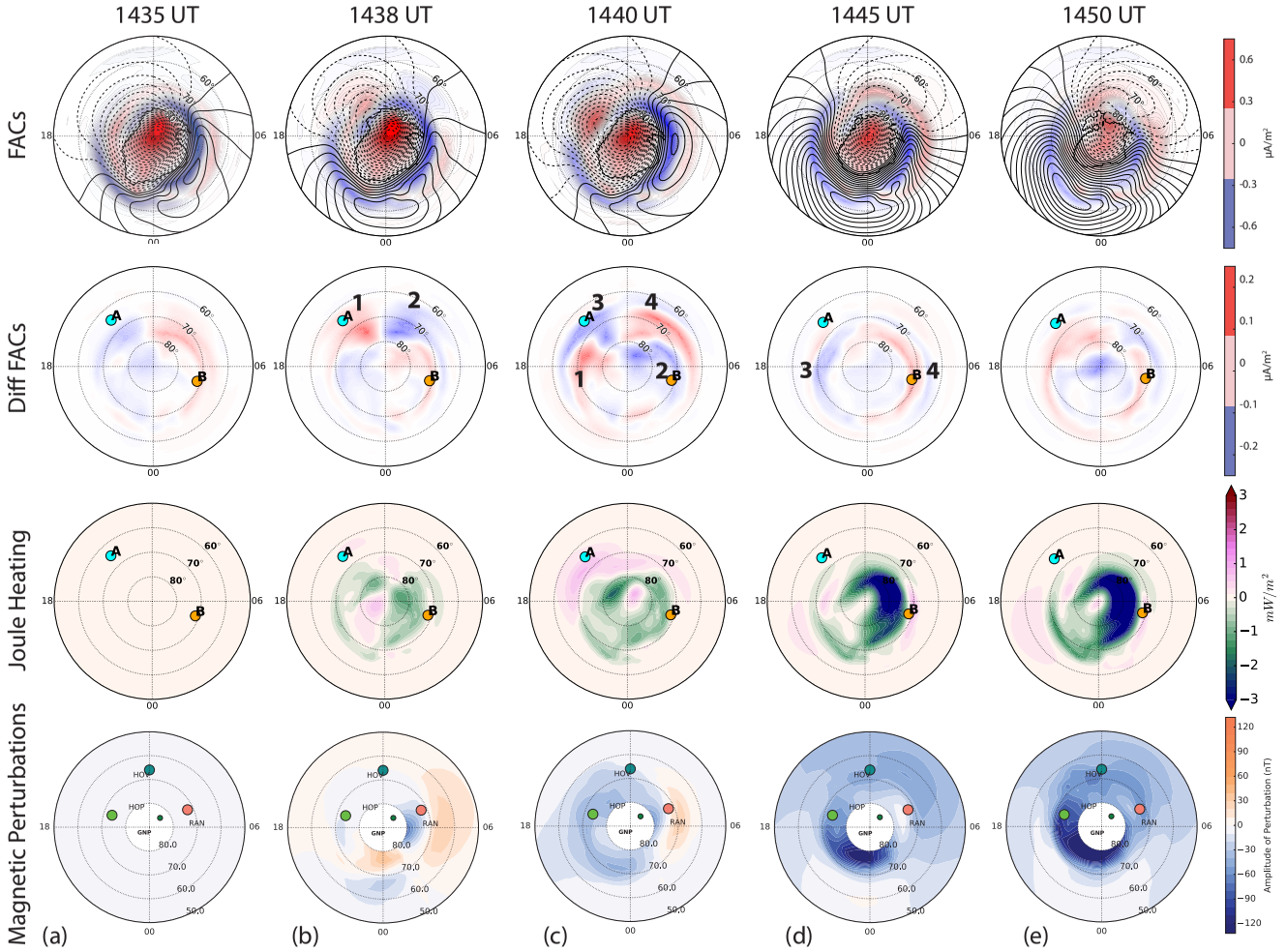

Figure 5.8: The FACs, perturbation FACs, Joule heating profile and the simulated ground magnetometer responses to the solar wind dynamic pressure drop are shown for 1435 UT (a), 1438 UT (b), 1440 UT (c), 1445 UT (d) and 1450 UT (e). The green, blue and pink dots in the bottom panels show the locations of the HOP, HOV and RAN magnetometers.

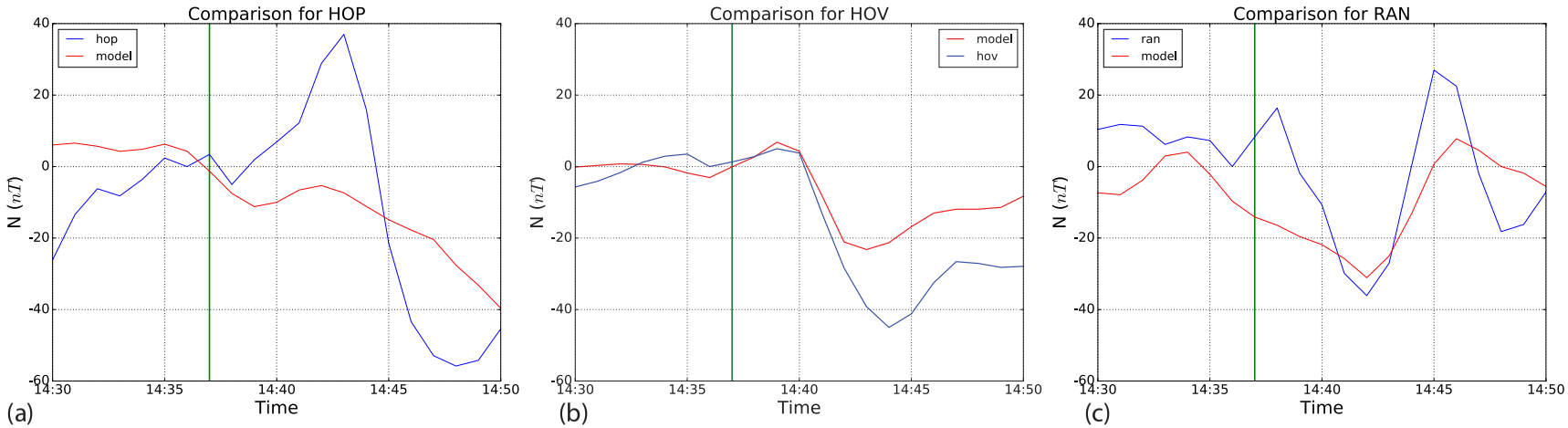

Figure 5.9: The comparison of the simulated magnetometer responses (red) with HOP (a), HOV (b) and RAN (c) magnetometers (blue) are shown in between 1430 UT-1500 UT. The solid green line shows the response to solar wind dynamic pressure drop.

Three magnetometer measurements were compared with the simulated magnetometer measurements to assess the simulation results. The locations of these magnetometers are shown in Figure 5.8 in the bottom row. The magnetometers were chosen to sample the behaviour at the high-latitude dawn, dusk and low-latitude dayside regions. The comparison of the observations with the simulations results are shown in Figure 5.9. The Hopen Island (HOP) magnetometer, located in the dusk sector at the time, recorded an enhancement followed by a drop in the N component of the magnetic field. This behaviour was well captured by the virtual magnetometer, indicating the presence of an upward perturbation FAC, followed by a downward FAC. The Faroe Island (HOV) magnetometer recorded a drop in the magnetic field, which was also captured by the model. At lower latitudes, the expected response to an expansion is a drop in the overall magnetic perturbation due to the variation in the Chapman-Ferraro currents. The Rankin Inlet (RAN) magnetometer located in the dawn sector recorded a drop followed by an enhancement in the magnetic field. The response of the virtual magnetometers to the magnetospheric expansion was well captured, however they underestimated the magnitude of the perturbations.

Figure 5.11 shows the ion convection, temperature and electron temperature variations from the GITM simulations, as a response to the sudden expansion of the magnetosphere. Figure 5.10a shows that the ion temperatures were below 1000 K before the event, with the exception of 10-14 LT, where a relatively strong westward ion convection was seen and the ion temperatures exceeded 2500 K. The electron density was depleted in this region. The meridional cut taken at 11 LT, shows the ion temperature peaked at 79° latitude, and around 300 km altitude. 1 minute after the start of the magnetospheric expansion, the ions started cooling and convecting eastward at noon. The drop in the ion temperature was around 1000 K at 300 km in the 11 LT cut. At 1440 and 1445 UT, the ions still convected eastward at noon and the temperature profiles stayed similar to that of 1438 UT. Figure 5.10e shows

the profiles at 1450 UT. At this time ions started convection westward again, heating the ions in the region back to 2500 K. The meridional cut showed that the peak ion temperature reached 2400 K at the same latitude but at a lower altitude around 180 km.

Figure 5.11 shows the vertical ion temperature, electron temperature and density profiles extracted from 78° latitude at the 11 LT. Before expansion the peak ion temperature was 2700 K at 300 km. At 1438 UT, the ion temperature dropped around 1600 K and the peak ion temperature was 1200 K at 210 km. The ion temperature did not change drastically until 1450 UT, at which, the temperature was enhanced but it was still lower than the initial profile at 1435 UT. The peak of the ion temperature was located at 200 km, and it was around 2300 K.

The electron density and temperature profiles are shown in Figure 5.10b, however there were no significant changes in both profiles except a mild drop followed by a recovery. The most significant variation can be seen in the electron density profile above 240 km, where the final electron density dropped by 10 %.

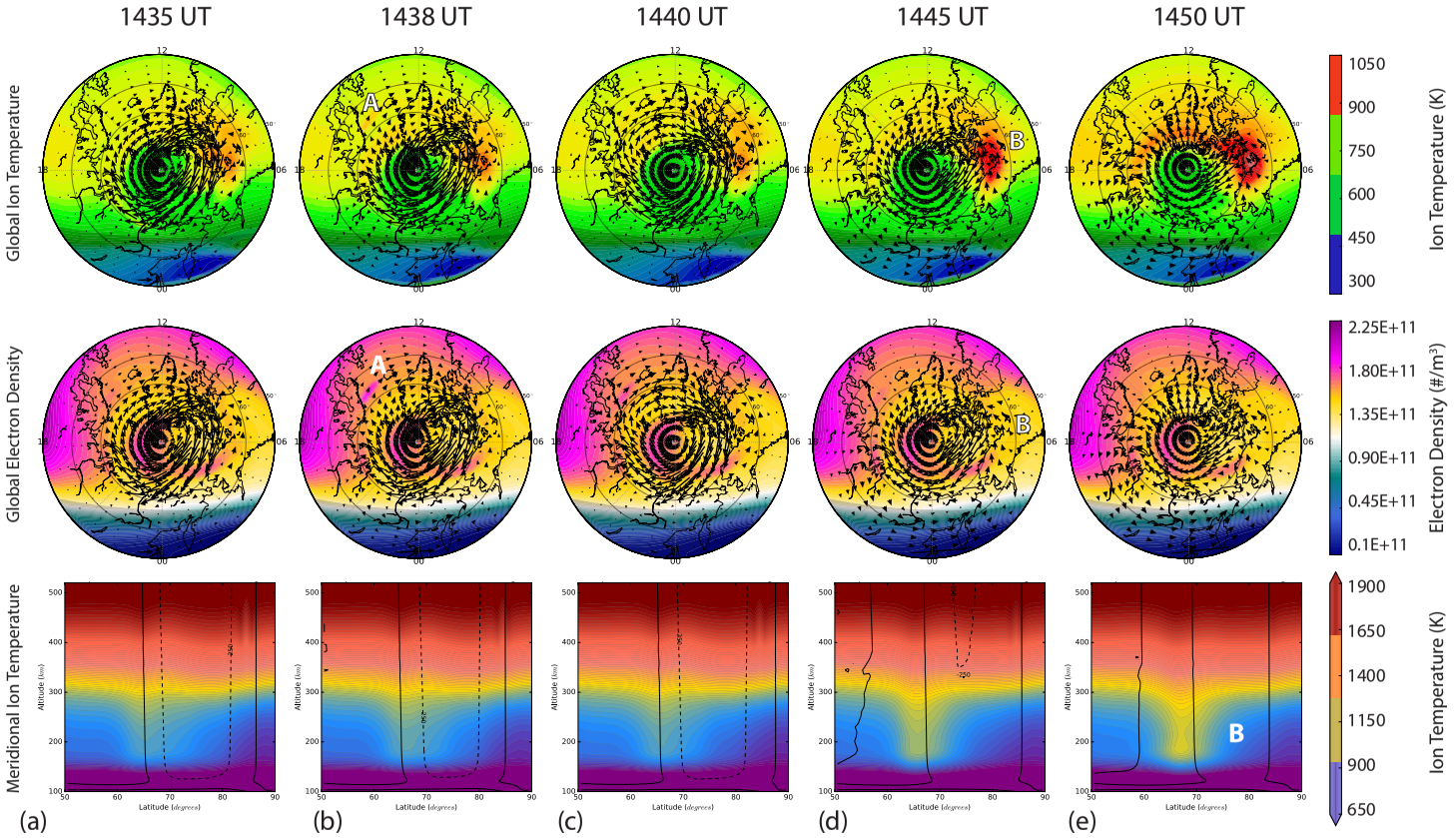

Figure 5.10: The GITM results for ion temperature and convection profiles at 210 km (top) and electron density (middle) are shown for 1435 UT (a), 1438 UT (b), 1440 UT (c), 1445 UT (d) and 1450 UT (e). The bottom panel shows the ion temperature for a meridional cut taken between 50° and 90° latitude at 11 LT, with horizontal ion convection velocities plotted on top for the same time steps.

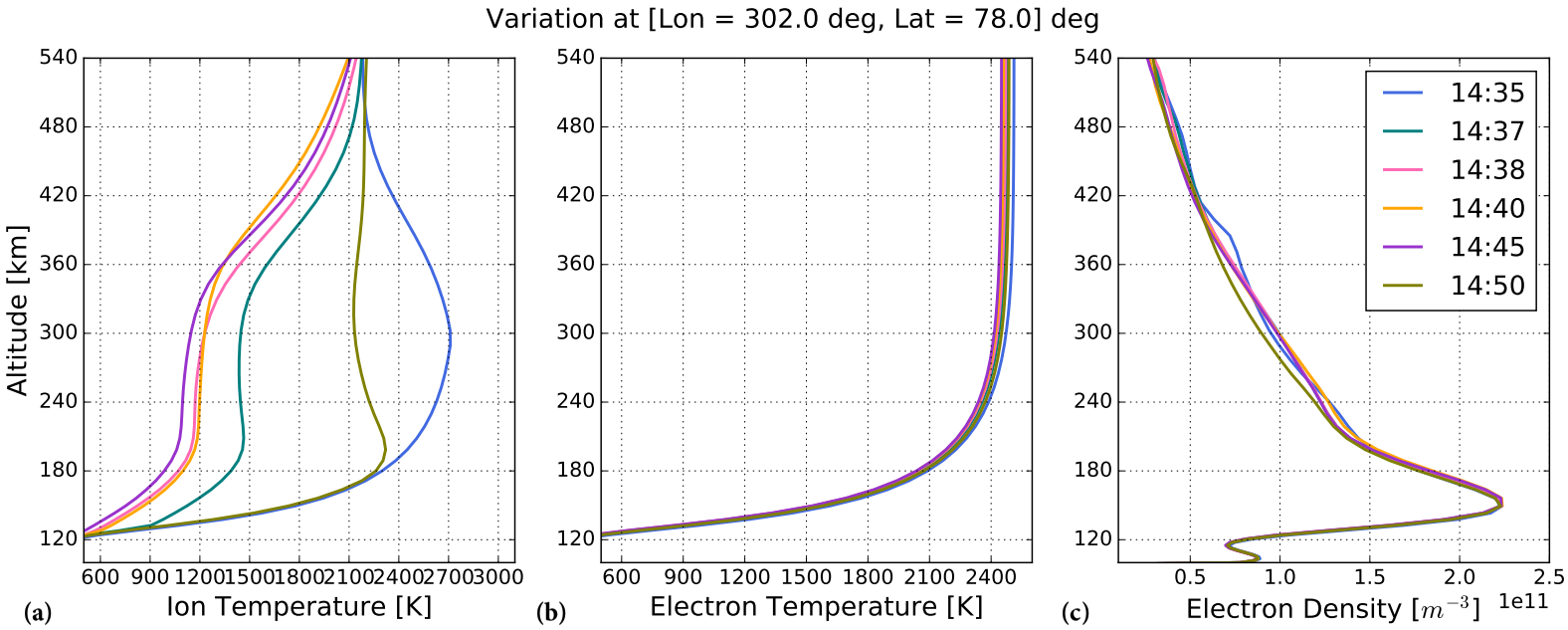

Figure 5.11: The altitude profiles (110-540 km) at 11 LT, 78° for ion temperature (a), electron temperature (b) and electron density (c) taken at 1435 UT (blue), 1437 (dark green), 1438 UT (pink), 1440 UT (orange), 1445 UT (purple) and 1450 UT (light green) are shown.

5.4 Discussion

With the help of global and physics based simulations, the response of the geospace system to a sudden solar wind dynamic pressure event has been investigated. During the expansion of the magnetosphere, the simulated magnetospheric flows showed interesting features, especially during the PI^- phase. One of the most comprehensive studies investigating the magnetospheric response to SI^-s was conducted by *Zhao et al.* (2015). They have reported Themis-A observations of a counter clockwise rotating vortex in the dawn sector, and reproduced an oppositely rotating dawn-dusk vortex pair with MHD simulations corresponding to the same time interval. However, this study showed that PI^- vortices exist in the magnetosphere and their existence could be verified with THEMIS-D observations of the velocity on the dusk. Furthermore, the ground magnetometers also indicated vortical structures through bipolarity changes. The PI^- vortices indicated an upward perturbation FAC in the dusk sector and a downward perturbation FAC in the dawn sector as shown in Figures 5.4 and 5.8. These FACs were responsible for the positive magnetic field perturbation in dusk and the negative magnetic field perturbation in the dawn sectors. Simulations reported in *Fujita et al.* (2005), also showed sunward flows during the PI^- phase, but the partial vortex profile [*Fujita et al.* (2005)] was not fully described.

The magnetic field perturbations on the ground, derived by virtual magnetometers, showed only slight deviations from the Araki model of SI^-s [*Araki and Nagano* (1988)]. The PI^- phase showed an enhancement in the low-latitude dawn sector and high-latitude noon and midnight sectors. The MI^- signature was mostly negative with strong dips at low-latitude noon and high-latitude midnight sectors. One exception to the overall negative trend was seen at the high-latitude noon sector, but with lower magnitudes than that of the negative dips. These differences from the Araki model can be attributed to the large magnetic dipole tilt in June and to the mostly positive but fluctuating IMF B_Y values.

The pre-existing NBZ current system had an upward FAC cell at the high-latitude dusk and mid-latitude dawn and a downward FAC at the high-latitude dawn and mid-latitude dusk at 1430 UT. During the PI^- phase, the electric field potentials in the dusk sector weakened, while those in the dawn sector remained unchanged. During the MI^- phase, both cells had weakened but the dusk cell had intensified on the nightside. This behaviour was reflected in the Joule heating in the ionosphere.

One of the most important missing links in understanding the geospace system response to solar wind dynamic pressure drops, was due to the lack of studies on the I-T system. By driving GITM with electric potentials that exhibit the behaviour of the magnetospheric expansion, this study showed the effects of the dynamic pressure drops on the ionosphere system. There was a significant drop in the ionospheric temperature at noon that exceeded 1000 K, but little response was seen in the electron temperature, density or the neutral temperature. Overall, the neutral temperature dropped by around 40 K above 326 km, however it later increased by about 30 K by 1445 UT. Similarly, after the decompression, the ion temperature was restored with slightly lower temperatures in the F_2 region.

This case study of the solar wind dynamic pressure decrease on 11 June 2017 revealed interesting magnetospheric flow profiles that were not evident in previous studies. Although this case was very useful in understanding the global response to solar wind dynamic pressure, it also showed the necessity of idealized simulations which can eliminate the asymmetries that occur due to the drivers of the system, such as the IMF, as well as intrinsic parameters like dipole tilt.

5.5 Summary and Conclusions

The findings of this study can be summarized as follows:

1. A pair of dawn-dusk vortices appear on the dayside as a response to magne-

tospheric expansion. These PI^- vortices have a clockwise sense of rotation on the dusk, and a counter clockwise sense of rotation on the dawn sector.

2. Another pair of dawn-dusk vortices follow the PI^- vortices. These MI^- vortices have a counter clockwise sense of rotation on the dusk and a clockwise sense of rotation of the dawn sector.

3. These vortices mapped to the ionosphere as PI^- (downward on dawn and upward on dusk) and MI^- (upward on dawn and downward on dusk) FACs.

4. The Joule heating on the noon sector decreased as a result of ionospheric electric field potential contours enlarging with magnetospheric expansion.

5. The ion temperature dropped by around 1500 K in the noon sector, which was in between PI^- and MI^- FACs. Around 15 minutes later it increased by around 800 K. On the contrary, the electron temperature, density and the neutral temperatures were not significantly affected by the magnetospheric expansion.

6. The polarity distribution of the magnetic field perturbations at the ground level slightly deviated from the SI^- model of Araki *Araki* (1994a), which is a mirror image of the SI^+, but this deviation is attributed to variations in the IMF drivers and the dipole tilt.

CHAPTER VI

The Geospace System Responses to Idealized Sudden Solar Wind Dynamic Pressure Increase and Decrease

6.1 Introduction

The sudden decreases in the solar wind dynamic pressure are associated with various magnetospheric activity, like ultra low frequency (ULF) waves [*Motoba et al.* (2003), *Zhang et al.* (2010), *Shen et al.* (2016)] auroral intensity enhancements [*N.Sato et al.* (2001), *Liou* (2007), *Belakhovsky and Vorobjev* (2016)] and even substorms [*N.Sato et al.* (2001)]. However the exact mechanisms behind the sudden expansion of the magnetosphere, the magnetospheric and ionospheric sources for the two-step response observed as the decompression signature [*Takeuchi et al.* (2000)], the global polarity distribution of the magnetic field perturbations on the ground [*Araki and Nagano* (1988), *Takeuchi et al.* (2002)] and the altitudinal changes in the I-T system [*Zhao et al.* (2015)] have not been well understood.

The geospace system response is significantly affected by the dipole tilt, IMF, and solar wind drivers, making idealized studies a necessity to parse out effects of each of those driving parameters. In this chapter, the global magnetospheric and ionospheric evolutions of the geospace system during SI^+s and SI^-s are investigated through

idealized simulations to minimize influence from other sources. In addition one strong event and one weak event have been designed for SI^+ and SI^- comparisons between strong and weak compression and decompression are presented to further investigate the role that solar wind density changes play in perturbing the geospace system.

6.2 Methodology

Similar to previous studies, the simulation outer boundary was set to +32 to -224 R_E in X, -128 to +128 R_E in Y and Z GSM coordinates. The GM/BATS-R-US, IM/RCM and IE/RIM components were used. A grid resolution of 1° in latitude by 1° longitude in MLT coordinates was picked for the IE module. Likewise, the 10 second high resolution output from IE was used in driving the GITM model. The virtual ground magnetometer chain consisted of 600 uniformly distributed points in MLT coordinates for each hemisphere. To understand the geospace system response and how it differs between a SI^+ and a SI^-, four cases of idealized simulations were conducted, one weak and one strong compression, as well as a weak and a strong decompression.

6.2.1 Simulation Setup for Compression

The solar wind and IMF drivers for the weak and strong compression cases are shown in Figure 6.1a and b respectively. The top panel shows the IMF B_Y, which equals zero, and the second panel shows the IMF B_Z, which was set to 5 nT. The IMF B_X, not shown, was set to 0 nT. The solar wind velocity was set to -320 km/s, which was a nominal speed for the slow solar wind. The solar wind velocity stayed constant throughout the simulation to inhibit electric field variations due to solar wind velocity variations. The compression was initiated by an enhancement in the solar wind density, shown in the fourth panels of both Figures 6.1a and b. The initial solar wind density was 10 cm^{-3}, which was increased to 30 cm^{-3} at 1430 UT for the

weak compression. This perturbation arrived at the Earth 7 minutes later at 1437 UT. The corresponding solar wind dynamic pressure increased from 1 nPa to 2.5 nPa, resulting in an overall solar wind dynamic pressure ratio, P_2/P_1 of 2.5. For the strong compression, the initial solar wind density was 5 $\#/cm^3$, which was increased to 50 $\#/cm^3$ at 1430 UT and similar to the weak compression arrived at the Earth at 1437 UT. The dynamic pressure was 0.5 nPa and as a result of density enhancement was increased to 4.2 nPa, with an overall P_2/P_1 ratio of 8.4.

The values before 1400 UT were used to drive the GITM simulations for both cases with the *Weimer* (2005) electric field potentials and the ovation aurora model [*Newell et al.* (2002)] for particle precipitation for a 2 day period, to allow the model to converge. These drivers were updated every minute. The initialization simulations ended at 14.00 UT and the drivers were then switched to the 10 second output from the MHD model.

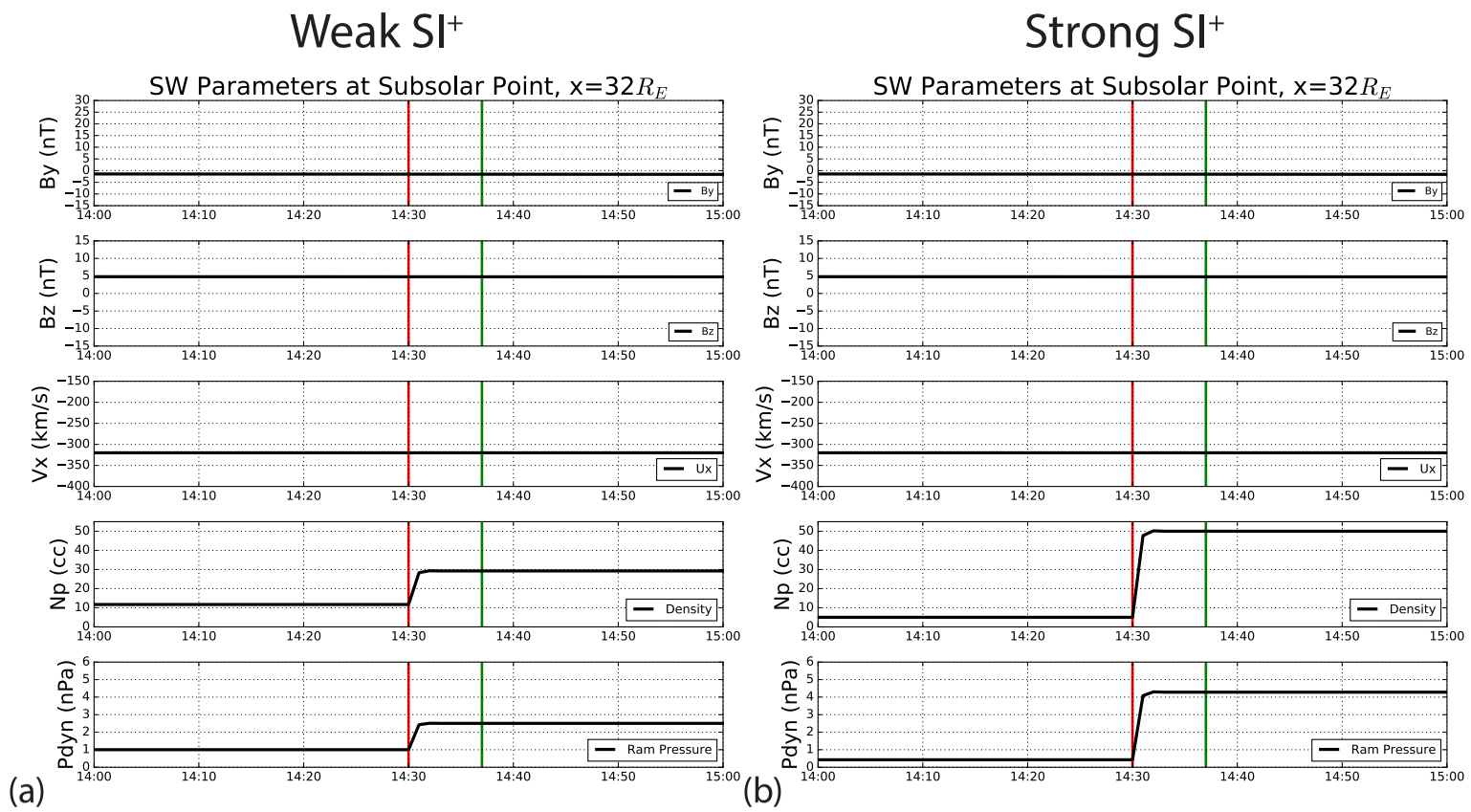

Figure 6.1: The IMF B_Y, B_Z, solar wind V_X, N_P and P_{dyn} values used to drive the weak SI^+ and the strong SI^+ simulations are shown in between 1400 UT to 1500 UT. The red line shows the time when the perturbation was at the outer boundary and the green line shows the arrival of the disturbance to the Earth.

6.2.2 Simulation Setup for Decompression

The solar wind and IMF drivers for the weak and strong decompression cases are shown in Figure 6.2a and b respectively. The IMF drivers were the same as the compression cases, with IMF B_X and B_Y being zero, and B_Z being set to 5 nT, while the solar wind speed was constant at -320 km/s. The solar wind dynamic pressure drop was again initiated at 1430 UT, with a drop in density for both cases. For the weak SI^-, the solar wind density was 30 $\#/cm^3$, which dropped to 10 $\#/cm^3$. The dynamic pressure was 2.4 nPa and dropped to 0.5 nPa, resulting in an overall P_2/P_1 of 0.4. For the strong SI^-, the solar wind density was 50 $\#/cm^3$, which dropped to 5 $\#/cm^3$ at 1430 UT. The dynamic pressure dropped from 4.2 nPa to 0.5 nPa, with an overall P_2/P_1 ratio of 0.12.

Similar to the compression simulations, the GITM simulations were driven with the values prior to 1400 UT with the *Weimer* (2005) electric field potentials and the ovation aurora model [*Newell et al.* (2002)] for particle precipitation for a 2 day period. At 1400 UT, the drivers for GITM were replaced with the global MHD solutions which had a 10 second temporal resolution.

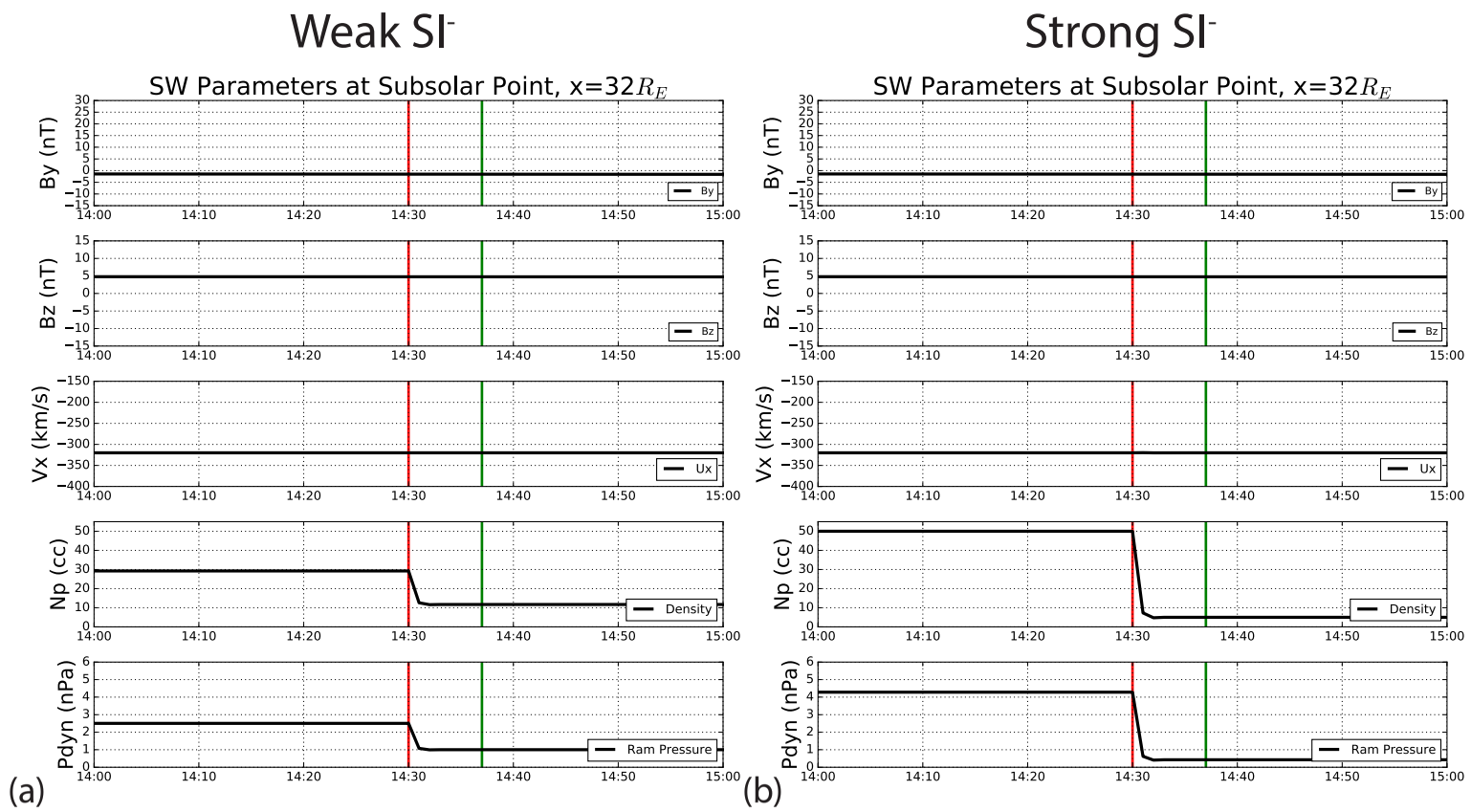

Figure 6.2: The IMF B_Y, B_Z, solar wind V_X, N_P and P_{dyn} values used to drive the weak SI^+ and the strong SI^- simulations are shown in between 1400 UT to 1500 UT. The red line shows the time when the perturbation was at the outer boundary and the green line shows the arrival of the disturbance to the Earth.

6.3 Comparison of Magnetospheric Responses to Strong Compression and Decompression Events

In this section, only the comparison of strong SI^+ and SI^- will be presented to understand the differences between compression and decompression events. Figure 6.3 shows the magnetospheric flow profiles in the equatorial region before the perturbation for the SI^+ and SI^- events respectively. The magnetospheric configuration shown in Figure 6.3a had a magnetopause standoff distance of 10 R_E due to the weaker solar wind pressure, whereas the magnetopause standoff distance was 8 R_E in Figure 6.3b due to the larger pressure. The co-rotational flows extended up to a radius of 8 R_E on the left and up to 6 R_E on the right when the magnetosphere was compressed. Both magnetospheric configurations showed sunward flows in the outer portions of the magnetosphere. Some elongated vortex like structures were also present in both configurations. One such vortex can be seen in the dayside dawn sector with a counter clock-wise sense of rotation, starting at [9, -1] R_E and extending to [3,-7] R_E in Figure 6.3a, whereas in Figure 6.3b it started at [9,-2] R_E and extended to [5,-4] R_E. The vortex system had a larger spatial scale in Figure 6.3a compared to the compressed case. Another vortex can be seen at dusk towards the nightside with a clock-wise sense of rotation. The dusk vortex in Figure 6.3a had a partial structure, starting at [7,5] R_E and extending towards [-3,8] R_E. Similarly, the dusk vortex in Figure 6.3b started at [5,1] R_E and extended to [-5,5] R_E. There were additional vortex systems on the nightside, however their examination is beyond the scope of this work.

Figure 6.4 shows the preliminary impulse responses of the SI^+ (a-c) and SI^- (d-f). The flow profiles 1 minute prior (1436 UT) to the perturbation arrival resembled the quiet time profiles in Figure 6.3a and b closely. When the compression front arrived at the nose of the magnetopause, as shown in Figure 6.4b, the sunward flows in the dayside magnetosphere ([8,-2] R_E and [8,4] R_E) were replaced with anti-sunward

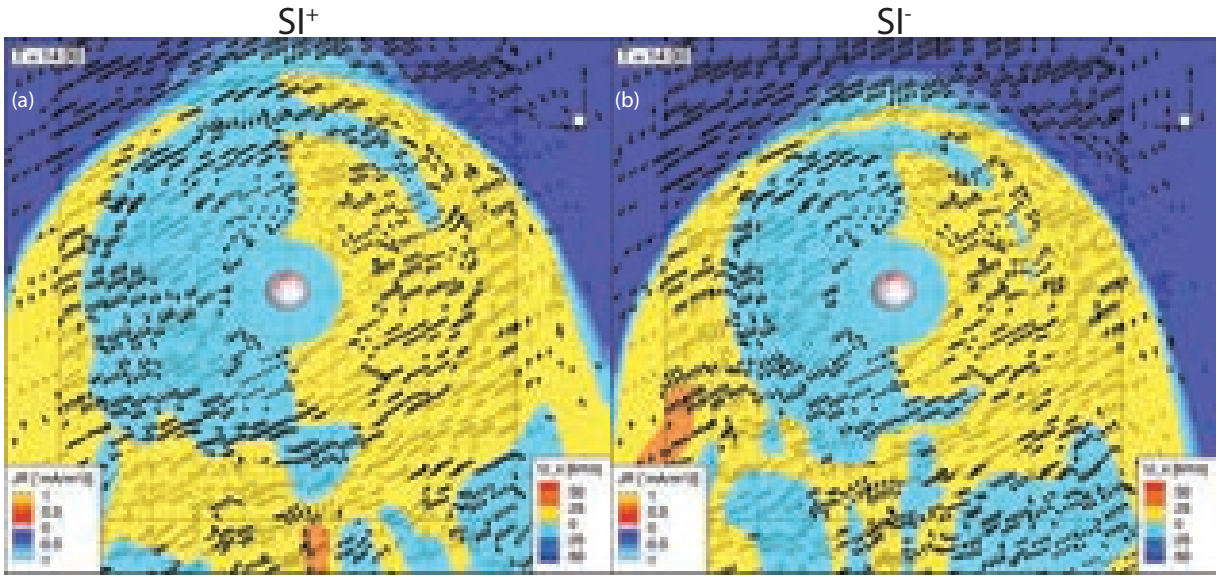

Figure 6.3: The comparison of the magnetospheric flow profiles at the equatorial plane before the dynamic pressure increase (a) and decrease (b) events. The contours show the x component of the velocity, arrows show the flow vectors, and the contours on the top of the Earth shows the radial current projections (red/upward; blue/downward).

flows, shrinking the size of the pre-existing vortex. The curl of the dusk vortex at the dayside magnetosphere was also enhanced due the compression of the nose. Figure 6.4c shows one minute after the arrival of the compression front. Both the dawn and dusk vortices have shrunk and their start points were offset to [4,-7] R_E and [3,9] R_E respectively, due to the propagation with the solar wind.

The flow profile in Figure 6.4e shows the expansion of the magnetosphere as the decompression front arrives at the nose of the magnetopause. Sunward flows occurred in the dayside magnetosphere as a part of the expansion. The dusk vortex further shrinks, whereas the dawn vortex disappears in the next minute shown in Figure 6.4f. Two new partial vortices appeared as a result of fountain like expansion from the nose, with a counter clock-wise sense of rotation on dusk, and with a clock-wise sense of rotation at dawn. Both flow systems had larger spatial scales than the initial vortex systems.

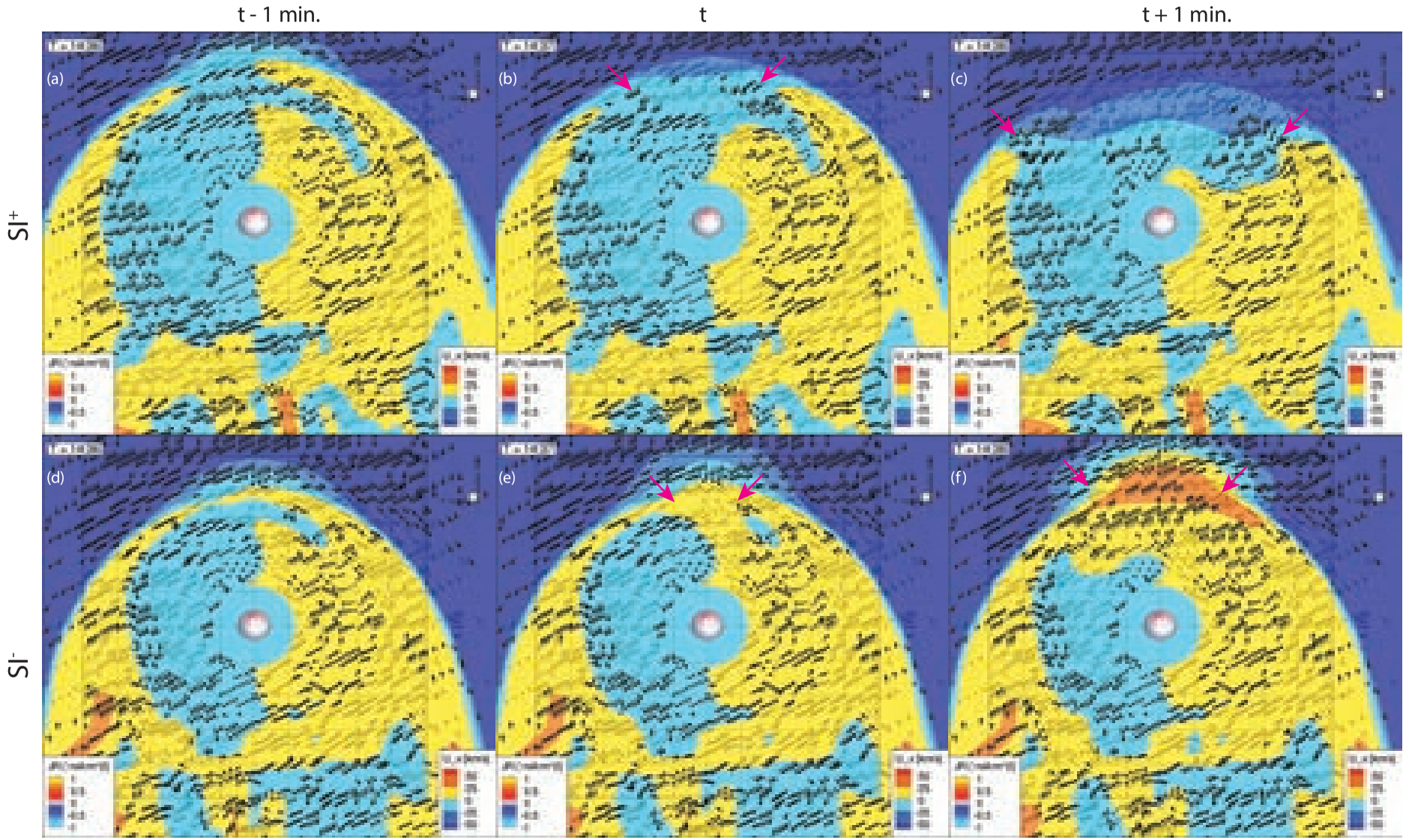

Figure 6.4: The equatorial magnetospheric flow profiles for SI^+ (a,b,c) and SI^- (d,e,f) taken at 1 minute prior to the perturbation (a,d), at the time of arrival (b,e) and 1 minute after the arrival of the perturbation (c,f). Pink arrows highlight the most significant flow profile changes.

The main impulse response of the SI^+ (a-c) and SI^- (d-f) are shown in Figure 6.5. The previous PI^+ vortex systems propagated towards the nightside at X=-2 R_E as indicated in Figure 6.4a. On the dayside a new vortex system started to form, with a counter clock-wise sense of rotation in the dusk sector and with a clock-wise sense of rotation in the dawn sector. This new vortex system (shown with pink arrows), associated with the MI^+ phase became more evident in Figure 6.4b, with the dawn vortex centered at [4,-6] R_E and the dusk vortex centered at [4,6] R_E. 5 minutes after the arrival of the compression front, these new vortices had further propagated towards the nightside, with centers at [1.8, -7] R_E and [1.8,7] R_E respectively as shown in Figure 6.4c. The new magnetopause standoff distance was at 8 R_E, 5 minutes after the arrival of the compression front.

Figure 6.5d shows the start of the MI^- phase, with flows directed in the +y direction in the dusk and -y direction in the dawn sectors. The MI^- vortices appeared 4 minutes after the magnetosphere started to decompress, which is shown in Figure 6.5e (shown with purple arrows). The flow in the noon sector became tailward, completing the formation of vortices. The dawn vortex had a counter clock-wise sense of rotation, whereas the dusk vortex had a clock-wise sense of rotation. These vortices also propagated towards the nightside with the dawn vortex centered at [5,-6] R_E and dusk vortex centered at [5,6] R_E, shown in Figure 6.5f. The new magnetopause standoff distance was at 10 R_E, 5 minutes after the expansion started.

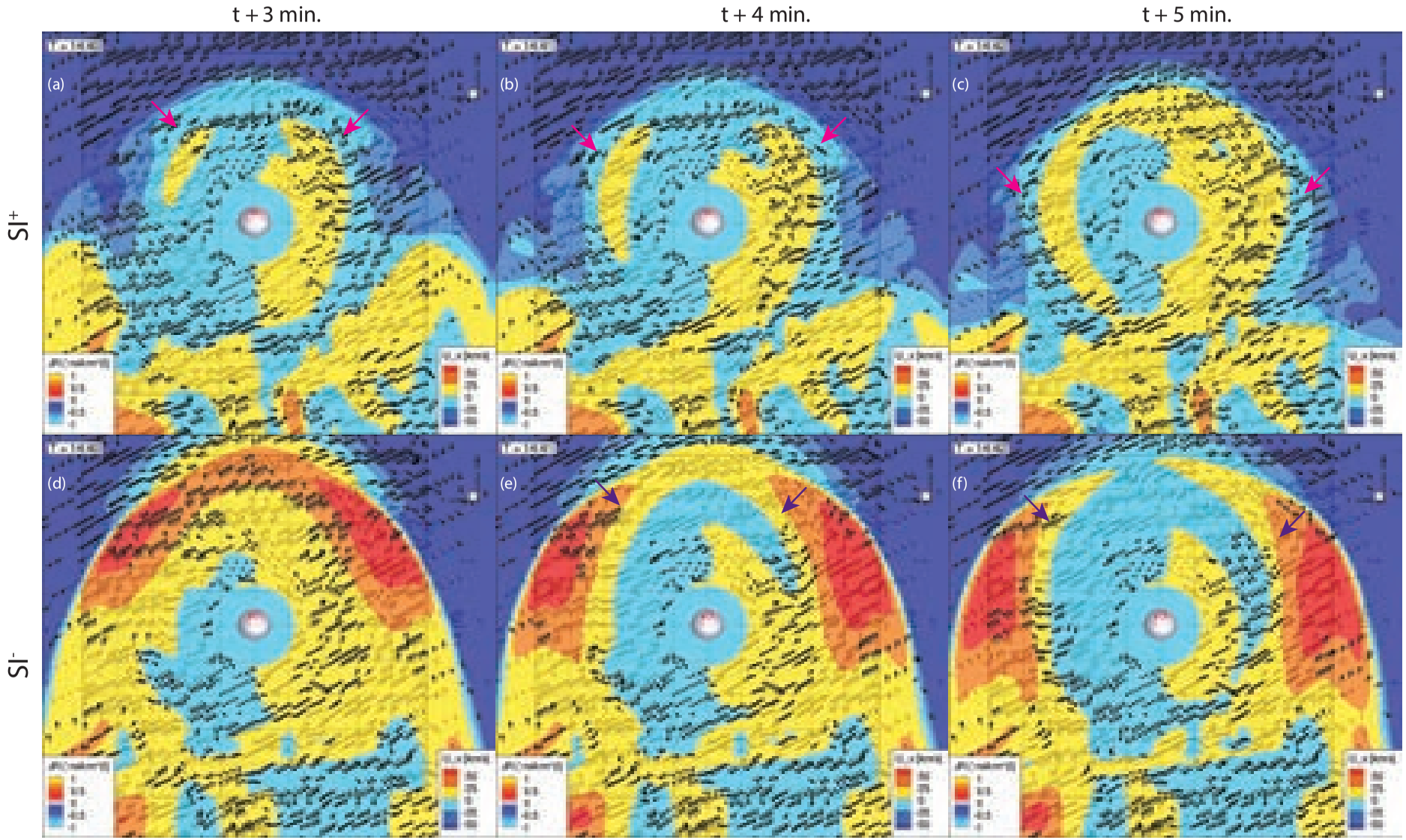

Figure 6.5: The equatorial magnetospheric flow profiles for SI^+ (a,b,c) and SI^- (d,e,f) taken at 3 (a,d), 4 (b,e) and 6 (c,f) minutes after the arrival of the perturbation. Pink and purple arrows highlight the most significant flow profile changes.

Figures 6.6 and 6.7 show the temporal evolution of V_X and V_Y extracted at [X,Y] = [4,-6] R_E (dawn) and [4,6] R_E (dusk) for SI^+ and SI^-. During the compression, both the dawn and dusk vortices had a negative x component, indicating tailward motion from 1437 to 1440 UT. Between 1440 UT and 1446 UT, the flows were sunward. In the dawn sector, V_y was positive, indicating that the magnetosphere was moving inwards, while it was mostly negative in the dusk sector, again showing an inward motion. The brief period when V_y turned positive at dusk indicates that the PI vortex was fully completed at this point.

During the decompression, both the dawn and dusk vortices had a sunward flow (+ V_x), between 1437 and 1443 UT. The flows became tailward between 1443 and 1449 UT in the dawn sector, and between 1443 and 1453 UT in the dusk sector. V_y was negative inn the dawn sector and positive in the dusk, indicating the expansion of the magnetosphere.

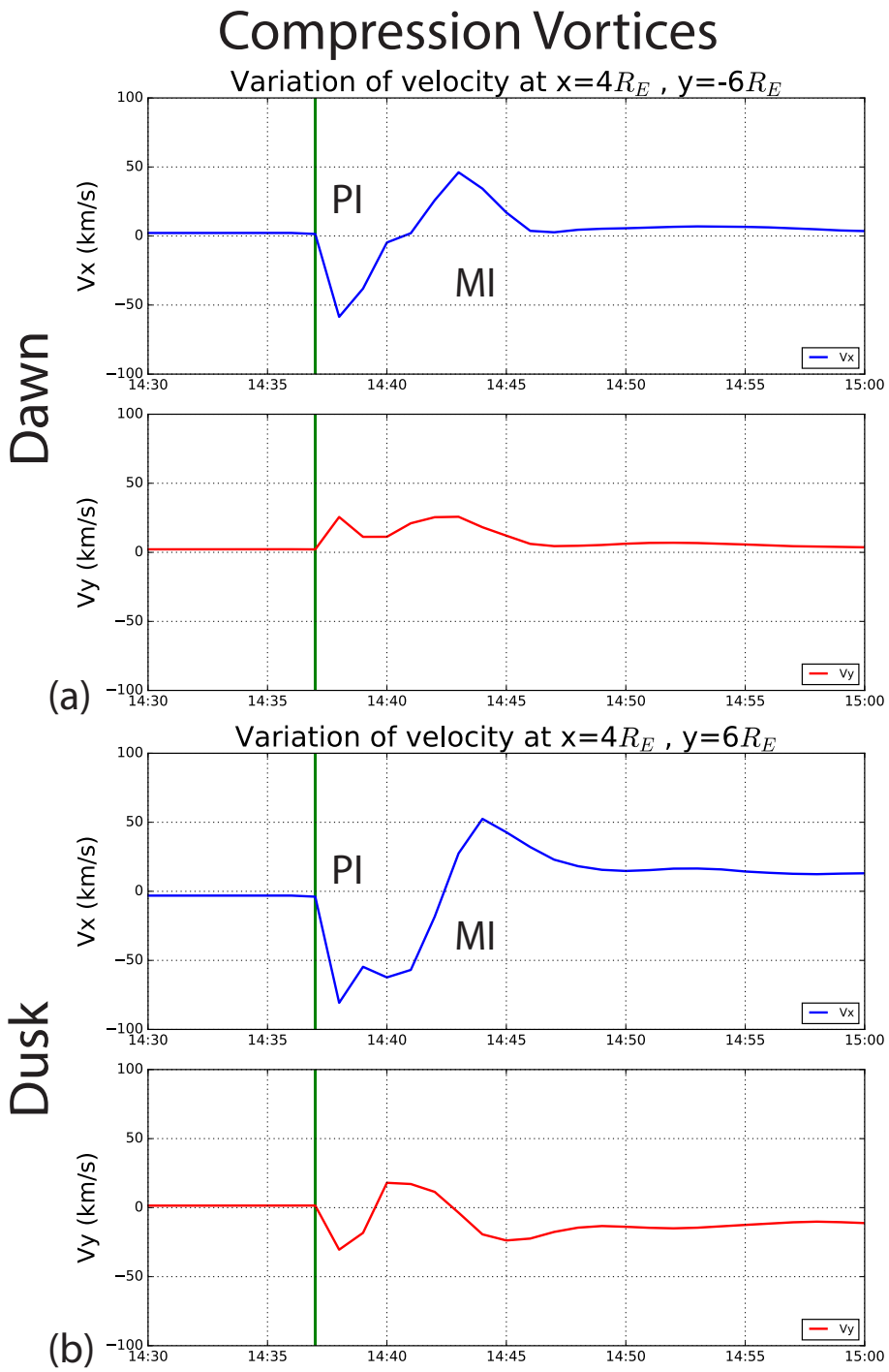

Figure 6.6: The x (blue) and y (red) components of the velocity at dawn (a) and dusk (b) sectors taken at $x = 4R_E$ are shown between 1430 UT to 1500 UT for the SI^+ event.

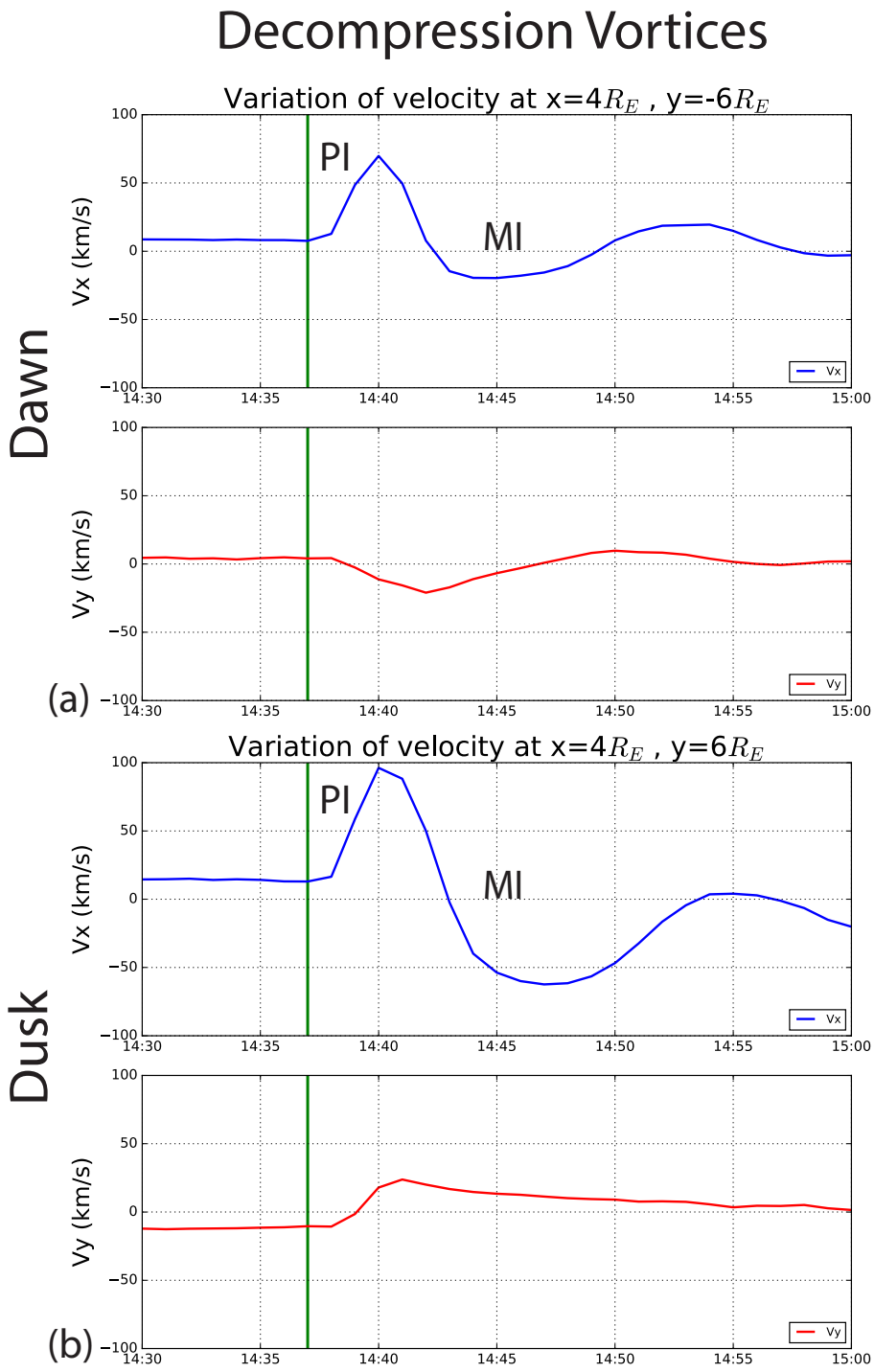

Figure 6.7: The x (blue) and y (red) components of the velocity at dawn (a) and dusk (b) sectors taken at $x = 4R_E$ are shown between 1430 UT to 1500 UT for the SI^- event.

If there was only one set of vortices, both compression and decompression signatures of the y component would have shown a sign reversal. Instead, the temporal evolution of the velocities at these locations indicates two sets of vortices passing back to back from the [4,-6] R_E and [4,6] R_E points.

Figure 6.8 shows the compression vortices in the dusk sector. The clock-wise rotating PI^+ vortex would form prior to the counter clock-wise rotating MI^+ vortex during the SI^+ event. A spacecraft passing through these vortices at points 1-2-3 (left) would observe the V_x (purple dots) and V_y (orange) shown on the right of Figure 6.8. At point 1, both the V_x and V_y components would be positive, measuring the outer edge of the PI^+ vortex. Point 2 would correspond to the inner edge of the PI^+ or the outer edge of the MI^+ vortices, regardless it would result in negative V_x and V_y measurements. At point 3, the spacecraft would be at the inner edge of the MI^+ vortex, which then would correspond to positive V_x and V_y measurements.

Figure 6.9 shows the decompression vortices in the dusk sector. The counter clock-wise rotating PI^- vortex would form prior to the clock-wise rotating MI^- vortex during the SI^- event. Similarly, a spacecraft passing through these vortices at points 1-2-3 (left) would observe the V_x (purple dots) and V_y (orange) shown on the right of Figure 6.9. At point 1, both the V_x and V_y components would be negative, measuring the outer edge of the PI^- vortex. Point 2 would correspond to the inner edge of the PI^- or the outer edge of the MI^- vortices, regardless it would result in positive V_x and V_y measurements. At point 3, the spacecraft would be at the inner edge of the MI^- vortex, which then would correspond to negative V_x and V_y measurements.

These schematics show how spacecraft measurements can be mistaken for a single vortex measurement since the start and end points would have same direction. It also helps explain the vortex signatures observed by Themis-D which were shown in Figure 5.8, implying that the observations show not one but two vortex systems with different senses of rotation which can explain how the two-step response was

generated in the magnetosphere.

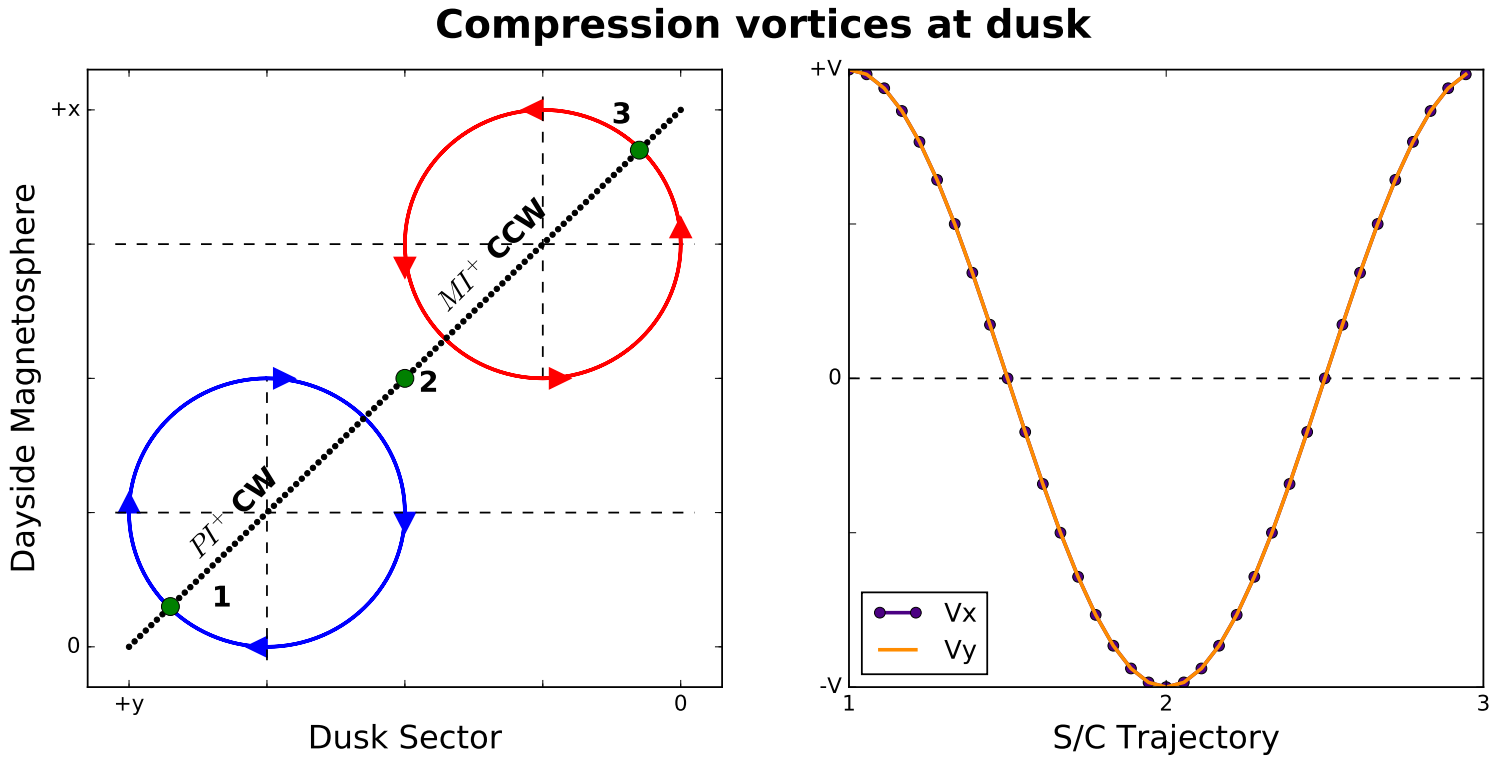

Figure 6.8: A diagram showing the passage of a spacecraft over the PI^+ (clock-wise) and MI^+ (counter clock-wise) vortices in the dusk sector during a compression event (left) and the Vx and Vy components it would measure along its trajectory (right).

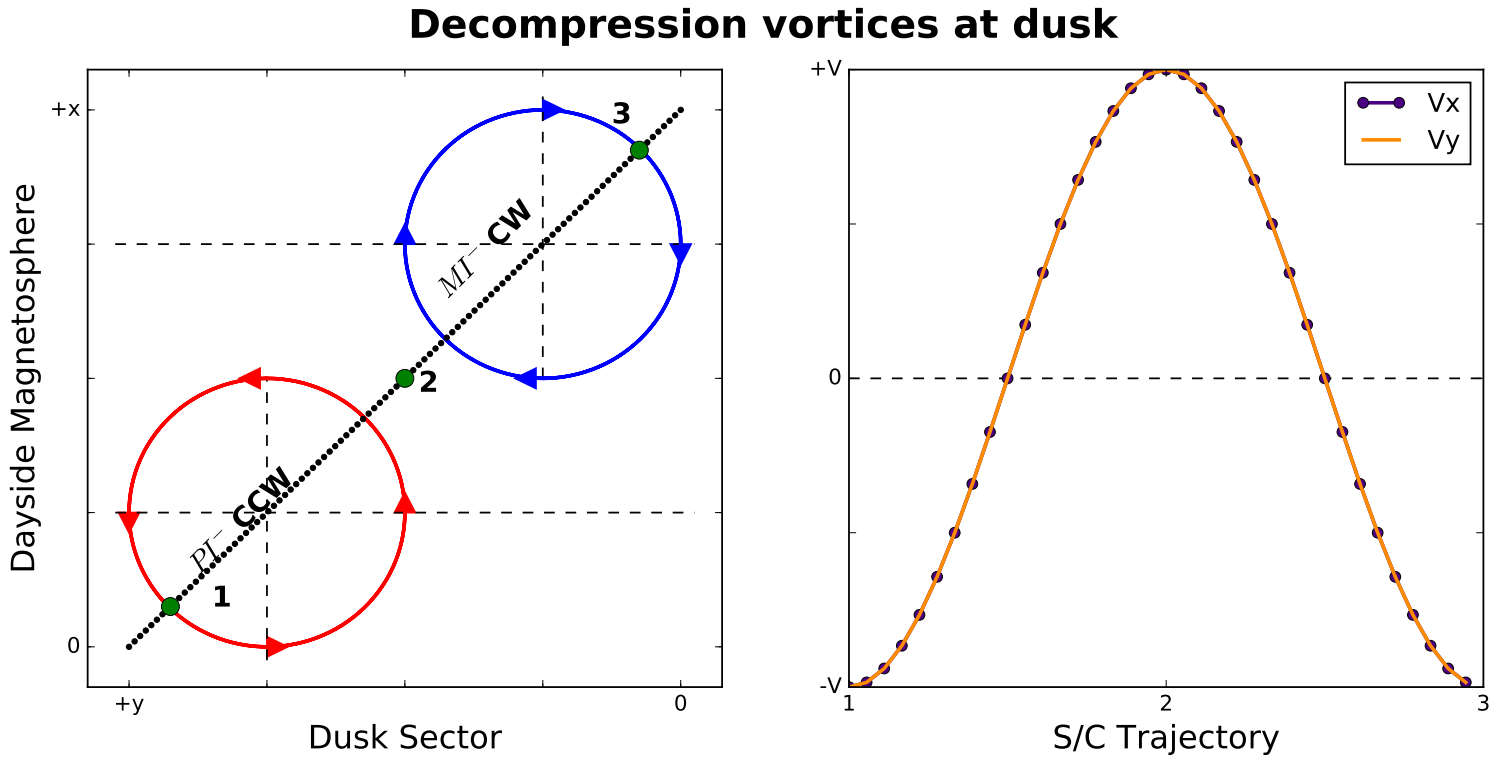

Figure 6.9: A diagram showing the passage of a spacecraft over the PI^- (counter clock-wise) and MI^- (clock-wise) vortices in the dusk sector during a decompression event (left) and the Vx and Vy components it would measure along its trajectory (right)

6.4 Comparison of Ionospheric Responses

To understand the differences in the ionospheric response to the compression and decompression, the FAC, Joule heating, ion convection, ion temperature and the N component of the magnetic perturbations at the ground are investigated. In addition a comparison between strong and weak events is also provided.

6.4.1 FAC Response

The evolution of the FACs for four different cases are show in Figure 6.10. Figure 6.10a shows the FAC profiles 7 minutes prior to the arrival of the solar wind perturbations, starting from the strong SI^+ and SI^-, followed by the weak SI^+ and SI^-. All four profiles showed the NBZ current system prior to the perturbation, with an upward FAC cell on dawn and a downward FAC cell on dusk at the high-latitudes and with an upward Region-1 sense FAC cell on dusk and a downward FAC cell on dawn at the lower-latitudes. The strengths of the FAC cells were similar with compressed configurations (second and fourth rows), having denser electric field potentials at the nightside.

The response to compression was immediate as shown in Figure 6.10b in the first and third rows. A new FAC with an upward cell on dawn and a downward cell on dusk appeared. The magnitude of the perturbation FACs for strong SI^+ were 0.2 $\mu A/m^2$ larger than that of the weak SI^+. The densest electric field potential line contours were in the noon sector for the strong SI^+, while the densest potential line contours were in the pre-midnight sector for the weak SI^+.

The response to the decompression was also prompt as shown in the second and fourth rows of the Figure 6.10b. The perturbation FACs had an upward direction at dusk and a downward direction at dawn. Similarly, the magnitude of the strong SI^- FACs were larger than that of the weak SI^- by 0.15 $\mu A/m^2$.

Two minutes after the arrival of the perturbation, a new FAC system developed

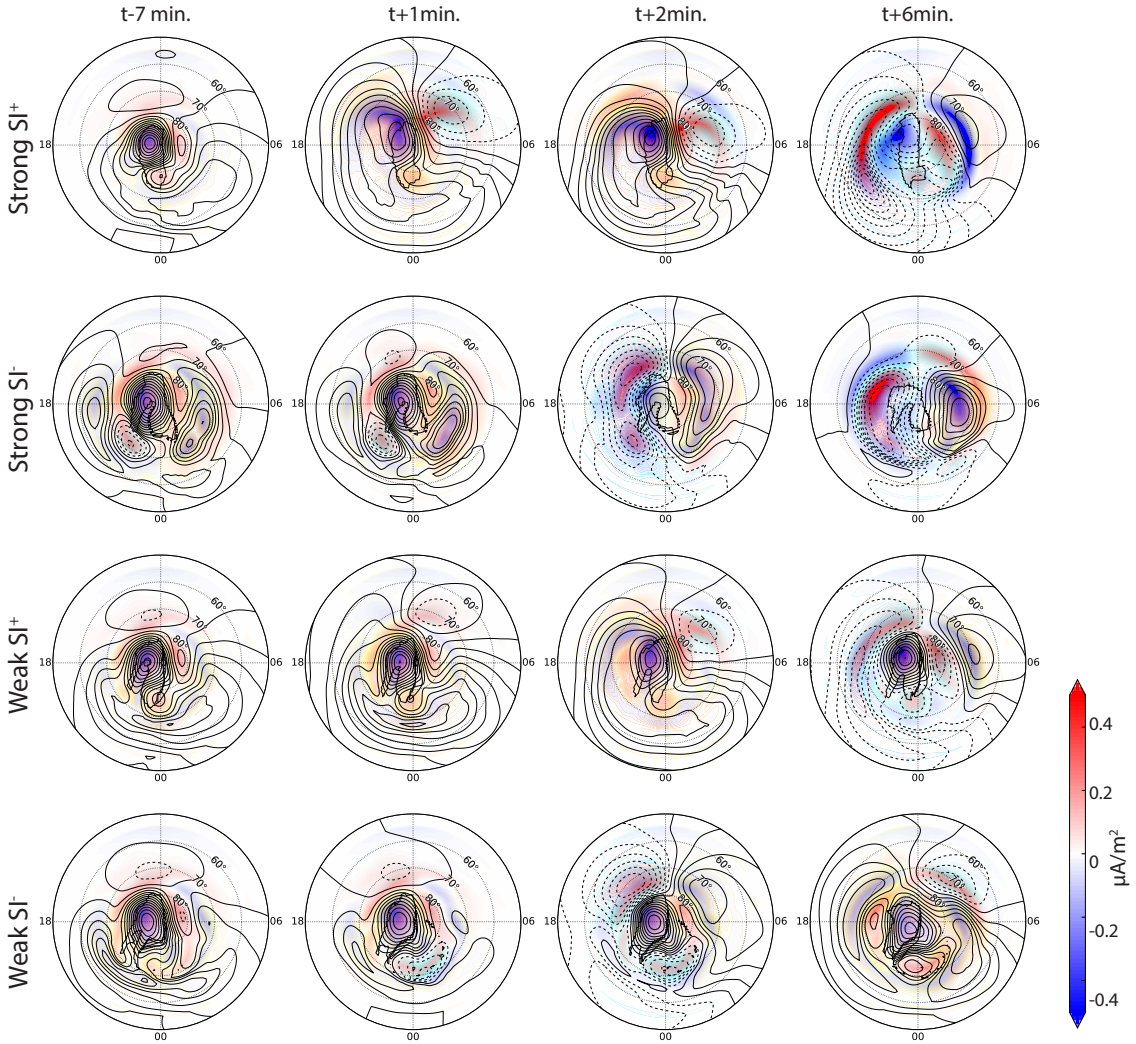

Figure 6.10: The evolution of the FACs are shown at quiet time (a), 1 (b), 2 (c) and 6 (d) minutes after the arrival of the perturbations. Panels show strong SI^+, SI^-, weak SI^+ and SI^- simulations from top to bottom. The red (blue) contours show upward (downward) FACs, the dashed and solid lines show electric field potentials.

with an opposite polarity to the initial FACs, as shown in Figure 6.6c. During the magnetospheric compression, these perturbation FACs had an upward FAC cell at dusk, and a downward FAC cell at dawn. The FAC cells were larger spatially and amplitude wise during the strong compression, compared with the weak compression. On the other hand, the perturbation FACs for decompression had an upward cell at dawn and a downward cell at dusk. Similarly, the stronger decompression cells were larger in size and amplitude compared with the weak decompression case.

Figure 6.10d shows the FAC profiles 6 minutes after the arrival of the perturbation. The MI^+ FACs were larger than the SI^+ case, but the profiles for both the strong and weak case were very similar to each other. The PI^- FACs were stronger than the MI^- FACs for the decompression cases. The upward PI^- and MI^- FACs for the weak case also merged at 12 MLT. In addition, the weak SI^- case had an upward FAC cell at midnight throughout the interval, which was also seen in the SI^+ FACs. This upward FAC cell further amplified as the magnetosphere expanded.

6.4.2 Joule Heating Response

Figure 6.11 shows the variation in the Joule heating profile as a response to strong SI^+, strong SI^-, weak SI^+ and weak SI^-. Seven minutes prior to the perturbation, the Joule heating had a peak in the noon sector for all four cases. The strong SI^- profile showed an additional enhancement along the dusk sector. Apart from the strong SI^+ case, the peak heating occurred at 78°, 14 MLT.

Figure 6.11b shows the response 1 minute after the perturbation. For the strong SI^+ case, the peak enhancement occurred between the 11-13 MLT sector, corresponding to the region in between the dawn and dusk PI^+ FACs in Figure 6.10. The weak SI^+ case had a peak at the same MLT but at a higher latitude. The response was also significantly smaller in magnitude and size compared to the strong SI^+. The initial response of the strong SI^- was not as prominent as the response of the strong SI^+.

Both strong and weak SI^- simulations showed mild enhancements in Joule heating rates on the nightside.

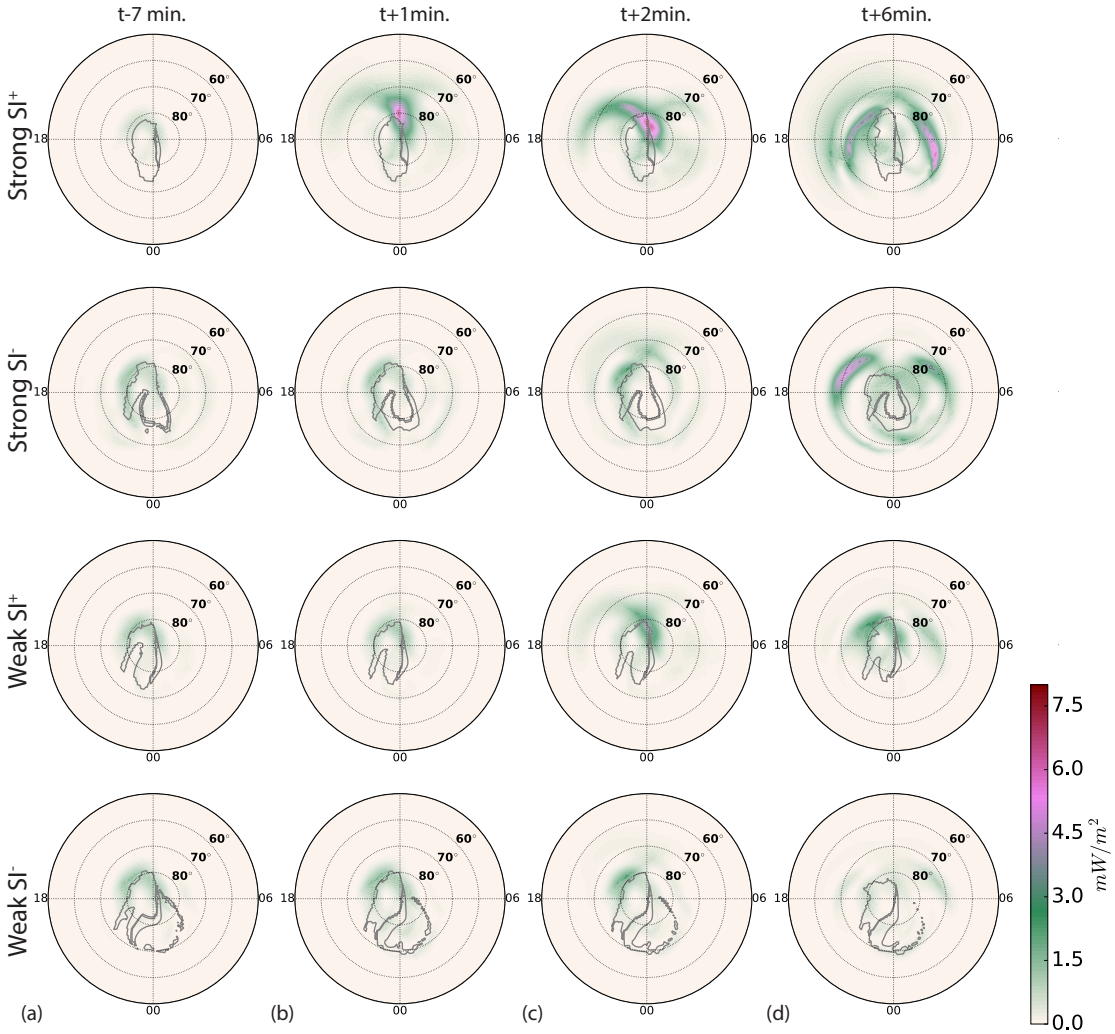

Figure 6.11: The evolution of the Joule heating profiles are shown at quiet time (a), 1 (b), 2 (c) and 6 (d) minutes after the arrival of the perturbations. Panels show strong SI^+, SI^-, weak SI^+ and SI^- simulations from top to bottom.

At the start of the main impulse phase, shown in Figure 6.11c, the heating for the strong SI^+ case was enhanced in between regions of PI^+ and MI^+ currents, extending from the dayside towards dawn and dusk. The heating in the weak SI^+ case was also further increased in the noon sector, with weak extension towards dawn

and dusk. For both SI^+ events, the heating in the dusk sector was larger than that in the dawn sector. The strong SI^- profile also showed an additional heating patch in the noon sector with the dusk patch further amplifying. The weak SI^- also showed an enhancement in the same locations. Surprisingly the amplitude of the dusk patch surpassed that of the strong SI^- by 2 mW/m^2.

Figure 6.11d shows 6 minutes after the arrival of the perturbation. The highest Joule heating rates were seen from 05-07 MLT, 14-18 MLT, 13-15 MLT, and 04-06 MLT for the strong SI^+, strong SI^-, weak SI^+, and weak SI^- respectively. There were two heating channels in all cases, which corresponded to the region between PI and MI FACs. The SI^- cases showed additional heating channels at higher latitudes, especially, in the midnight sector which corresponded to regions between PI^- FACs and pre-existing NBZ currents.

6.4.3 Ion Temperature Response

Figure 6.12 shows the ion convection patterns and the differenced ion temperature profiles obtained by removing the profile at one previous time step. The ion convection patterns were very similar to each other prior to the event.

At t+1, the ion temperature enhancement was above 150 K from 10 to 13 LT in the strong SI^+ case, corresponding to the peak Joule heating region for this time. The ion convection profile consisted of a clock-wise rotating vortex at dawn and a counter clock-wise rotating vortex in the dusk sector. At t+2, the latitudes below 70° on the dayside started cooling, whereas the region corresponding to the peak Joule heating rates were heated. The ion convection vortices were enlarged, with the dusk vortex being larger than the dawn vortex. At t+6, the ion convection vortices had opposite senses of rotation to the previous ones, and the highest ion temperature regions shifted to 5 LT and 20 LT.

The ion temperature response in the weak SI^+ case lagged 1 minute, compared

to the strong SI^+, due to the Joule heating being weaker. The ion temperature enhancement at t+2 was around 120 K, with vortices that had similar senses of rotation but mapping to slightly higher latitudes. At t+6, the ion convection vortices had reversed senses of rotation but were not as effective as the strong SI^+ in perturbing the nightside ionosphere.

In the strong SI^- case, a pair of flow vortices appeared at t+2 with a clock-wise rotating vortex at dusk and a counter clock-wise rotating vortex at dawn. The ion temperature enhancement was much weaker compared to the SI^+, and the convection vortices had opposite senses of rotation. At t+6, the rotation sense of the ion convection vortices had reversed and the peak heating occurred between 04-06 LT.

The ion convection response of the weak SI^- was very similar to the strong SI^- with peak ion temperature enhancement being 20 K. At t+6, the ion convection vortices had reversed senses of rotation, similar to the strong SI^- case. The peak temperature enhancement occurred between 06-09 LT.

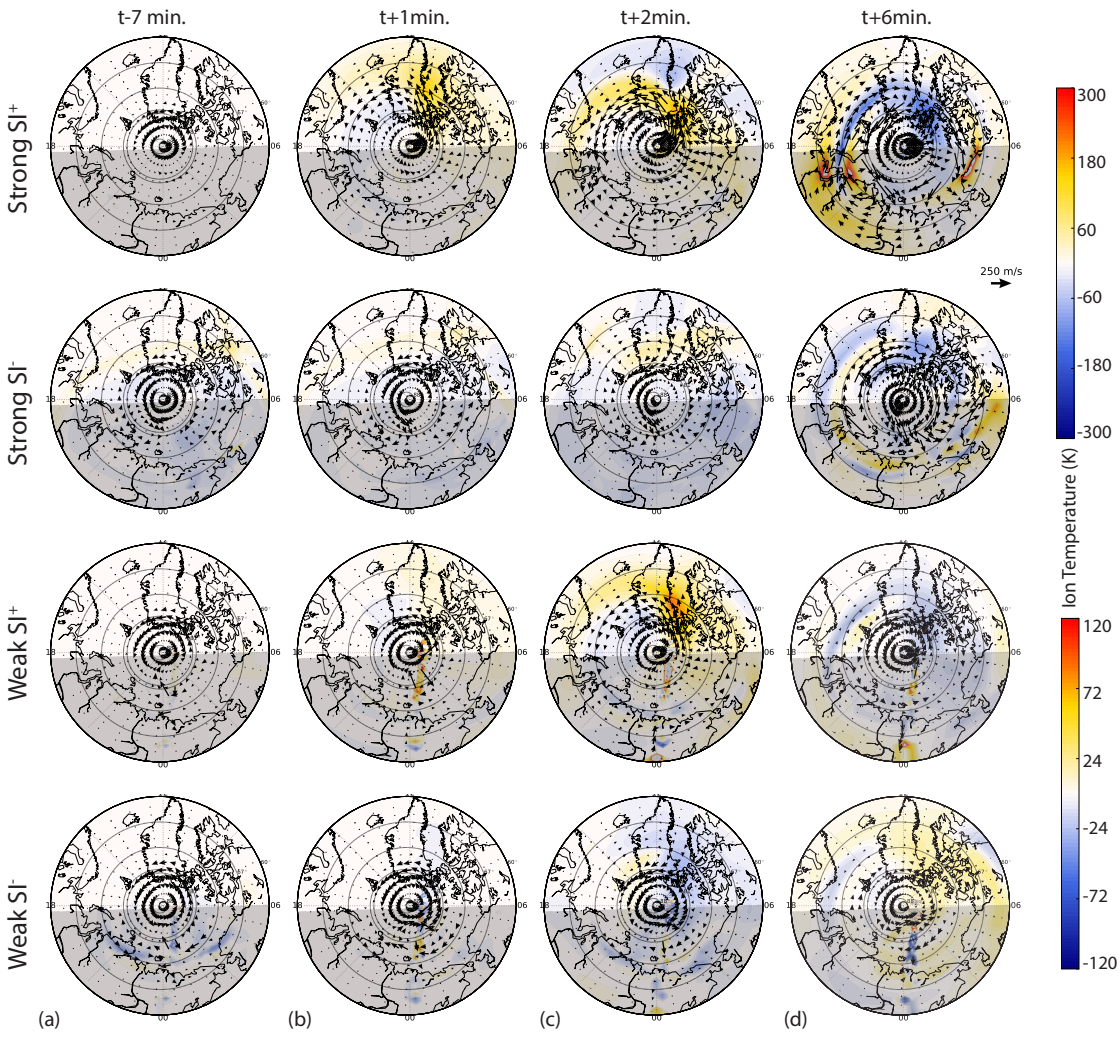

Figure 6.12: The evolution of the differenced ion temperature profiles are shown at quiet time (a), 1 (b), 2 (c) and 6 (d) minutes after the arrival of the perturbations with ion convection vectors on top for the Northern Hemisphere. Panels show strong SI^+, SI^-, weak SI^+ and SI^- simulations from top to bottom. The strong and weak simulation results are shown with separate color bars.

6.4.4 Virtual Magnetometer Response

The northward component of the baseline subtracted magnetic field perturbations at the ground level, derived from the virtual magnetometers are presented in Figure 6.13. The responses of the weak and strong SI^+s were qualitatively very similar but

quantitatively different. In both cases, the high-latitude ($> 70°$) response between 12-19 MLT was positive (green), while the 19-12 MLT was negative (pink) with the exception of 04-06 MLT positive response seen in weak SI^+. The mid and low-latitude ($< 70°$) response during the PI^+ was negative between 2-19 MLT and positive between 19-02 MLT. These PI^+ responses eventually weakened, as shown in Figure 6.13c, and reversed at the MI^+ phase shown in Figure 6.13d. The response at the high-latitudes was positive between 18-01 MLT, and negative between 01-18 MLT. Similarly, the mid and low-latitude ($< 70°$) responses were positive everywhere except within 18-00 MLT between $60° - 70°$.

The responses were also qualitatively very similar for both SI^- cases. The high-latitude PI^- signatures consisted of an enhancement in between 15-02 MLT and a decrease in between 2-15 MLT. At t+6 min, the high-latitude MI^- signatures consisted of an enhancement between 02-13 MLT, and a decrement between 13-02 MLT, with the exception of an enhancement between 13-20 MLT seen in the strong SI^- case. The low-latitude response was a decrement everywhere except the positive response at the mid-latitudes ($60° - 70°$) between 22-01 MLT in both cases.

The overall ground magnetic field polarity distributions as a response to SI^+ and SI^- were mirror images with slight exceptions at high-latitudes ($< 70°$) between 5-7 MLT during the preliminary impulse phase and between 16-18 MLTs during the main impulse phase.

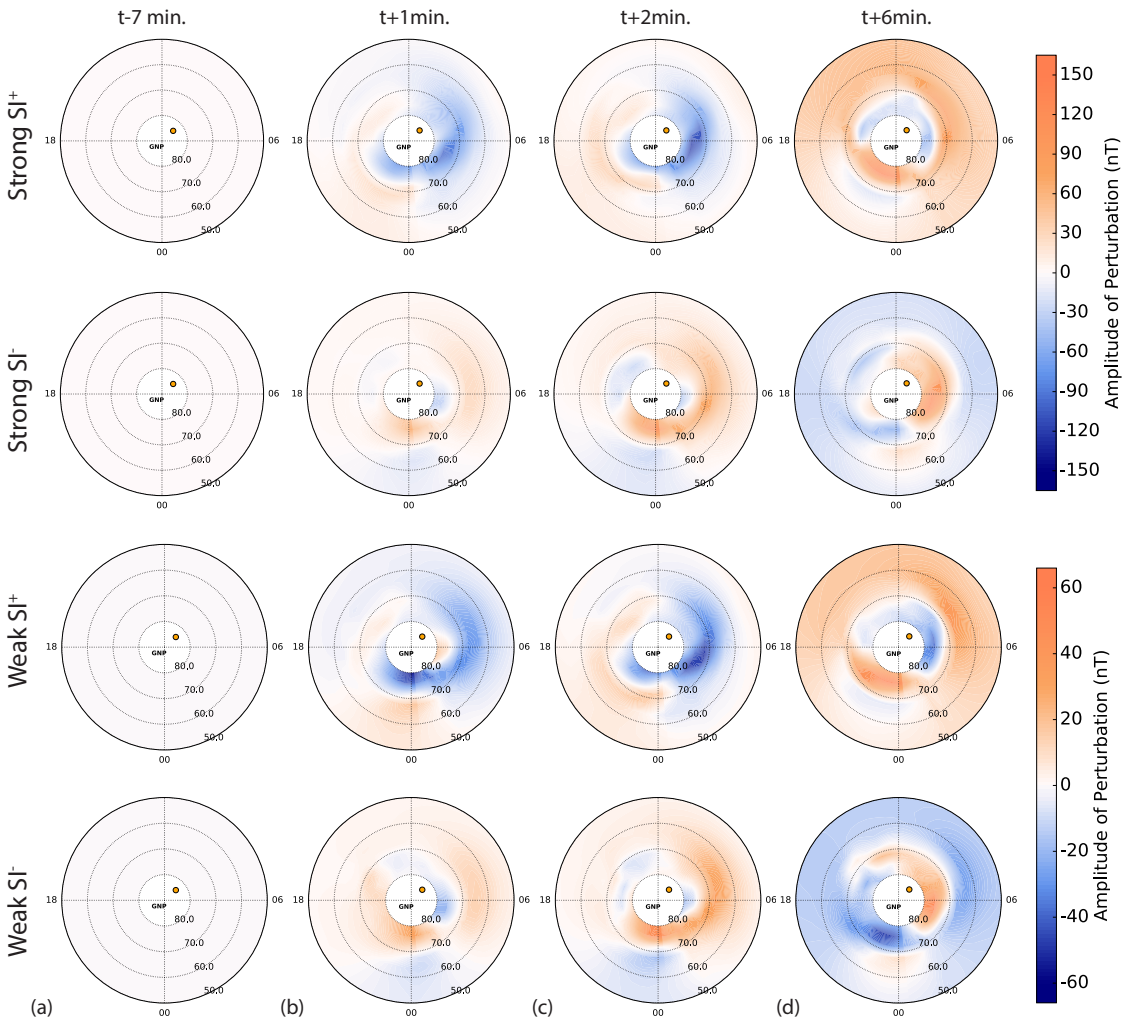

Figure 6.13: The evolution of the baseline subtracted magnetic perturbation profiles at the ground are shown at quiet time (a), 1 (b), 2 (c) and 6 (d) minutes after the arrival of the perturbations for the Northern Hemisphere. Panels show strong SI^+, SI^-, weak SI^+ and SI^- simulations from top to bottom. The strong and weak simulation results are shown with separate color bars.

6.4.5 Altitude Profiles in the Ionosphere

Figure 6.14 shows the ion temperature (left), electron temperature (middle) and density profiles (right) in the dawn (a) and dusk (b) sectors for select times during the strong SI^+. The dawn [11 LT, 78°] and dusk [14 LT, 77°] locations were picked

based on the points where significant changes occurred in the ion convection profiles. The ion temperature profile in Figure 6.11a shows that the highest ion temperature enhancements occurred below 300 km at 1440 UT, with a peak enhancement reaching 300 K. However, the ion temperature dropped back to its initial value by 1445 UT. The electron temperature above 180 km was also enhanced about 100 K at 1440 UT, dropping back to the initial values by 1450 UT. The electron density profile did not show a significant variation during this interval.

Figure 6.14b shows the aforementioned quantities in the dusk sector. The peak ion temperature enhancement occurred at 1440 UT, which was around 150 K at 180 km, however it cooled down to initial values by 1445 UT. The highest electron temperature enhancement occurred at the same time, which was around 100 K above 180 km. The electron density was first enhanced then dropped below the initial values, however this variation was not very significant above 150 km. Below 150 km, the electron density increased by 20% of its initial value at 1440 UT, then dropped by 22% at 1450 UT compared to the values at 1430 UT.

Figure 6.15 shows the same vertical profiles of ion temperature (left), electron temperature (middle) and density profiles (right) at dawn (a) and dusk (b) sectors for select times during the strong SI^- event. Again, the dawn [11 LT, 73°] and dusk [14 LT, 80°] locations were picked based on locations which showed highest variations in ion convection profiles. During the SI^- event, the peak ion temperature enhancement was around 300 K which occurred at 1440 UT at 240 km, followed by a cooling of around 150 K. At 1438 UT, the electron temperature was enhanced around 300 K above 160 km, stayed high until 1445 UT, and cooled back to the initial values at 1450 UT. The electron density above 180 km, showed 18% enhancement reaching a peak at 1450 UT, while the values dropped around 60% below the initial value under 130 km.

On the dusk side shown in Figure 6.15b, the ion temperature decreased above 150

km, with a peak drop around 150 K at 1440 UT, and further decreased about 150 K by 1450 UT. Similarly, electron temperature dropped above 150 km, with a peak drop around 300 K by 1450 UT. The electron density was enhanced above 180 km, however the enhancement was very small. Below 120 km, the electron density profile at 1445 UT was 55% smaller than at 1430 UT. This overall drop was around 25% below 120 km at 1450 UT.

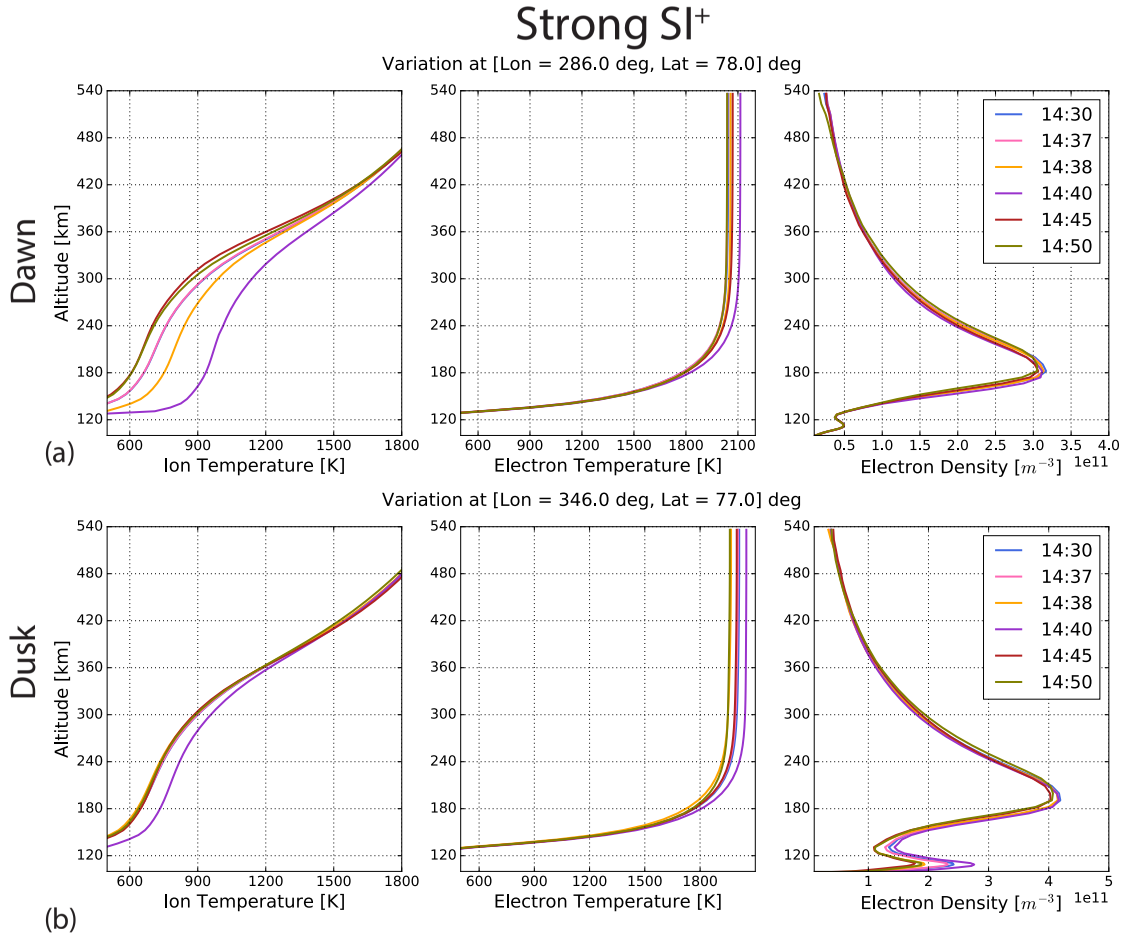

Figure 6.14: The vertical ion temperature (left), electron temperature (middle), and the electron density (right) profiles at select time steps are shown at peak heating locations on the dawn (a) and the dusk (b) sectors for the strong SI^{+} event. The time steps shown are 1430 UT (t-7min; blue), 1437 UT (t; pink), 1438 UT (t+1min; orange), 1440 UT (t+3min; purple), 1445 UT (t+8min; brown) and 1450 UT (t+13min; green).

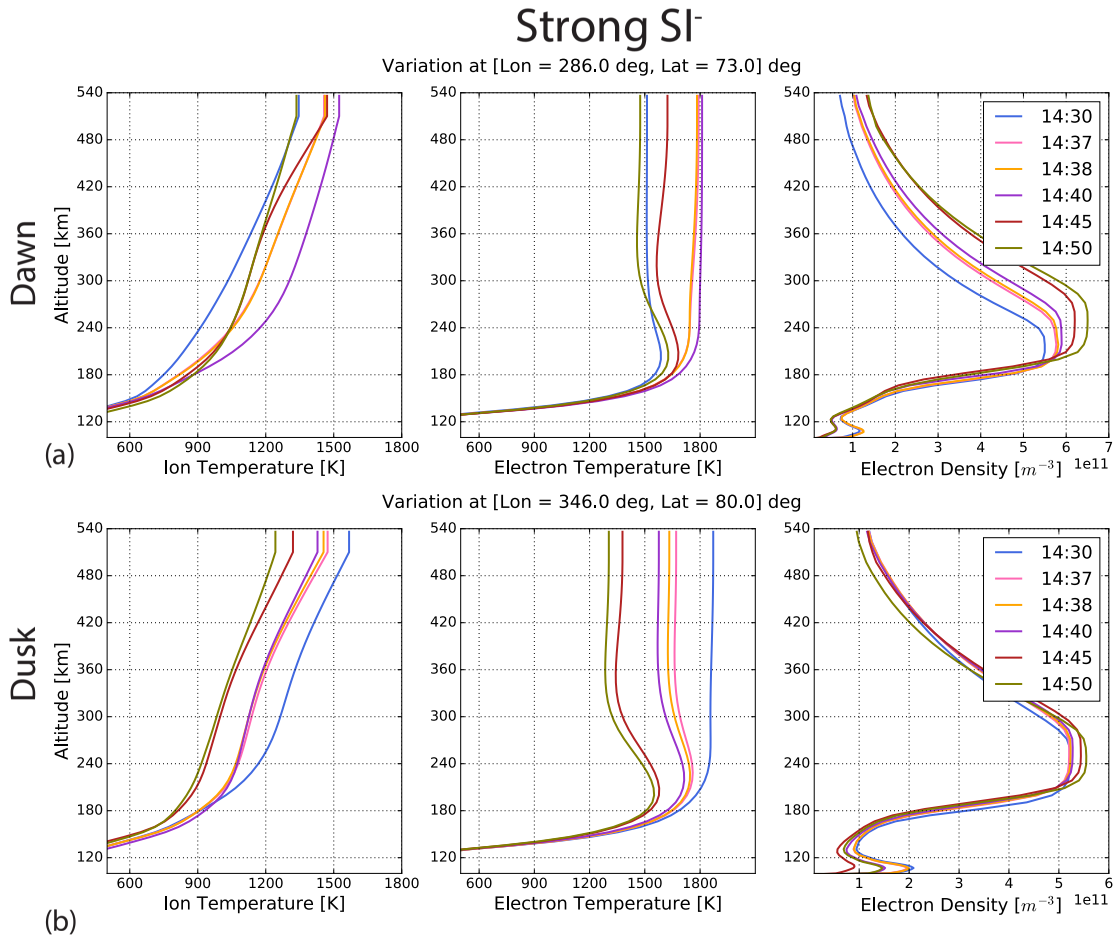

Figure 6.15: The vertical ion temperature (left), electron temperature (middle), and the electron density (right) profiles at select time steps are shown at peak heating locations on the dawn (a) and the dusk (b) sectors for the strong SI^{-} event. The time steps shown are 1430 UT (t-7min; blue), 1437 UT (t; pink), 1438 UT (t+1min; orange), 1440 UT (t+3min; purple), 1445 UT (t+8min; brown) and 1450 UT (t+13min; green).

6.5 Discussion

The simulated response of the global magnetosphere revealed distinct responses to PI phases. During compression, a pair of PI^+ vortices formed in the dayside dawn (counter clock-wise) and dusk sectors (clock-wise), later propagating towards the tail. The PI^+ signatures were attributed to magnetopause deformation [*Kivelson and Southwood* (1991)] but the simulation results showed that the existence of magnetospheric flows and their horizontal motion with the compression of the nose of the magnetosphere also play a role in the formation of these vortical flows. On the other hand, the simulations of the strong SI^- case showed a pair of PI^- vortices forming as a result of magnetospheric expansion starting from the nose. These sunward flows lead to a clock-wise rotating vortex on the dawn and a counter clock-wise rotating vortex in the dusk sector. These vortices generate a pair of upward FACs on the dusk and a downward FACs on the dawn sectors which can explain the two-step response reported in *Araki and Nagano* (1988) and *Takeuchi et al.* (2002).

Both the PI^+ and the PI^- vortices haven't been observed before, whereas both MI^+ [*Samsonov and Sibeck* (2013)] and MI^- [*Zhao et al.* (2015)] vortices have been reported. The further investigation of the V_x and V_Y along the possible spacecraft trajectories revealed that back to back measurements of the PI and MI vortices did not distinguish the two oppositely rotating vortices, however a W shaped signature in either component accompanied by a decrease in the other velocity component can indicate the presence of two consecutive vortices with opposite senses of rotation. Such signatures are abundant in satellite observations, one of them is shown in Figure 5.7a for a decompression case at dusk.

The global simulations showed that for the SI^+ and SI^- cases a two-step response in the FAC profiles was observed. The PI^+ FACs, had an upward cell on the dawn and an upward cell on the dusk as shown in previous studies [*Fujita et al.* (2003a), *Yu. and Ridley* (2011), *Ozturk et al.* (2017)]. The PI^- FACs, had an upward cell

on the dusk and a downward cell on the dawn, which are opposite to that of the compression case. Both PI^+ and PI^- FACs had similar amplitudes, however the longitudinal extent of the PI^+ FACs was larger. The comparison between strong and weak PI FACs showed, even though the perturbation FACs had similar qualitative properties, that the magnitude of the FACs depended on the strength of the compression/decompression events.

The MI^+ FACs had an upward FAC cell on the dusk and a downward FAC cell on the dawn, similar to what has been shown in previous studies [*Fujita et al.* (2003a), *Yu. and Ridley* (2011), *Ozturk et al.* (2017)]. On the contrary, the MI^- FACs had an upward cell on the dawn and a downward cell on the dusk sectors. Similarly, the magnitude of the perturbation FACs depended on the strength of the compression/decompression events.

One interesting finding is that PI^+ FACs merged with the inner cells of the NBZ current system which had the same polarity in the dawn and dusk sectors, whereas the PI^- FACs merged with the outer cells of the NBZ current system that had the same dawn-dusk polarity. This resulted in formation of different channels in Joule heating profiles. The peak Joule heating channels occurred between PI^+ FACs during the compression, whereas they occurred between the inner and perturbed outer cells (outer cells + PI^- FACs) of the NBZ currents during decompression. The Joule heating channels during the MI phase occurred between the PI and MI FACs for both compression and decompression cases. However because of the aforementioned behaviour more channels formed at the nightside during decompression, since tailward traveling PI^- FACs kept perturbing the inner cells of the NBZ current systems. In addition, during the weak decompression event the amplitude of the NBZ current system and the weak PI^- and MI^- FACs were comparable, resulting in a different FAC profile compared with that of the strong SI^-.

The simulation results also showed that a two step response exists in the iono-

spheric convection patterns. A clock-wise ion convection vortex formed on the morning sector, whereas a counter clock-wise convection vortex formed on the afternoon sector at the PI^+ phase. On the contrary, a counter clock-wise ion convection vortex formed on the morning sector, whereas a clock-wise ion convection vortex formed on the afternoon sector during the PI^- phase. The ion convection speeds for the PI^- were smaller than those for PI^+. New ion convection vortices with opposite senses of rotation formed during the MI phase for both compression and decompression. The comparison between strong and weak cases of compression showed similar qualitative results, however since the FAC intensity for the strong compression case was higher, the ions responded earlier to the strong compression. The comparison between strong and weak cases of decompression showed differences between regions where peak temperature enhancements occurred.

The simulated ground magnetic field maps showed that the SI^+ and SI^- events were almost mirror images of each other, with minor exceptions. However, as opposed to the SI^+ model by *Araki* (1994a), the response between dawn and dusk sectors was not asymmetric at the MI phase. The polarity reversal at this stage was between 3-18 MLT.

The investigation of the altitude profiles during the SI^+ and SI^- events also showed very distinct responses. The ion temperature profile was affected most from the SI^+, showing enhancements around 100-300 K between 120-300 km. The electron density below 120 km at dusk sector also responded to the SI^+, with a 10% enhancement at 1440 UT, which can be due to the downward precipitation of electrons from the upward PI^+ FAC, this value later dropped below the initial value. The altitudinal response to the SI^- showed more variations in all three quantities. Both the ion and electron temperatures in the dawn sector were enhanced (above 180 km), around 300 K at 1440 UT. The electron density was also enhanced by 18% above 180 km, but dropped by 60% below 120 km. However on the dusk side, both the ion and electron

temperatures dropped by 300 K above 180 km. At this location, the electron density was enhanced by 5% above 180 km, but dropped by 55% below 120 km.

6.6 Summary and Conclusions

Four idealized events, namely a strong SI^+, a strong SI^-, a weak SI^+ and weak SI^-, were investigated using the global MHD and I-T models to understand the magnetospheric and ionospheric responses to compression and decompression. The findings of this study can be summarized as follows:

1. A pair of dawn dusk vortices appear on the dayside with opposite polarities during the PI phase for both magnetospheric compression and expansion. The PI^+ and PI^- vortices have opposite senses of rotation at dawn and dusk sectors.

2. The PI^+ FACs merge with the inner cells of the NBZ current system, whereas the PI^- FACs merge with the outer cells of NBZ current system. This results in different heat channels forming in between current systems.

3. The comparison of the strong and weak SI^+ events showed that both responses are qualitatively very similar, whereas the magnitude of the perturbations depend on the strength of the compression.

4. The comparison of the strong and weak SI^- events showed that the mechanisms giving rise to perturbations were similar, however they couple with NBZ and R1 currents differently, resulting in spatial variations of the response.

5. The polarity distributions of SI^+ and SI^- were almost mirror images of each other with responses reversing in between 3-18 MLT.

6. The altitude profiles of ion temperature, electron temperature and density showed stronger responses to the SI^- event. The ion and electron tempera-

tures increased by around 300 K on the dawn but decreased by around 300 K on the dusk sector.

CHAPTER VII

Conclusions and Future Work

7.1 Findings of the Work

In this study, the geospace system (M-I-T) response to solar wind dynamic pressure variations was investigated with the extensive use of global models. The magnetospheric flows, FACs, ion convection flows, ground magnetic field, ion, electron and neutral temperature perturbations were examined in detail to understand (1) their magnetospheric and ionospheric sources, (2) the formation and evolution of the perturbations, (3) the spatial asymmetries due to the compression and decompression of the magnetosphere. The main conclusions of this work are summarized as follows:

Q1. What is the role of the IMF B_Y in determining the geospace system response to solar wind dynamic pressure enhancement events?

The IMF B_Y affects the symmetry of the NBZ current system. Even though the magnetospheric flows and associated FAC systems due to solar wind dynamic pressure increase did not show significant differences during different IMF B_Y orientations. The superposition of these transient FACs with the B_Y dependent NBZ currents created asymmetric responses. The total ground magnetic perturbation at high-latitudes was mostly due to the Hall current systems, with noon sector being the region where the peak perturbation was recorded during negative B_Y, and the dawn sector being

the region where the peak perturbation occurred during the positive B_Y. For the zero B_Y simulations, there were two peaks located in both regions.

Q2. What are the effects of magnetospheric compression on the I-T system?
The high-latitude convection patterns were largely perturbed during the compression. In certain regions, the flow speeds exceeded 1000 m/s, in particular between the PI and MI FACs. The ion temperature enhancements were above 1000 K at these locations, due to significant frictional heating. The PFISR observations for the ion temperature enhancement were even higher than the modeled results, indicating that the frictional heating rates were underestimated in the model. Within the flow channel, the peak heat transfer and frictional heating rates between ions and neutrals and the peak ionospheric density were co-located with the peak ionospheric density at 240 km. Both heating rates were similar in magnitude and delivered energy to the neutrals at a rate of 60K/min. Subsequently, in the heating region the O^+ and electron density dropped due to charge exchange rates increasing proportionately to the ion temperature while the NO^+ density increased in the same region.

Q3. What are the magnetospheric and ionospheric responses to a solar wind dynamic pressure decrement event?
A two-step response was seen in the magnetosphere and ionosphere system after the solar wind dynamic pressure decrease. First, a pair of vortices appeared on the dayside as a response to magnetospheric expansion. These PI^- vortices had a clockwise sense of rotation on the dusk, and a counter clockwise sense of rotation on the dawn. Following the PI^- vortices, a pair of MI^- vortices appeared. These MI^- vortices had a counter clockwise sense of rotation on the dusk and a clockwise sense of rotation on the dawn, exactly opposite to the PI^- vortices. These PI^- and MI^- vortices mapped to the ionosphere as PI^- (downward on the dawn and upward on the dusk)

and MI^- (upward on the dawn and downward on the dusk) FACs. The polarity distribution of the magnetic field perturbations at the ground level slightly deviated from the SI^- model of *Araki* (1994a), which is a mirror image of the SI^+, but this deviation is attributed to variations in the IMF drivers and the dipole tilt.

Q4. How are the I-T systems affected by the magnetospheric decompression?
The Joule heating in the noon sector decreased as a result of ionospheric electric field potential contours reconfigure after the magnetospheric expansion. The ion temperature dropped by around 1500 K in the noon sector, which was in between the PI^- and the MI^- FACs. However, 15 minutes later it increased by around 800 K due to the propagation of the MI^- FACs. On the contrary, the electron temperature, density and the neutral temperatures were not significantly affected by the magnetospheric expansion.

Q5. What are the differences in the geospace response between the solar wind dynamic pressure enhancement and decrement events?
The PI^+ and PI^- vortices have opposite senses of rotation at the dawn and the dusk sectors. The PI^+ FACs merge with the NBZ current system, whereas the PI^- FACs merge with the Region-1 current system. The superposition of the perturbation FACs with pre-existing FACs results in different locations of energy deposition and heating channels. The MI^+ and MI^- vortices had opposite senses of rotations compared to their predecessor PI^+ and PI^- vortices, resulting in MI^+ and MI^- FACs with opposite directions compared to the PI^+ and PI^- FACs. The polarity distributions of ground magnetic perturbations of SI^+ and SI^- were almost mirror images of each other with responses reversing in between 3-18 MLT.

7.2 Future Work

7.2.1 Exploring the Effects of Other Solar Wind and IMF Drivers During Solar Wind Dynamic Pressure Variations

Global modeling is a powerful tool that can help explore the effects of different drivers. In this study, only the northward IMF B_Z case has been investigated. This means that the open flux in the polar cap region was low, and no significant geomagnetic activity was expected during these periods. However, during intervals of southward IMF B_Z, the polar cap open flux content increases, and the magnetosphere can be more dynamic. An example of how the magnetopause standoff distance changes as a result of southward turning of the IMF can be seen in Figure 7.1. The figure shows the variation of the magnetopause standoff distance calculated from the simulations using the density gradient model (solid line) and from the solar wind observations using the Shue model (dashed line) with the IMF B_Z (upper panel) and solar wind dynamic pressure (bottom panel) during the 11 June 2017 event.

Apart from the direction of the drivers such as B_Y, B_Z and V_Y, the magnitude of the solar wind and IMF parameters are known to contribute to the asymmetries that are observed in the geospace system response. In this study, how the solar wind density could affect the geospace system response was discussed briefly in Chapter VI. This study can be further be expanded to investigate how the CIRs and CMEs can individually affect the geospace system, by driving the models with representative idealized drivers that would resemble the typical values of the fast-slow solar wind structure of the CIRs, and the typical shock-sheath-flux rope structure of the CMEs.

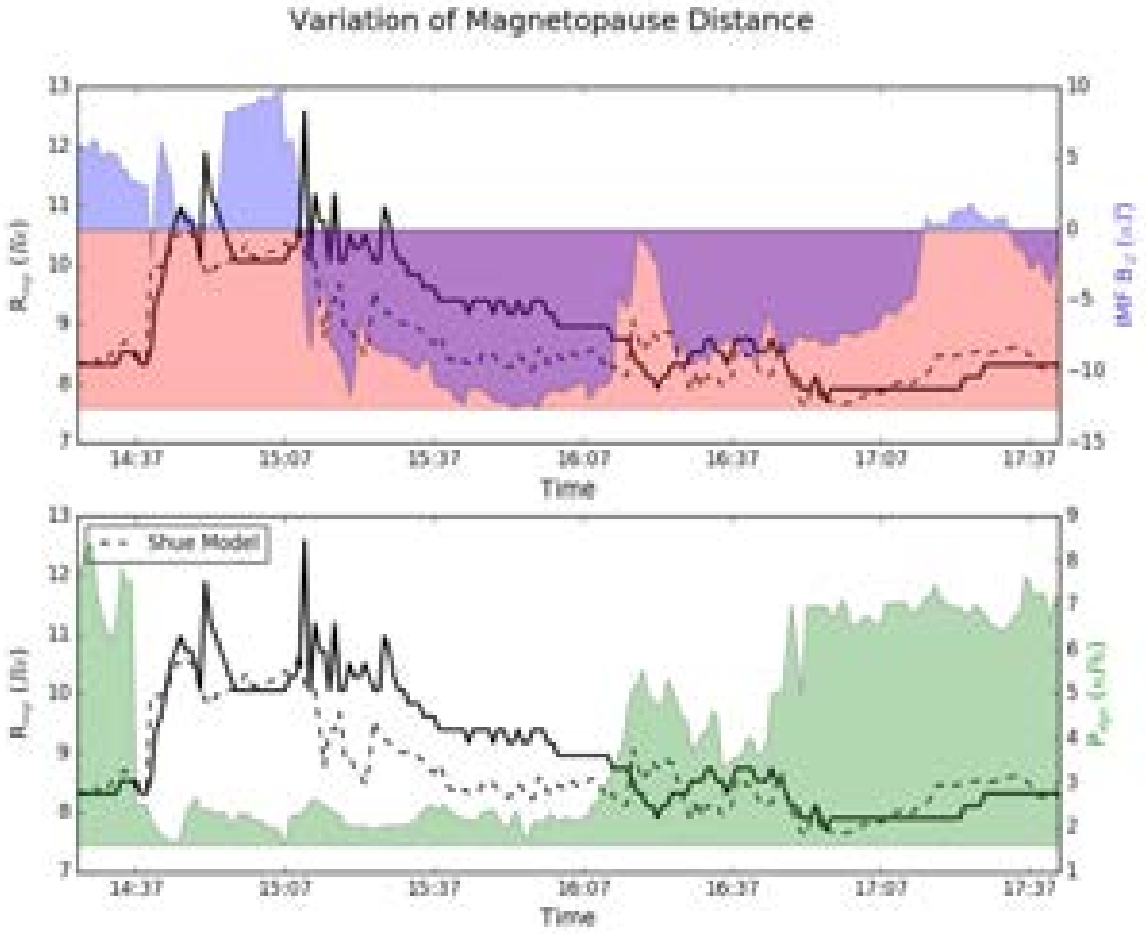

Figure 7.1: The variation of the magnetopause standoff distance calculated from the simulations using the density gradient model (solid line) and from the solar wind observations using the Shue model (dashed line) with the IMF B_Z (upper panel; blue) and solar wind dynamic pressure (bottom panel; green) between 1430-1740 UT during the 11 June 2017 event.

7.2.2 Exploring the Magnetotail Response to the Solar Wind Dynamic Pressure Variations

In this study, the focus was on the dayside responses to the solar wind dynamic pressure variations. However, as the compression/decompression front propagates towards the tail, it will perturb the magnetospheric flows, the magnetic field configuration and the currents in the tail. Investigating how the magnetotail responds to the compression/decompression events, as well as quantitatively determining how long the perturbations last will further our understanding of the tail dynamics.

7.2.3 Improving the Models

Conductance plays a key role in the coupling of the M-I-T systems. The case studies presented in this work showed that the simulated results mostly underestimated the ground magnetic field perturbations, the ion and electron temperatures compared with the observations. One possible reason is that the conductance model used in the system might be responsible for such disparities. Improved conductance models are essential to truly assess the response of the geospace system to the solar wind and IMF perturbations.

BIBLIOGRAPHY

Amm, O., M. J. Engebretson, R. A. Greenwald, H. Lühr, and T. Moretto (1999), Direct determination of imf by related cusp current systems using superdarn radar and multiple ground magnetometer data: A link to theory on cusp current origin, *Journal of Geophysical Research*.

Anderson, B. J., H. Korth, D. L. Waters, and P. Stauning (2008), Statistical birkeland current distributions from magnetic field observations by iridium constellation, *Annales Geophysicae*, *26*, 671–687.

Araki, T. (1994a), Global structure of geomagnetic sudden commencement, *Planetary Space Science*, *25*, 373–384.

Araki, T. (1994b), A physical model of geomagnetic sudden commencement, *AGU*, *81*.

Araki, T., and H. Nagano (1988), Geomagnetic response to sudden expansion of the magnetosphere, *Journal of Geophysical Research*.

Backus, G. (1986), Poloidal and toroidal fields in geomagnetic field modeling, *Review Geophysics*.

Balogh, A., L. J. Lanzerotti, and S. T. Suess (2008), *The Heliosphere through the Solar Activity Cycle*, Springer.

Belakhovsky, V. B., and V. G. Vorobjev (2016), Response of the night aurora to a negative sudden impulse, *Geomagnetism and Aeronomy*.

Belehaki, A., I. Stanislawska, and J. Lilensten (2009), An overview of ionosphere—thermosphere models available for space weather purposes, *Space Science Reviews*.

Bilitza, D. (2000), International reference ionosphere 2000, *Radio Science*.

Cherniak, I., I. Zakharenkova, and R. J. Redmon (2015), Dynamics of the highlatitude ionospheric irregularities during the 17 march 2015 st. patrick's day storm: Ground based gps measurements, *Space Weather*.

Clauer, C. R., P. M. Banks, A. Q. Smith, T. S. Jorgensen, E. Friis-Christensen, S. Vennerstrom, V. B. Wickwar, J. D. Kelly, and J. Doupnik (1984), Observation of interplanetary magnetic field and of ionospheric plasma convection in the vicinity of the dayside polar cleft, *Geophysical Research Letters*.

Codrescu, M. V., T. J. Fuller-Rowell, and J. C. Foster (1995), The importance of efield variability for joule heating in the highlatitude thermosphere, *Geophysical Research Letters*.

Collier, M. R., J. A. Slavin, R. P. Lepping, K. Ogilvie, A. Szabo, H. Laakso, and S. Taguchi (1998), Multispacecraft observations of sudden impulses in the magnetotail caused by solar wind pressure discontinuities: Wind and imp8, *Journal of Geophysical Research*.

Deng, Y., and A. J. Ridley (2006), Dependence of neutral winds on convection e-field, solar euv and auroral particle precipiation at high-latitudes, *Journal of Geophysical Research*.

Deng, Y., and A. J. Ridley (2007), Possible reasons for underestimating joule heating in global models: E field variability, spatial resolution, and vertical velocity, *Journal of Geophysical Research*.

Dungey, J. W. (1961), Interplanetary magnetic field and the auroral zone, *Physics Review Letters*.

Emmert, J. T. (2015), Thermospheric mass density: A review, *Advances in Space Research*, *56*, 773–824.

Engebretson, M. J., et al. (2013), Multiinstrument observations from svalbard of a traveling convection vortex, electromagnetic ion cyclotron wave burst, and proton precipitation associated with a bow shock instability, *Journal of Geophysical Research*.

Fagundes, P. R., F. A. Cardoso, B. G. Fejer, K. Venkatesh, B. A. G. Ribeiro, and V. G. Pillat (2016), Positive and negative gpstec ionospheric storm effects during the extreme space weather event of march 2015 over the brazilian sector, *Journal of Geophysical Research*.

Fok, M.-C., R. A. Wolf, R. W. Spiro, and T. E. Moore (2001), Comprehensive computational model of earth's ring current, *Journal of Geophysical Research*, *106*(A5), 8417–8424.

Foster, J. C., J. M. Holt, R. G. Musgrove, and D. S. Evans (1986), Ionospheric convection associated with discrete levels of particle precipitation, *Geophysical Research Letters*.

Friis-Christensen, E., M. A. McHenry, and C. R. Clauer (1988), Ionospheric traveling convection vortices observed near the polar cleft: A triggered response to sudden changes in the solar wind, *Geophysical Research Letters*.

Fujita, S., T. Tanaka, T. Kikuchi, K. Fujimoto, K. Hosokawa, and M. Itonaga (2003a), A numerical simulation of the geomagnetic sudden commencement: 1. generation of the field-aligned current associated with the preliminary impulse, *Journal of Geophysical Research*.

Fujita, S., T. Tanaka, T. Kikuchi, K. Fujimoto, and M. Itonaga (2003b), A numerical simulation of the geomagnetic sudden commencement: 1. plasma processes in the main impulse, *Journal of Geophysical Research*.

Fujita, S., T. Tanaka, T. Kikuchi, and S. Tsunomura (2004), A numerical simulation of a negative sudden impulse, *Earth Planets Space*.

Fujita, S., T. Tanaka, and T. Motoba (2005), A numerical simulation of the geomagnetic sudden commencement: 3. a sudden commencement in the magnetosphere-ionosphere compound system, *Journal of Geophysical Research*.

Fukushima, N. (1969), Equivalence in ground geomagnetic effect of chapman-vestine's and birkeland-alfven's current systems for polarmagnetic storms, *Report of Ionosphere Space Research*.

Garcia, K. S., and W. J. Hughes (2007), Finding the lyon-fedder-mobarry magnetopause: A statistical perspective, *Journal of Geophysical Research*.

Gjerloev, J. W. (2012), The supermag data proccessing technique, *Journal of Geophysical Research*.

Glassmeier, K. H., and C. Heppner (1992), Traveling magnetospheric convection twin vortices: Another case study, global characteristics and a model, *Journal of Geophysical Research*.

Glassmeier, K. H., M. Honisch, and J. Untiedt (1989), Groundbased and satellite observations of traveling magnetospheric convection twin vortices, *Journal of Geophysical Research*.

Gombosi, T. I. (2004), *Physics of the Space Environment*, Cambridge University Press.

Gosling, J. T. (1997), *Encyclopedia of the Solar System*, Academic Press.

Heelis, R. A. (1984), The effects of interplanetary magnetic field orientation on dayside high latitude convection, *Journal of Geophysical Research*.

Heelis, R. A., J. K. Lowell, and R. W. Spiro (1982), A model of the highlatitude ionospheric convection pattern, *Journal of Geophysical Research*.

Heppner, J. P., and N. C. Maynard (1987), Empirical high latitude electric field models, *Journal of Geophysical Research*.

Honisch, M., and K. H. Glassmeier (1986), Isolated transient magnetic variations in the auroral zone, *Eos Transactions*.

Huang, C. Y., Y. Huand, Y. J. Su, E. K. Sutton, M. R. Hairston, and W. R. Coley (2016), Ionospherethermosphere response to solar wind forcing during magnetic storms, *Journal of Space Weather Space Climate*.

Huttunen, K. E. J., J. A. Slavin, M. Collier, H. E. J. Koskinen, A. Szabo, E. Tanskanen, A. Balogh, E. Lucek, and H. Reme (2005), Cluster observations of sudden impulses in the magnetotail caused by interplanetary shocks and pressure increases, *Annales Geophysicae*.

Iijima, T., and T. A. Potemra (1976), Field-aligned currents in the dayside cusp observed by triad, *Journal of Geophysical Research*.

Jacobsen, K. S., and Y. L. Andalsvik (2016), Overview of the 2015 st. patrick's storm and its consequences for rtk and ppp positioning in norway, *Journal of Space Weather Space Climatep*.

Johnson, E. S., and R. A. Heelis (2005), Characteristics of ion velocity structure at high latitudes during steady southward interplanetary magnetic field conditions, *Journal of Geophysical Research*.

Kamide, Y., and A. C.-L. Chian (Eds.) (2007), *Handbook of the Solar-Terrestrial Environment*, Springer.

Kamide, Y., S. I. Akasofu, and A. Brekke (1976), Ionospheric currents obtaind from chatanika radar and ground magnetic perturbations at the auroral latitudes, *Planetary and Space Science*.

Kataoka, R., H. Fukunishi, and L. J. Lanzerotti (2003), Statistical identification of solar wind origins of magnetic storm on 17 march 2015, *Geophysical Research Letters*.

Kataoka, R., H. Fukunishi, S. Fujita, T. Tanaka, and M. Itonaga (2004), Transient response of the earth's magnetosphere to a localized density pulse in the solar wind: Simulation of traveling convection vortices, *Journal of Geophysical Research*.

Kataoka, R., D. Shiota, E. Kilpua, and K. Keika (2015), Pileup accident hypothesis of magnetic storm on 17 march 2015, *Geophysical Research Letters*.

Keiling, A., et al. (2009), Substorm current wedge drived by plasma flow vortices: Themis observations, *Journal of Geophysical Research*.

Kelley, M. C. (2009), *The Earth's Ionosphere Plasma Physics and Electrodynamics*, Academic Press.

Kikuchi, T., and T. Araki (1979), Transient response of uniform ionosphere and preliminary reverse impulse geomagnetic storm sudden commencement, *J. Atmos. Sol-Terr. Phys.*

Kim, H., C. R. Clauer, M. J. Engebretson, J. Matzka, D. G. Sibeck, H. J. Singer, C. Stolle, D. R. Weimer, and Z. Xu (2015), Conjugate observations of traveling convection vortices associated with transient events at the magnetopause conjugate observations of traveling convection vortices associated with transient events at the magnetopause conjugate observations of traveling convection vortices associated with transient events at the magnetopause, *Journal of Geophysical Research*.

Kivelson, M. G., and C. R. Russell (Eds.) (1997), *Introduction to Space Physics*, Cambridge University Press.

Kivelson, M. G., and D. J. Southwood (1991), Ionospheric traveling convection vortex generation by solar wind buffeting of the magnetosphere, *Journal of Geophysical Research*.

Knipp, D. J., W. K. Tobiska, and B. A. Emery (2004), Direct and indirect thermospheric heating sources for solar cycles 21–23, *Solar Physics*.

Kubota, Y., R. Kataoka, M. Den, T. Tanaka, T. Nagatsuma, and S. Fujita (2015), Global mhd simulation of magnetospheric response of preliminary impulse to large and sudden enhancement of the solar wind dynamic pressure, *Earth Planets Space*.

Lanzerotti, L. J. (2007), Space weather effects on communications, in *Space Weather Physics and Effects*, Springer Praxis Books.

Lanzerotti, L. J., R. M. Konik, A. Wolfe, D. Venkatesan, and C. G. Maclennan (1991), Cusp latitude magnetic impulse events: 1. occurrence statistics, *Journal of Geophysical Research*.

Liou, K. (2007), Large abrupt pressure decreases as a substorm onset trigger, *Geophysical Research Letters*.

Liu, J., W. Wang, A. Burns, X. Yue, S. Zhang, Y. Zhang, and C. Huang (2016), Profiles of ionospheric stormenhanced density during the 17 march 2015 great storm, *Journal of Geophysical Research*.

Matsushita, S., and W. Y. Xu (1982), Equivalent ionospheric current systems representing solar daily variations of the polar geomagnetic field, *Journal of Geophysical Research*.

Morley, S. K., J. Koller, D. T. W. B. A. Larsen, M. G. Henderson, and J. T. Niehof (2011), Spacepy - a python based library of tools for the space sciences, in *Proceedings of the Pth Python in science conference (SciPy 2010)*.

Motoba, T., T. Kikuchi, T. Okuzawa, and K. Yumoto (2003), Dynamical response of the magnetosphere-ionosphere system to a solar wind dynamic pressure oscillation, *Journal of Geophysical Research*.

Murr, D. L., W. J. Hughes, A. S. Rodger, E. Zesta, H. U. Frey, and A. T. Weatherwax (2002), Conjugate observations of traveling convection vortices: The field-aligned current system, *Journal of Geophysical Research*.

Newell, P. T., et al. (2002), Ovation: Oval variation, assesment, tracking, intensity and online nowcasting, *Annales Geophysicae*.

N.Sato, et al. (2001), Enhancement of optical aurora triggered by the solar wind negative pressure impulse, *Geophysical Research Letters*.

Oliveira, D. M., E. Zesta, P. W. Schuck, and E. K. Sutton (2017), Thermosphere global time response to geomagnetic storms caused by coronal mass ejections, *Journal of Geophysical Research*.

Ozturk, D. S., S. Zou, and J. A. Slavin (2017), Imf by effects on ground magnetometer response to increased solar wind dynamic pressure derived from global mhd simulations, *Journal of Geophysical Research*.

Picholtz, R. L. (1996), Communications by means of low earth orbiting satellites, *Modern Radio Science*.

Powell, K. G. (1994), An approximate riemann solver for magnetohydrodynamics (tha t works in more than one dimension), *Tech. rep.*, NASA.

Ridley, A. J., T. I. Gombosi, and D. L. DeZeeuw (2004), Ionospheric control of the magnetosphere: conductance, *Annales Geophysicae*, *22*, 567–584.

Ridley, A. J., Y. Deng, and G. Toth (2006), The global ionosphere-thermosphere model, *J. Atmos. Sol-Terr. Phys.*, *68*.

Samsonov, A., and D. G. Sibeck (2013), Large-scale flow vortices following a magnetospheric sudden impulse, *Journal of Geophysical Research*.

Schrijver, C. J., and G. L. Siscoe (Eds.) (2009), *Heliophysics Plasma Physics of the Local Cosmos*, Cambridge University Press.

Schunk, R., and A. Nagy (2009), *Ionospheres Physics, Plasma Physics and Chemistry*, Cambridge University Press.

Schunk, R. W., L. Zhu, and J. J. Sojka (1994), Ionospheric response to traveling convection twin vortices, *Geophysical Research Letters*.

Shang, J. J. S. (2018), Modeling plasma via electron impact ionization, *Aerospace*.

Shen, X. C., et al. (2016), Dayside magnetospheric ulf wave frequency modulated by a solar wind dynamic pressure negative impulse, *Journal of Geophysical Research*.

Shi, Y., et al. (2017), Highlatitude thermosphere neutral density response to solar wind dynamic pressure enhancement, *Journal of Geophysical Research*.

Shinbori, A., Y. Tsuji, T. Kikuchi, T. Araki, and S. Watari (2009), Magnetic latitude and local time dependence of the amplitude of geomagnetic sudden commencements, *Journal of Geophysical Research*.

Shue, J.-H., J. K. Chao, H. C. Fu, K. K. Khurana, C. T. Russell, H. J. Singer, and P. Song (1997), A new functional form to study the solar wind control of the magnetopause size and shape, *Journal of Geophysical Research*, *102*(9497).

Sitar, R. J., and C. R. C. E. Friis-Christensen (1996), High-latitude ground-based response to sudden changes in solar wind dynamic pressure, *Journal of Geophysical Research*.

Slinker, S. P., J. A. Fedder, W. J. Hughes, and J. G. Lyon (1996), Response of the ionosphere to a density pulse in the solar wind: Simulation of traveling convection vortices, *Geophysical Research Letters*.

Sojka, J. J., R. W. Schunk, M. D. Bowline, J. Chen, S. P. Slinker, and J. A. Fedder (1997), Driving a physical ionospheric model with a magnetospheric mhd model, *Journal of Geophysical Research*.

Suguira, M., T. L. Skillman, B. G. Ledley, and J. P. Heppner (1968), Propagation of the sudden commencement of july 8, 1966 to magnetotail, *Journal of Geophysical Research*.

Sun, T. R., C. Wang, J. J. Zhang, V. A. Pilipenko, Y. Wang, and J. Y. Wang (2014), The chain response of the magnetospheric and ground mangetic field to interplanetary shocks, *Journal of Geophysical Research*.

Takeuchi, T., T. Araki, A. Viljanen, and J. Watermann (2002), Geomagnetic negative sudden impulses: Interplanetary causes and polarization distribution, *Journal of Geophysical Research*.

Takeuchi, T., et al. (2000), Geomagnetic sudden impulse due to a magnetic cloud observed on may 13, 1995, *Journal of Geophysical Research*.

Tanaka, T. (2001), Interplanetary magnetic field by and auroral conductance effects on high latitude ionospheric convection patterns, *Journal of Geophysical Research*.

Tanaka, T. (2003), Formation of magnetospheric plasma population regimes coupled with the dynamo process in the convection system, *Journal of Geophysical Research*.

Tanaka, T. (2007), Magnetosphere-ionosphere convection as a compound system, *Space Science Reviews*.

Thayer, J. P. (1998), Heightresolved joule heating rates in the highlatitude e region and the influence of neutral winds, *Journal of Geophysical Research*.

Tian, A. M., X. C. Shen, Q. Q. Shi, B. B. Tang, M. Nowada, Q. G. Zong, and S. Y. Fu (2016), Dayside magnetospheric and ionospheric responses to solar wind pressure increase: Multispacecraft and ground observations, *Journal of Geophysical Research*.

Toffoletto, F., S. Sazykin, R. Spiro, and R. Wolf (2003), Inner magnetospheric modeling with the rice convection model, *Space Science Reviews*, *107*, 175–196.

Toth, G. (2000), The b = 0 constraint in shock-capturing magnetohydrodynamics codes., *Journal of Computational Physics*.

Toth, G., et al. (2005), Space weather modeling framework: A new tool for the space science community, *Journal of Geophysical Research*.

Untiedt, J., and W. Baumjohann (1993), Studies of polar current systems using the ims scandinavian magnetometer array, *Space Science Reviews*.

Valladares, C. E., D. Alcayde, J. V. Rodriguez, J. M. Ruohoniemi, and A. P. V. Eyken (1999), Observations of plasma density structures in association with the passage of traveling convection vortices and the occurrence of large plasma jets, *Annales Geophysicae*.

Verkhoglyadova, O., B. T. Tsuratani, A. J. Manucci, M. G. Mlynczak, L. A. Hunt, L. J. Paxton, and A. Komjathy (2016), Solar wind driving of ionospherethermosphere responses in three storms near st. patrick's day in 2012, 2013, and 2015, *Journal of Geophysical Research*.

Verkhoglyadova, O., X. Meng, A. J. Manucci, M. G. Mlynczak, L. A. Hunt, and G. Lu (2017), Ionosphere-thermosphere energy budgets for the icme storms of march 2013 and 2015 estimated with gitm and observational proxies, *Space Weather*.

Wang, Y., Q. Zhang, J. Liu, C. Shen, F. Shen, and Z. Yang (2016), On the propagation of a geoeffective coronal mass ejection during 15–17 march 2015, *Journal of Geophysical Research*.

Weimer, D. R. (1996), Flexible, imf dependent model of highlatitude electric potentials having 'space weather' applications, *Geophysical Research Letters*.

Weimer, D. R. (2005), Predicting surface geomagnetic variations using ionospheric electrodynamic models, *Journal of Geophysical Research*.

Weygand, J. M., O. Amm, A. Viljanen, V. Angelopoulos, D. Murr, M. J. Engebretson, H. Gleisner, and I. Mann (2011), Application and validation of the spherical elementary currents systems technique for deriving ionospheric equivalent currents with the north american and greenland ground magnetometer arrays, *Journal of Geophysical Research*.

Weygand, J. M., O. Amm, V. Angelopoulos, S. E. Milan, A. Grocott, H. Gleisner, and C. Stolle (2012), Comparison between superdarn flow vectors and equivalent ionospheric currents from ground magnetometer arrays, *Journal of Geophysical Research*.

Wilder, F. D., S. Eriksson, H. Korth, J. B. H. Baker, M. R. Hairston, C. Heinselman, and B. J. Anderson (2013), Field-aligned current reconfiguration and magnetospheric response to an impulse in the interplanetary magnetic field by component, *Geophysical Research Letters*.

Wilson, G. R., D. R. Weimer, J. O. Wise, and F. A. Marcos (2006), Response of the thermosphere to joule heating and particle precipitation, *Journal of Geophysical Research*.

Yu, Y., and A. J. Ridley (2008), Validation of the space weather modeling framework using ground based magnetometers, *Space Weather*.

Yu, Y., and A. J. Ridley (2009), The response of the magnetosphere-ionosphere system to a sudden dynamic pressure enhancement under southward imf conditions, *Annales Geophysicae*.

Yu., Y., and A. J. Ridley (2011), Understanding the response of the ionosphere-magnetosphere system to sudden solar wind density increases, *Journal of Geophysical Research*.

Zesta, E., W. J. Hughes, M. J. Engebretson, T. J. Hughes, A. J. Lazarus, and K. I. Paularena (1999), The november 9, 1993 traveling convection vortex event: A case study, *Journal of Geophysical Research*.

Zesta, E., W. J. Hughes, and M. J. Engebretson (2002), A statistical study of traveling convection vortices using the magnetometer array for cusp and cleft studies, *Journal of Geophysical Research*.

Zhang, B., W. Lotko, O. Brambles, M. Wiltberger, and J. G. Lyon (2014), Electron precipitation models in global magnetosphere simulations, *Journal of Geophysical Research*.

Zhang, X. Y., et al. (2010), Ulf waves excited by negative/positive solar wind dynamic pressure impulses at geosynchronous orbit, *Journal of Geophysical Research*.

Zhao, H. Y., et al. (2015), Magnetospheric vortices and their global effect after a solar wind dynamic pressure decrease, *Journal of Geophysical Research*.

Zhu, J. (2016), The effect of energy input on the earth's upper atmosphere, Ph.D. thesis, University of Michigan.

Zhu, J., A. J. Ridley, and Y. Deng (2016), Simulating electron and ion temperature in a global ionosphere thermosphere model: Validation and modeling an idealized substorm, *Journal of Atmospheric and Solar-Terrestrial Physics*.

Zhu, L., R. W. Schunk, and J. J. Sojka (1999), Effects of the magnetospheric precipitation and ionospheric conductivity on the ground magnetic signatures of traveling convection vortices, *Journal of Geophysical Research*.

Zou, S., D. S. Ozturk, R. Varney, and A. Reimer (2017), Effects of sudden commencement on the ionosphere: Pfisr observations and global mhd simulation, *Geophysical Research Letters*.